1947-2017

UNIVERSITY OF CRAIOVA

70 YEARS

Annals of the University of Craiova
The Chemistry Series

Analele Universităţii din Craiova
Seria Chimie

Volume XLIV, no. 1

2017

1947-2017
UNIVERSITY OF CRAIOVA
70 YEARS
TRADITION, PERFORMANCE, VISION

DEPARTMENT OF CHEMISTRY

RECTOR
CEZAR IONUŢ SPÎNU, PROF. PHD

Contact
Phone: +40 251 597048
Fax: +40 251 597048
Web page: http://chimie.ucv.ro/departament/
e-mail: office@chimie.ucv.ro

tehnoredactare – lect. univ. dr. Bogdan Tutunaru

Content

Annals of the University of Craiova
The Chemistry Series
Volume XLIV, No. 1 (2017) 2-12
homepage: chimie.ucv.ro/anale/

The electrochemical behaviour of 304L stainless steel in differents environments

Research article

*Roxana Grecu, Adriana Samide**

University of Craiova, Faculty of Sciences, Department of Chemistry, Calea Bucuresti, 107i, Craiova, Romania
*e-mail: samide_adriana@yahoo.com

Received: 18.01.2017 / *Accepted*: 27.02.2017 / *Published*: 10.05.2017

Abstract
The electrochemical behaviour of 304L stainless steel in different media was investigated using potentiodynamic polarization associated with the optical microscopy. The semilogarithmic curves were used to calculate the corrosion current density (i_{corr}), in order to determine the corrosion rezistance of 304L stainless steel in solutions containing Cl^- and CH_3COO^- ions and a mixture of aminoacids (commercial name: Aminosteril). The corrosion rate of 304L stainless steel studied in four media varies as follows: HCl > NaCl > CH_3COOH ≥ Aminosteril. These results show that the steel has a very good resistance to corrosion in studied solutions such as: natrium chloride, acetic acid and Aminosteril.

Keywords: 304L stainless steeel; corrosion rezitance; inhibition study; metronidazole drug

1. INTRODUCTION

The corrosion is one of the great issues affecting the integrity and the duration of the life of the bioimplants made of metals and their alloys. In contact with different environments, the metals are damaged by the processes of oxidation, which may affect in full surface. To enlarge the resistance of corrosion of these materials has developed different methods of protection for

metal surfaces. Through the application of these methods is to improve the properties of the metals and the decrease in the concentration of the products of corrosion.

The stability of the chemical, behavior of mechanically and biocompatibility with fluids and biological tissues are the conditions required for the use of the materials as implants in fractures and replacing the bones. Bioimplants are materials used for manufacture devices that can interact and coexist with biological systems. Biomaterials are used in the repair, replacement or increasing the damaged parts of the system the musculoskeletal as well as skeletal bones, joints and teeth. The following applications of these materials are: orthopedics prothesis, dental implants, the plates of the head [1].

One of the metals used for manufacturing bioimplants is stainless steel 304L. It contains chromium enough to form a passive layer of chromium oxide, which prevents further corrosion of the surface of the metal and stops the spread of corrosion in the internal structure and in addition because of the similar size of molecules of steel and the concentration of chromium are formed a close link between them, so that the layer of nitrous oxide remains attached to the surface of the metal. Certain organic molecules containing heteroatoms of sulfur, oxygen and nitrogen were suggested as inhibitors for corrosion for stainless steel [2]. The mechanism of inhibition to this class of inhibitors is based on the adsorption of ions and molecules on the metal [3]. It was also followed the use of non-toxic and harmless inhibitors of corrosion for environment. The role of the inhibitors of corrosion is to form layers on the metallic surface to restrict the processes of corrosion.

The inhibitor is defined as a substance which is added to a small amount, in an aggressive environment, may slow down or prevent corrosion of a material which is intended to come into contact with the environment in question. They can be used for permanent or temporary protection. In order to be effective, the inhibitor of corrosion must be compatible with the corrosive environment and with the structure of the metal and this implies the selection of it in accordance with the scientific rigorous criteria (mechanism of action, stability in the working conditions of the data) [4].

The organic compounds have at least one donor group of electrons that behave usually as a active center for adsorption as well as the nitrogen, oxygen, phosphorus or sulfur [5]. Their use is preferred to inorganic inhibitors, mainly for reasons of ecotoxicity.

The effect of drugs as ampicillin and benzylpenicillin in corrosion of stainless steel 304 in 1.0 M hydrochloric acid was investigated using the techniques, like: weight loss, potentiodynamic polarization and scanning electron microscopy (SEM). The effectiveness of the inhibition was increased by improving the concentration of corrosion inhibitor and decreased with the increased temperature. It has been demonstrated that the adsorption of these inhibitors shall be subject to the adsorption izotherms Langmuir. The

measurements of the degree of potentiodinamic polarization have indicated that the inhibitors are mixed. It was proposed the synergism between the potassium iodide and inhibitors. The results obtained with the three different methods are in accordance one with each other. Was studied the effect of molecular structure on the effectiveness of inhibition of these compounds. The choice of these inhibitors (ampicillin and benzylpenicillin) as corrosion inhibitors shall be based on: easy obtaining; contain oxygen, nitrogen and atoms of sulfur dioxide as active centers; high solubility in the acid, produce toxic effects; relatively cheap [2]. The molecules of adenina have small size and a flat ideal structure which makes the electronic effects will be much more important and sterical effects to be omitted. It also has the properties of low basic [6].

Adenine is relatively an easy and cheap product with a purity of less than 99 %. Being non-toxic and biodegradable the investigation of its properties of inhibition is more important in the context of the production of inhibitors "green" or harmless for the environment. This has been studied as inhibitor to corrosion of stainless steel 304L in solution of hydrochloric acid. Corrosive environments have been prepared from a stock solution of sodium chloride and hydrochloric acid solution 1 mol L^{-1}. Adenina was being dissolved in a concentration in the range of 0,1-10 mmol L^{-1} in solutions of HCl 1.0 mol L^{-1} (pH 1,5). For each experiment were used freshly prepared solutions. The study of the degree of Tafel polarization has shown that adenina acts as a mixed inhibitor. The effectiveness of the inhibition increased in direct proportion with the concentration of adenina. The adsorption of the adenine it has been demonstrated that appears on the surface of the stainless steel 304L IS according to Langmuir izoterm [6].

Norfloxacin and ciprofloxacin have been used as inhibitors of corrosion to protect the stainless steel 304 in solution of NaCl 1,5%. The results obtained from an analysis of the effect of the inhibitor by electrochemical methods and by potentiodinamic polarization have shown that these compounds are very good corrosion inhibitors and the highest performance has been recorded at concentration of 1800 ppb. The potentiodinamic curves have indicated that they are anodic corrosion inhibitors [5].

In numerous studies, drugs were investigated as inhibitors of corrosion for different substrate, using the electrochemical measurements associated with different techniques of examination and analysis of the surface: SEM, XPS, optical microscopy. Studies have the purpose of reintroduction into the circuit under different forms of drug with time expired, such as: sulfacetamide [7, 8]; sulfathiazole [9, 10]; aminophylline [11]; quinine [12]; trimethoprim [13]; ampicillin [2, 14]; trihydrate [14]; cephalexin [15]; ciprofloxacin and norfloxacin [5, 16]; doxycycline [17]; eritromicinin [18]; streptomycin [19, 20]; rodanina [21]; metronidazole [22].

This work presents the testing of the bioactive compound metronidazole in various concentrations as corrosion inhibitor for 304L stainless steel in

different environments: HCl 1.0 mol L^{-1} and NaCl 1.0 mol L^{-1} followed by a comparative study of steel behaviour in solutions containing aminoacids and acetic acid.

2. MATERIALS AND METHODS

2. 1. Materials

304L stainless steel plates (area 2.0 cm^2) with the composition: 10-12 % Ni; 18-20 % Cr; 1-2 % Mn, the remaining is iron were submitted to corrosion in: 1.0 mol L^{-1} HCl solution; 1.0 mol L^{-1} NaCl solution; Aminosteril and 1.0 mol L^{-1} acetic acid. The Aminosteril composition is given in Table 1. This steel is used for the manufacture of packaging of food storage (canned); and in some cases a bioimplant.

Metronidazole (MNZ) form part of the group of drugs called anti-infectious agents used in the treatment of some infections caused by micro-organisms susceptible to metronidazole (bacteria, parasites), such as: - amoebiaza (infection caused by a parasite), - tricomoniaza peritonitis (urinary tract infections or genital organs determined by a parasite called Trichomonas) - vaginits (genital women infections determined by bacteria), - giardiasis (parasitic infection), - the treatment of the curative infections medical-surgical by anaerob sensitive germs, - in the prevention of infections that appear during surgical operations with the molecular structure (Fig. 1).

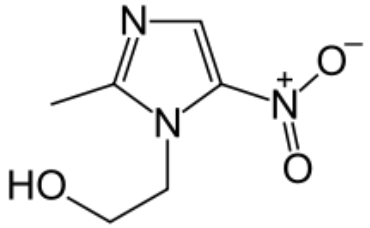

Figure 1. The molecular structure of the metronidazole

Table 1. The Aminosteril composition

Compound	C (g L^{-1})
L-isoleucine (2-amino-3-methylpentanoic acid)	10.40
L-leucine (2-amino-4-methyl-pentanoic acid)	13.09
L-lysin	6.88
L-cysteine (α-amino-β- Thio-propanoic acid)	1.1
L-methionine (2-amino-4- (methiltio) butanoic acid)	0.52
L-phenylalanine (2-amino-3-phenylpropanoic acid)	0.88
L-threonine (2-amino-3-hydroxybutanoic acid)	4.4
L-tryptophan	0.70

L-valine (2-amino-3-methylbutanoic acid)	10.08
L-arginine (2-amino-5-guanidinopentanoic acid)	10.72
L-histidine (2-amino-3- (1H-imidazol-4-yl) propanoic acid)	2.8
Glycine (aminoetanoic acid)	5.08
L-alanine (2-amino-propanoic acid)	4.64
L-proline (pyrrolidine-2-carboxylic acid)	5.73
L-serine (2-amino-3-hydroxypropanoic acid)	2.24
glacial acetic acid	4.42

2.2. Methods

2.2.1. Electrochemical measurements

The potentiodinamic polarization has been carried with a potential scan rate of 1.0 mV s^{-1}, after immersion time of electrodes at open circuit of 4.0 minutes. Thus, it has been determined the corrosion current density (i_{corr}) and the polarization resistance (R_p) for 304L stainless steel corroded in different solutions, as follows: 1.0 mol L^{-1} HCl and 1.0 mol L^{-1} NaCl blank solutions and in 1.0 mol L^{-1} HCl and 1.0 mol L^{-1} NaCl solutions containing various concentrations of metronidazole: 0.2 mmol L^{-1}; 0.4 mmol L^{-1}, 0.6 mmol L^{-1}; 0.8 mmol L^{-1} and 1.0 mmol L^{-1}, as well as in 1.0 mol L^{-1} CH_3COOH and Aminosteril. The electrochemical measurements were performed using a potentiostat/galvanostat Volta Lab 40 with VoltaMaster 4 software. A standard electrochemical cell with three electrodes was used: a work electrode made from 304L stainless steel; an auxiliary electrode of platinum; a reference electrode of Ag/AgCl [23].

2.2.2. The optical microscopy

The morphology of the electrode surfaces of stainless steel 304L, before and after the corrosion in the solutions: 1.0 mol L^{-1} HCl; 1.0 mol L^{-1} NaCl; 1.0 mol L^{-1} CH_3COOH and Aminosteril has been examined by means of a metallographic microscope, type Euromex with Canon camera and included software [23].

3. RESULTS AND DISCUSSION

3.1. The corrosion inhibition of 304L stainless steel in hydrochloric acid solution

The potentiodinamic polarization curves are presented in Fig. 2. It should be noted that: (i) in presence of MNZ the curves of polarization are

moved in the positive direction and lowest areas of current; (ii) the corrosion potential (E_{corr}) moves in the positive direction; this is associated with the decrease of the current density (i_{corr}) and with the increasing of polarization resistance (R_p); (ii) thus, MNZ behaves like a corrosion inhibitor for 304L stainless steel acting by adsorption on the surface of the alloy [23].

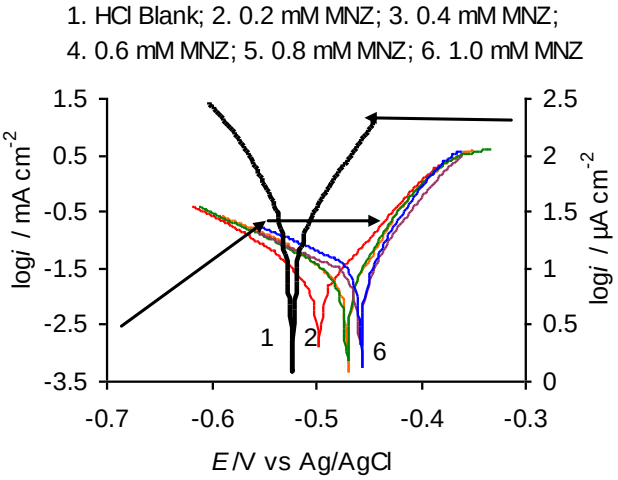

Figure 2. The potentiodinamic polarization curves recorded for stainless 304L steel corroded in 1.0 mol L^{-1} HCl solution, without and with MNZ [23]

The electrochemical parameters were determined using the software VoltaMaster 4, being listed in the Table 2. The inhibition efficiency (*EI* %) has been determined using the relationship 1.

$$EI = \frac{i^{o}_{cor} - i_{cor}}{i^{o}_{cor}} \times 100 \qquad (1)$$

where i^{o}_{corr} is the corrosion current density for solution without inhibitor and i_{corr} is the corrosion current density for the solution containing the MNZ.

Table 2. The electrochemical parameters and efficiency of inhibition calculated for 304L stainless steel corroded in 1.0 mol L^{-1} HCl solution, in the absence and in the presence of the MNZ, at room temperature [23]

Nr. crt.	C-MNZ/ mmol L^{-1}	E_{cor}/ mV vs. Ag/AgCl	i_{cor}/ μA cm^{-2}	R_p/ Ω cm^2	*EI* %
1	0	-522.2	58.6	39.4	0
2	0.2	-497.3	46.0	43.9	21.5
3	0.4	-470.5	30.0	44.0	48.8
4	0.6	-471.1	25.7	49.6	56.2
5	0.8	-457.9	25.4	61.3	56.7
6	1.0	-456.6	20.0	76.2	65.9

from Table 1 it can be observed that: (i) if the concentration of corrosion inhibitor increases the corrosion current decreases while the polarization resistance increases; (ii) the same trend of *IE* is observed reaching a value of 65.9 %, at a concentration of MNZ of 1.0 mol L^{-1}.

3.2. Corrosion of 304L stainless steel in NaCl 1.0 mol L^{-1}solution

The behaviour of 304L stainless steel in NaCl 1.0 mol L^{-1}solution without and with MNZ was determinated by recording the polarization curves followed by their processing as semilogarithmic anodic and cathodic curves. As in the previous case, corrosion current density was calculated at intersection of Tafel lines at corrosion potensial [23]. As shown in Fig. 3, the following characteristics of polarization curves may be observed: the curves polarization were moved in the positive direction; this movement is dependent by the concentration of the inhibitor; it is noted that for concentrations of 0.4 mol L^{-1} and 0.6 mol L^{-1} curves are overlayed, the same phenomenon was also observed for MNZ concentrations of 0.8 mol L^{-1} and 1.0 mol L^{-1}; on the curve obtained for the concentration of 0.2 mol L^{-1} MNZ are not observed significant changes of the two processes, anodic and cathodic; MNZ concentrations less affects the corrosion of 304L stainless steel in NaCl compared to that took place in HCl solution, the corrosion current and the polarization resistances having close values; corrosion current reaches the values between 8.0 and 10.0 μA cm^{-2} and the polarization resistances values ranged from 4.39 to 5.11 kΩ cm^2 [23].

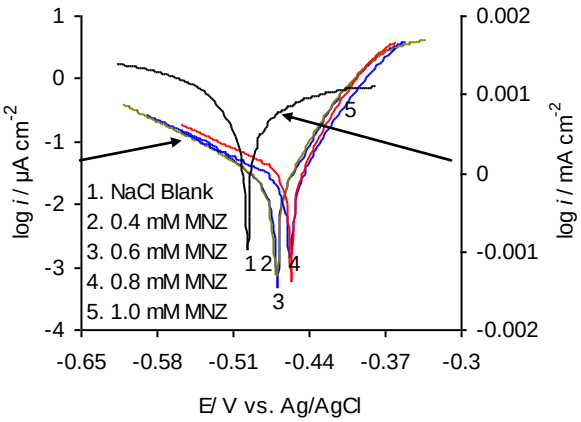

Figure 3. The polarization curves recorded for 304L stainless steel corroded 1.0 mol L^{-1} NaCl solution, in the absence and in the presence of the MNZ [23]

Consequently, MNZ is an inhibitor less efficient for corrosion of 304L stainless steel in solution of NaCl. This can be explained by the appearance of a passive layer to the alloy/electrolyte interface which reduces the oxidation processes, even in the absence of the inhibitor. The phenomenon can be associated with spontaneous passivation of 304L stainless steel in NaCl solution.

3.3. The comparative study on the corrosion behaviour of 304L stainless steel corrosion in different types of environments

The study was carried out in 1.0 mol L^{-1} acetic acid solution and in Aminosteril that contains acetic acid as *pH*-stabilizer. The results were compared with those were obtained in the HCl and NaCl solutions. The polarization curves are shown in Fig. 4. It can be observed that, in the 1.0 mol L^{-1} HCl solution the corrosion is the most intense, much afterwards NaCl. In acetic acid, the stainless steel has reduced susceptibility, corrosion current having a value of 6.0 µA cm^{-2} and the polarization resistance value reaching a value of 10.4 kΩ cm^2. In the presence of Aminosteril, the corrosion potential was shifted in the negative direction influencing both processes, anodic and cathodic, without significantly change of the value of the current corrosion, in relation to the one obtained in acetic acid solution and in NaCl solution. Thus, corrosion of 304L stainless steel in environments are concerned varies as follows: HCl > NaCl > CH_3COOH ≥ Aminosteril. These results show that this steel has a resistance to corrosion very good in studied solutions [23].

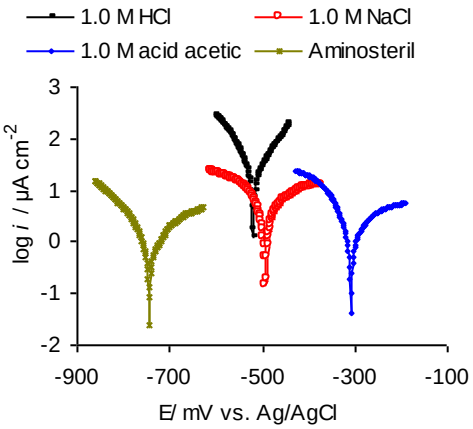

Figure 4. The polarization curves obtained for the 304L stainless steel in: 1.0 mol L^{-1} HCl solution; 1.0 mol L^{-1} NaCl solution; 1.0 mol L^{-1} CH_3COOH solution; Aminosteril [23]

3.4. Optical microscopy

In order to support the commented above, the samples of 304L stainless steel were analyzed by optical microscopy (Fig. 5).

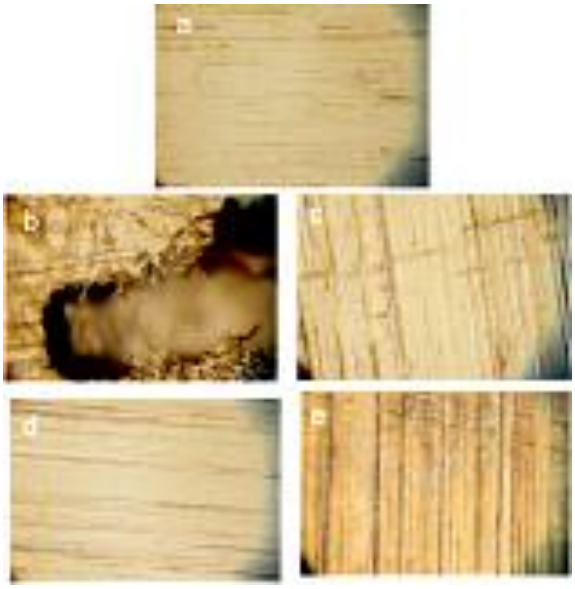

Figure 5. The optical images for 304L stainless steel: a - standard sample; b - after corrosion in HCl; c - after corrosion in NaCl; d - after corrosion in acetic acid; e - after corrosion in Aminosteril [23]

Fig. 5b pointed the steel corrosion very intense in HCl with the formation of cavities and significant modification of the morphology of the surface. In NaCl (Fig. 5c), the steel surface is covered by a protective thin layer, the morphology of the surface being easily changed compared with the standard (Fig. 5a). In acetic acid (Fig. 5d), the surface characteristics are almost unchanged, no items who can reveal points of corrosion which would affect the overall texture or the morphology. In Aminosteril (Fig. 5e) is a record the formation of a film with a folded appearance, but the uniformity or its stability in time could not be discussed [23].

4. CONCLUSIONS

Metronidazole has been investigated as corrosion inhibitor for 304L stainless steel following solutions: 1.0 mol L^{-1} HCl; 1.0 mol L^{-1} NaCl; 1.0 mol L^{-1} CH_3COOH and Aminosteril, using the potentiodynamic polarization and optical microscopy.

The MNZ presence in 1.0 mol L^{-1} HCl solution highlighted the increasing of polarization resistance and subtracting the corrosion current with the increase in the concentration of MNZ.

The MNZ concentration less affects the corrosion of 304L stainless steel in NaCl compared with that in the HCl solution, corrosion current and the polarization resistance having regard value close to those obtained in the blank solution. Thus, MNZ is an inhibitor less efficient for corrosion of 304L stainless steel in solution of NaCl. This can be explained by the appearance of a passive layer to the alloy/electrolyte interface which reduces the oxidation processes even in the absence of the inhibitor.

The corrosion resistance of 304L stainless steel in the four environments varies as follows: HCl > NaCl > CH_3COOH ≥ Aminosteril.

The potentiodinamic polarization indicated that the MNZ in 1.0 mol L^{-1} HCl solution and 1.0 mol L^{-1} NaCl solution acts as an inhibitor anodic and in solution of aminosteril MNZ is a mixed inhibitor suppressing both processes: anodic and cathodic. In acetic acid steel has reduced susceptibility.

The optical images have shown significant modification of the morphology of the area in the case of the sample corroded in HCl, in NaCl surface morphology is slightly different from that of the standard sample. In acetic acid surface characteristics are almost unchanged, no items that highlights the corrosion spots which would affect the overall texture or the morphology. In Aminosteril is recorded the formation of a film with folded aspect.

References

1. U. Kamachimudali, T. M. Sridhar, B. Raj, *Sadhana*, 28 (**2003**) 601.
2. A.S. Fouda, H.M. El-Abbasy, *Corrosion*, 68 (**2012**) 1.
3. M. Shabani-Nooshabadi, M. S. Ghandchi, J. Ind. Eng. Chem. 31 (**2015**) 231.
4. A. Samide, B. Tutunaru, *Inhibitori de coroziune*, Ed. Sitech, Craiova, **2014**.
5. R.S. Dubei, Yogesh Potdar, Indian *J. Chem. Tech*., 16 (**2009**) 334.
6. M. Scendo, J. Trela, *Int. J. Electrochem. Sci*., 8 (**2013**) 9201.
7. A. Samide, B. Tutunaru, C. Negrila, I. Trandafir, A. Maxut, *Digest J. Nanomater. Biostruct*., 6 (**2011**) 663.
8. A. Samide, B. Tutunaru, C. Negrila, A. Dobritescu, *J. Therm. Anal. Calorim*., 110 (**2012**) 145.
9. A. Samide, B. Tutunaru, *Chem. Biochem. Eng*. Q., 25 (**2011**) 299.
10. A. Samide, B. Tutunaru, Catalin Negrila, I. Prunaru, *Spectrosc. Lett*., 45 (**2012**) 55.
11. A. Samide, B. Tutunaru, C. Ionescu, P. Rotaru, L. Simoiu, *J. Therm. Anal. Calorim*., 118 (**2014**) 631.
12. A. Samide, B. Tutunaru, *Centr. Eur. J. Chem*., 12 (**2014**) 901.
13. A. Samide, J. Env. Sci. Heal. Part A., 48 (**2013**) 159.
14. N.O. Eddy, U.J. Ibok, E.E. Ebenso, A. El Nemr, E.S.H El Ashry, *J. Molec. Model*., 15 (**2009**) 1085.
15. M. Abdallah, *Corros. Sci*., 46 (2004)1981.
16. S.K. Shukla, M.A. Quraishi, *Mater. Chem. Phys*., 120 (**2010**) 142.
17. X.H. Pang, W.J. Guo, W.H. Li, J.D. Xie, B.R. Hou, *Sci. China Series B: Chem*., 51 (**2008**) 928.
18. S.K. Shukla, M.A. Quraishi, *Corros. Sci*., 314 (**2010**) 314.
19. N.O. Eddy, S.A. Odoemelam, E.C. Ogoko, B.I. Ita, *Port. Electrochim. Acta*, 28 (**2010**) 15.
20. S.K. Shukla, A.K. Singh, I. Ahamad, M.A. Quraishi, *Mater. Lett*., 63 (**2009**) 819.
21. M. Abdallah, *Corros. Sci*., 44 (**2002**) 717.
22. A. Samide, B. Tutunaru, A. Dobrițescu, P. Ilea, A.C. Vladu, C. Tigae, *Int. J. Electrochem. Sci*., 11 (**2016**) 5520.
23. R. Ghita, Dissertation Work, Master - Chemistry of Biologically Active Compounds, Title: *„Efectul unor compuşi bioactivi asupra degradării oţelului inoxidabil 304L utilizat ca bioimplant"/ Effect of some bioactive compounds on the degradation of 304L stainless steel used as bioimplant, Department of Chemistry, Faculty of Sciences, University of Craiova*, **2016**.

Annals of the University of Craiova
The Chemistry Series
Volume XLIV, No. 1 (2017) 13-25
homepage: chimie.ucv.ro/anale/

Study on the inhibition of wheat bran acid phosphatase activity

Research article

Georgeta Ciobanu, Cătălina Ionescu, Andreea Eliescu, Monica Mateescu*

University of Craiova, Faculty of Sciences, Department of Chemistry, Calea Bucuresti, 107i, Craiova, Romania
*e-mail: geo_ciobanu20@yahoo.com

Received: 18.02.2017 / Accepted: 15.03.2017 / Published: 10.05.2017

Abstract
We have prepared and tested for acid phosphatase activity a proteic extract from wheat bran. The pH-activity profile of acid phosphatase pointed out an optimal value at 4.8, and the parameters inferred from the Michaelis-Menten kinetic study were: V_{max}= 42.32 μmol L^{-1} min^{-1} and K_M=0.8 mmol L^{-1}. Acid phosphatase activity was inhibited by phosphate and molybdate, resistant to tartrate and rather activated by zinc cations, at concentrations of 1 mmol L^{-1}. The inhibitory effect of some fluoride containing personal care products indicated that acid phosphatase from wheat bran is also fluoride-sensitive.

Keywords: acid phosphatase; wheat bran; enzyme kinetics and inhibition

1. INTRODUCTION

The design of enzyme inhibitors for various applications is based on the screening of a library of molecules, in terms of inhibitory effect on the enzyme of interest. The starting point of our study was an experiment conducted with our students, using acid phosphatase from wheat bran as target enzyme [1]. Non-specific phosphatases with optimal acidic pH (EC 3.1.3.2) are apparently ubiquitous throughout the living world. Studies on mammalian acid phosphatase were driven by the observation that disruption of their activity

correlates with pathological conditions [2]. These enzymes are involved not only in phosphate acquisition but are also acting as part of important regulatory and signaling processes. Although numerous studies refer to the enzymes found in animals and plants [2-5], there is also evidence for acid phosphatase activity in fungi [6] and bacteria [7]. Phosphatases catalyze the hydrolysis reaction of orthophosphoric monoesters (scheme 1) having either small or high molecular mass:

Orthophosphoric monoester + $H_2O \rightarrow$ alcohol + H_3PO_4 (Scheme 1)

Being a large and diverse group of enzymes, phosphatases are difficult to grasp in a simple classification scheme; they can be classified according to several criteria [2, 5]. In terms of substrate specificity, there are non-specific phosphatases that can dephosphorylate a wide range of substrates, and phosphatases strictly specific for certain phosphorylated small molecules or side chains of amino acids in proteins (*i.e.* Ser, Tyr and Thr). Non-specific phosphatases are further divided according to the optimum pH for their action *in vitro*, as acidic or alkaline. Another criterion for phosphatases classification is the catalytic mechanism. Phosphatase-catalyzed hydrolysis of phosphoric monoesters occurs in certain cases with the formation of a covalent enzyme-substrate intermediate, by transferring of the phosphate group from the substrate to a cysteine (Cys) or histidine (His) residue in the active site of the enzyme. In other cases, catalysis is assisted by metal cations in enzyme's structure. Acting as Lewis acids, structural cations aid catalysis by activating of a water molecule that will accept the phosphate leaving group from the substrate [8].

The aim of our study was to characterize the acid phosphatase activity of a proteic extract from wheat bran in terms of optimum pH, kinetic parameters and preliminary testing for enzyme inhibitors.

2. MATERIALS AND METHODS

2.1. Materials

Analytical grade reagents from Sigma-Aldrich, Roth or Merck were used for all solution preparation. Wheat bran and personal care products were purchased from the local stores.

2.2. Methods

2.2.1. Enzyme extraction and assay

Wheat bran was suspended in 0.1 mol L^{-1} CH_3COOH-CH_3COONa buffer, pH 5.0, at 1:5 (m/V) ratio. The suspension was kept at room temperature for 2 hours, and stirred from time to time. Large, insoluble material was removed by filtration through several layers of cheesecloth. The filtrate was centrifuged at 10,000 rpm and 4°C for 10 minutes, in a refrigerated Sigma K-216 centrifuge. The obtained supernatants were used to assess phosphatase activity with optimum pH in the acidic range, without further purification (crude extract).

Acid phosphatase activity was assayed using *p*-nitrophenyl phosphate (pNPP) as a substrate, at pH 5 and 25°C [9]. In this method, the colourless product, *p*-nitrophenol (pNP), released by substrate hydrolysis, turns into the yellow-coloured *p*-nitrophenolate when the reaction is stopped by alkalinisation with NaOH. Each sample was accompanied by a blank with the same composition, except that enzyme extract was added after the NaOH solution.

Absorbances of the samples and blanks, recorded at 410 nm, were transformed in concentrations using a standard curve obtained with pNP. Acid phosphatase activity was expressed in units per mL (U mL^{-1}), one unit representing the enzyme quantity that releases 1 μmol of pNP per minute. Total soluble protein content of the extract was assayed using the Bradford method [10], with bovine serum albumin as standard. All the absorbance measurements were done with a Varian Cary 50 UV-Vis spectrophotometer.

2.2.2. pH-optimum for wheat bran acid phosphatase activity

In order to assess the effect of *pH* on enzyme activity, p-NPP hydrolysis was carried out in 0.1 mmol.L^{-1} CH_3COOH-CH_3COONa buffer solutions with pH ranging from 3.6 to 5.6, while substrate and enzyme concentrations were kept constant. The amounts of p-NP released at each of the tested pH values were assayed as described above, and reaction rate was calculated using equation 1.

$$v\ (\mu mol\ L^{-1}\ min^{-1}) = \frac{[\ pNP]_{sample} - [pNP]_{blank}}{t} \qquad (1)$$

where: $[pNP]_{sample}$ and $[pNP]_{blank}$ represent product concentration in the sample and blank respectively, and *t* is the reaction time. The results were plotted (v *vs.* pH) and pH optimum was inferred from nonlinear regression of the data.

2.2.3. Screening for potential inhibitors of wheat bran acid phosphatase

The substances we have tested as potential inhibitors of wheat bran acid phosphatase were: $NaOOC(CHOH)_2COONa$ (sodium tartrate), Na_2MoO_4

(sodium molybdate), 2-(OH)C_6H_4COOH (salicylic acid), $ZnCl_2$ (zinc chloride) and $EDTANa_2$ (ethylenediaminetetraacetic acid disodium salt). The tests were performed at two different concentrations of the substrate (p-NPP), 0.41 mmol L^{-1} and 4.1 mmol L^{-1}, respectively, while inhibitor's concentration in the assay mixture was 1 mmol L^{-1}. All the samples were accompanied by controls, where distilled water was added instead of the test solution.

We have also tested the inhibitory effect of certain personal care products presented in Table 1. To this end, 0.5 g solid product or, where applicable, 1 mL liquid product was brought to 10 mL with distilled water. The obtained suspension was shaken in order to dissolve the soluble components, while the insoluble ones were removed by centrifugation [1]. The supernatants were decanted and used for the inhibition tests, 0.5 mL per sample at a final volume of 3 mL. Substrate concentration in the samples was 0.41 mmol L^{-1} at a constant enzyme quantity (0.1 mL crude extract) and reaction time (5 min).
For all the tests, reaction rate was calculated as described above and the obtained results were used to infer the relative rate of reaction in the presence of the tested substances compared to control (v_r, Equation 2), as well as the degree of inhibition of phosphatase reaction (I, Equation 3).

$$v_r\ (\%) = 100 \times \frac{v_{sample}}{v_{control}} \qquad (2)$$

$$I\ (\%) = 100 \times \frac{v_{control} - v_{sample}}{v_{control}} \qquad (3)$$

2.2.4. Kinetic study of the reaction catalysed by wheat bran acid phosphatase

Wheat bran acid phosphatase-catalysed hydrolysis of p-NPP was carried out at pH 5 and substrate concentrations varying from 0.133 mmol L^{-1} to 8.33 mmol L^{-1}, at constant enzyme concentration, either in the absence (control) or the presence of certain inhibitors. The experimental setup remained unchanged compared to control, except for the presence of the inhibitors.

Reaction rates calculated as previously described were plotted *vs.* substrate concentration, and the kinetic parameters: K_M (the Michaelis constant), V_{max} (the maximal reaction rate) and the inhibition constant (K_I) were inferred from nonlinear regression of the data [11].

Table 1a. Personal care products screened as wheat bran acid phosphatase inhibitors: dental care products

Categories	Product type	Probe number	Specifications & ingredients
Dental care products	Toothpaste	1	Medicinal; aqua, hydrated silica, sorbitol, silica, disodium phosphate, PEG-32, poloxamer 188, tetrapotassium pyrophosphate, sodium lauryl sulfate, aroma, cellulose gum, sodium fluoride (1357 ppm), titanium dioxide, aluminium lactate, sodium saccharin, methylparabene, propylparabene, eugenol, limonene.
	Toothpaste	2	Complete protection for sensitive teeth; agycerin, PEG-8, hydrated silica, calcium sodium phosphate, aroma, sodium lauryl sulfate, sodium monofluorophosphate 1.08% w/w (1450 ppm F^-), titanium dioxide, carbomer, sodium saccharin, eugenol, limonene.
	Toothpaste	3	Helps gum stop bleeding; sodium bicarbonate, aqua, glycerin alcohol, cocamidopropyl betaine, *Krameria triandra* extract, *Echinaceea purpureea* flower/leaf/stem juice, aroma, xanthan gum, *Chamomilla recutita* extract, *Commiphora myrtha* extract, sodium fluoride 0.31% w/w (1400 ppm F^-), sodium saccharin, sodium benzoate, *Salvia officinalis* oil, *Mentha piperitha* oil, *Mentha arvensis* oil, limonene, linalool, CI 77491.
	Toothpaste	4	Total protection, pro gum health; aqua, hydrated silica, glycerin, sorbitol, PVM/MA copolymer, sodium lauryl sulfate, aroma, CI 77891, cellulose gum, sodium hydroxide, sodium fluoride (1450 ppm F^-), carrageenan, sodium saccharin, triclosan, limonene.
	Mouthwash	5	Long lasting sensitivity protection; aqua, glycerin, sorbitol, potassium nitrate (3% w/w), PEG-60 hydrogenated castor oil, poloxamer 407, sodium benzoate, aroma, disodium phosphate, methylparaben, propylparaben, sodium phosphate, sodium fluoride 0.048%w/w (217 ppm), sodium saccharide, CI42090.

Table 1b. Personal care products screened as wheat bran acid phosphatase inhibitors: soaps and detergents

Categories	Product type	Probe number	Ingredients
Soaps and detergents	Liquid soap	6	Aqua, sodium laureth sulfate, sodium chloride, cocamidopropyl betaine, cocamide DEA, parfum, limonene, glycerin, citric acid, linalool, sodium benzoate, benzophenone-4, methyl-chloroisothiazolinone, magnesium nitrate, magnesium chloride, methylisothiazolinone, CI15985, CI19140.
	Liquid soap	7	Alcohol, glycerin, lauril glucoside, *Punica granatum* extract, xanthan gum, *Butyrospermum parkii* butter, sodium ceterayl sulfate, sodium cocoyl glutamate, disodium cocoyl glutamate, tocopherol, *Helianthus annuus* seed oil, perfume, linalool, limonene, geraniol
	Liquid soap	8	Aqua, sodium laurethyl sulphate, cocamide DEA, sodium chloride, cocamidopropyl betaine, glycerin, phenoxiethanol, methylparaben, buthylparaben, perfume, PEG-7-glyceryl cocoate, 2-bromo-2-nitro, 1,3-propanediol, citric acid, citronellol, linalool, CI14720.
	Liquid soap	9	Aqua, sodium C12-13 pareth sulfate, sodium laureth sulfate, cocamidopropyl betaine, sodium chloride, cocamide MEA, perfume, sodium salicylate, sodium benzoate, poliquaternium-7, styrene/ acrylates copolymer, citric acid, tetrasodium EDTA, sine adipe lac, *Aloe barbadensis* leaf extract, *Olea europea* oil, limonene, linalool.
	Dishwash liquid	10	5-15% anionic surfactants, <5% nonionic surfactants, benzisothiazolinona, phenoxyethanol, perfume, hexil cinnamal, limonene.

2.2.5. K_M, V_{max} and K_I calculation

V_{max} and K_M were determined by measuring the reaction rate at various concentrations of the substrate, considering that the enzyme operates according to the Michaelis-Menten model described by Equation 4:

$$v = \frac{V_{max} \cdot [S]}{K_M + [S]} \quad (4)$$

We have also calculated the same parameters using the double-reciprocal Lineweaver-Burk plot (Equation 5):

$$\frac{1}{v} = \frac{K_M}{V_{max}} \frac{1}{[S]} + \frac{1}{V_{max}} \quad (5)$$

Non-linear regression of the kinetic data inferred from the inhibition tests were used for the apparent kinetic parameters (K_M^{ap}, V_{max}^{ap}) calculation and inhibition type identification, as well as for K_I calculation. A more general form of the Michaelis-Menten equation for reversible inhibition was used, that accounts for both EI and ESI complexes formation (Equation 6), assuming that the inhibitors may bind both the free enzyme (E) and the enzyme-substrate complex (ES):

$$v = \frac{V_{max} \cdot [S]}{\alpha K_M + \alpha'[S]} = \frac{(1/\alpha')V_{max} \cdot [S]}{(\alpha/\alpha')K_M + [S]} \quad (6)$$

where α and α' are modifying factors depending on both inhibitor's concentration [I] and inhibition constants, as it follows (Equation 7 and 8):

$$\alpha = 1 + \frac{[I]}{K_I} \quad (7)$$

$$\alpha' = 1 + \frac{[I]}{K_I'} \quad (8)$$

K_I and K_I' represent the dissociation constants of EI and ESI, respectively. Thus, α=α'=1 for the uninhibited enzyme, α>1 for competitive inhibition (increased K_M^{app} values), α'>1 for uncompetitive inhibition (decreased K_M^{app} and V_{max}^{app} values), while mixed type inhibition is characterised by both α and α' values greater than 1 (decreased V_{max}^{app}; K_M^{app} may increase or decrease) [12].

3. RESULTS AND DISCUSSION

3.1. pH-activity profile of wheat bran acid phosphatase

Protein concentration in the wheat bran crude extract was 80 μg mL^{-1} and acid phosphatase activity with p-NPP as substrate was 800 mU mL^{-1}, *i.e* 10 U mg^{-1} protein. The reaction rate of enzyme-catalysed p-NPP hydrolysis was plotted *vs.* pH values ranging from 3.6 to 5.6, yielding a bell-shaped curve with a maximum at 4.8 (Figure 1). Enzyme activity sharply decreased at pH values below 4.4 and above 5.6, as suggested the symmetric shape of the nonlinear regression of the data (gaussian, R^2 = 0.9866). Thus, one can conclude that

wheat bran acid phosphatase is active in a narrow pH domain centred on value 4.8. This pH-activity profile of the enzyme might be correlated with a role of acid phosphatase in phosphorus mobilisation as phosphate, during germination, and is suggestive for enzyme's localisation within the vacuole.

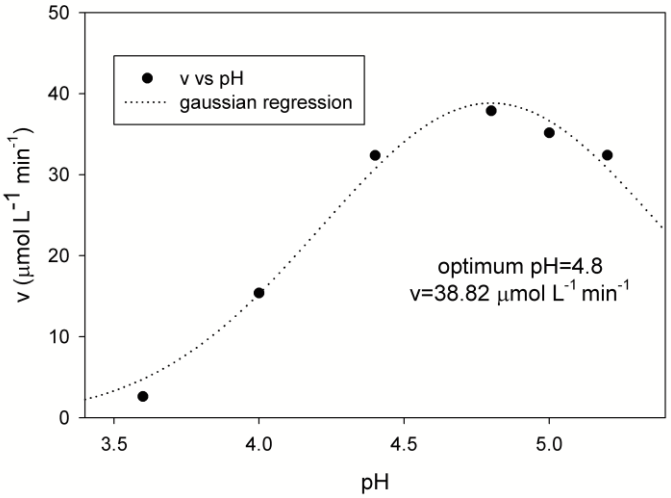

Figure 1. pH-activity profile of wheat bran acid phosphatase

3.2. Results of the screening for potential inhibitors of wheat bran acid phosphatase

The catalytic activity of an enzyme depends on its three-dimensional architecture, on the amino-acid side-chains and prosthetic groups present at the active site, that are involved in substrate binding and transformation, as well as on the existence of other specific sites that can bind different allosteric effectors. Thus, any substance or form of energy that affects an enzyme's native conformation or hinder somehow the productive substrate binding would diminish its catalytic efficiency. The obtained results of the screening for phosphatase activity inhibitors (section 2.4) are presented in table 2.

Among the tested substances in this experiment, only molybdate has shown an appreciable inhibition of wheat bran acid phosphatase activity. Whith 1 mmol L^{-1} sodium molybdate, the degree of inhibition was 80% compared to control at substrate's concentration of 0.41 mmol.L^{-1}, but decreased to 63% when substrate concentration increased 10 times. Attenuation of the inhibition at growing concentrations of the substrate is characteristic for competitive inhibition. Thus, our data suggested that molybdate acted as a competitive inhibitor. In the other cases, rather than the expected inhibition, an activation of acid phosphatase was observed.

Table 2. Relative reaction rate (v_r) for p-NPP hydrolysis catalysed by wheat bran acid phosphatase, in the presence of certain substances tested as potential enzyme inhibitors.

Probe	*C-inhibitor*/ mmol L^{-1}	v_r / %	
		pNPP 0.41 mmol L^{-1}	pNPP 4.1 mmol L^{-1}
Control	0	100.00	100.00
$NaOOC(CHOH)_2COONa$	1	112.68	134.17
Na_2MoO_4	1	19.74	36.90
$2^-(HO)C_6H_4CO_2H$	1	106.70	269.77
$ZnCl_2$	1	135.17	156.87
$EDTANa_2$	1	175.40	123.02

Another substance we have tested was salicylic acid, whose structure contains the phenylen moiety also present in pNPP, the substrate widely used for phosphatases assay. Thus, is expected that the benzene ring to match the active site of acid phosphatase. For example, literature data presented salicylic acid as the starting point for the synthesis of a library of inhibitors targeting protein tyrosine phosphatase SPH2 as anti-cancer and anti-leukemia therapy [13]. However, efficient and specific inhibitors must target not only the catalytic site of an enzyme, but also adjacent and peripheral sites. It appears that solely the presence of a benzene ring is not enough for a tight binding at the active site. Also, the catalytic mechanism of the abovementioned protein phosphatase may be different from that of wheat bran acid phosphatase.

As for the personal care products, the results showed that, in the tested amounts, they had, without exception, a strong inhibitory effect, over 40%, on phosphatase activity (Table 3).

Considering the ingredients of the tested dental hygiene products (Table 2a), we have noticed that all of them contained fluoride, mostly as NaF. Like molybdate and wolframate, fluoride (F^-) is a strong nucleophile that may bind to the active site of a metalohydrolase, inhibiting its action [4, 5, 8]. The hypothesis that fluoride was at least in part responsible for the inhibitory effect of the products presented in table 1a is consistent with the observation that among the dental care products, the one having the lowest fluoride content had also the lowest inhibitory effect in the screening.

Table 3. The degree of inhibition, I, of wheat bran acid phosphatase activity inferred from the screening of personal care products

Significance	Variant	v/ mmol.min^{-1}L^{-1}	I/ %
H_2O	Control (-)	11.44	0
KH_2PO_4 3 mmol L^{-1}	Control (+)	7.37	35.55
Toothpaste	1	0.48	95.79
Toothpaste	2	0,53	95.38
Toothpaste	3	3.35	70.74
Toothpaste	4	0.8	93.03
Mouthwash	5	4.89	57.23
Liquid soap	6	0.48	95.77
Liquid soap	7	2.17	81.03
Liquid soap	8	2.9	74.64
Liquid soap	9	0.53	95.38
Dishwashing liquid	10	0.68	94.07

Various phosphates are also among the common ingredients in toothpaste formulations. As inorganic phosphate is one of the end-products of phosphatase-catalysed reaction, it is part of enzyme's substrate and has a complementary shape with a region in its active site. Thus, phosphate may competitively bind to the active site of acid phosphatase, inhibiting its activity. In fact, competitive inhibition by phosphate is well-documented for various types of phosphatases [14].

The observed effects in the experiments with soaps and detergent (Table 2b) could be ascribed to the presence of significant amounts of surfactants that may destabilize or distort the native conformation of the enzyme, acting rather in an unspecific manner in the given conditions. Repeating the experiments at higher dilutions of these products could bring more information. It's also important to keep in mind that all the tested products were mixtures of substances which may cause interactive effects, *e.g* cooperativity, as observed by Qin et al. in case of fluoride and phosphate binding at Mg^{2+} in enolase's active site [15].

We continued with the phosphatase inhibitors quest by testing the inhibitory effect of the screened products on a wider range of substrate concentrations, while enzyme's concentration remained constant (section 2.5). We have formally ascribed the concentration 1 mmol L^{-1} to the 'inhibitory cocktails' derived from the personal care products (section 2.4), as was the concentration of KH_2PO_4 considered as positive control for the kinetic study of enzyme inhibition. By doing so, we had the possibility to compare the effects of

the probes within the inhibition kinetic study. The obtained results are presented in figure 2 and table 3.

Data on the effect of 1 mmol L^{-1} KH_2PO_4 on acid phosphatase activity pointed out an increase of K_M value compared to control, while V_{max} didn't vary significantly (table 3). Such an effect is characteristic for competitive inhibition, being consistent with the expected response and literature data. As regards the experiments with personal care products, it is obvious that both the K_M and V_{max} values significantly varied compared to control, suggesting that a mixed-type inhibition effect occurred (table 3). This assumption is also sustained by the Lineweaver-Burk plots where the linear regressions of kinetic data intercepts are between the axes rather than on the axes (1/c or 1/v).

The value of the calculated competitive inhibition constant (K_I) for KH_2PO_4 is quite high (in the millimolar range), a possible explanation being that the experiments were carried out with crude enzyme extracts that might contain substances with protective effect for enzyme activity. However, comparing the values of K_I and K_I', the non-competitive inhibition is ruled out as the latter is 15 folds greater than the former.

Taking into account that K_I meaning is generally comparable with IC_{50}, both representing the concentration that leads to 50% inhibition of the tested parameter it is hard to imagine the physiological efficiency of an inhibitor at such a high concentration. In terms of physiological signification, the competitive inhibition exerted by the reaction products is a feedback loop that equilibrates production with demand, avoiding wastage.

Table 3 Kinetic parameters inferred from the nonlinear regressions of the data (ligand binding type, one parameter, R^2>0.96) for acid phosphatase reaction in the presence of selected inhibitors from the preliminary tests with personal care products (Table 1, a and b). For comparison, data on phosphatase activity in the absence of inhibitors, as well as in the presence of 1 mmol L^{-1} KH_2PO_4 are also presented.

	control	KH_2PO_4 1 mol L^{-1}	toothpaste (1)	toothpaste (3)	liquid soap (8)	liquid soap (9)
V_{max}/ μmol L^{-1} min^{-1}	42.32	40.97	9.01	36.36	11.49	12.95
K_M/ mmol L^{-1}	0.80	1.15	3.11	1.86	2.14	0.48
K_I/mmol L^{-1}	-	2.06	0.06	0.59	0.11	1.06
K_I'/mmol L^{-1}	-	30.35	0.27	6.10	0.37	0.44

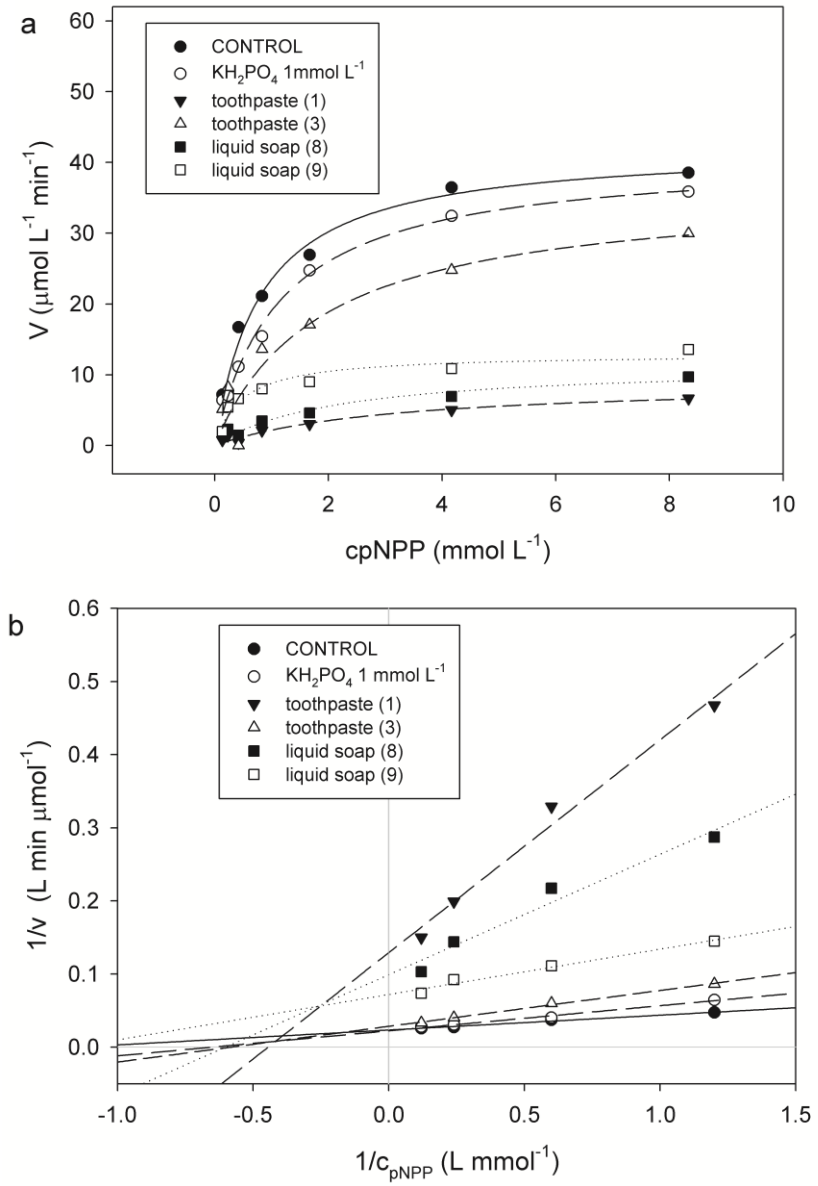

Figure 2. The Michaelis-Menten (a) and Lineweaver-Burk (b) plots for pNNP hydrolysis catalyzed by wheat bran acid phosphatase, for certain probes from the enzyme inhibition screening with personal care products (table 1, a and b) and KH_2PO_4 as positive control

4. CONCLUSIONS

Acid phosphatase activity from wheat bran has an optimum pH at 4.8, sugestive for the location of the enzyme within the vacuole of the aleurone cell layer in wheat grain, as well as for a role in phosphate mobilisation during germination. Kinetic study of wheat bran acid phosphatase revealed a maximum reaction rate of 42.32 μmol L^{-1} min^{-1} and a Michaelis-Menten costant of 0.8 mmol L^{-1} for p-nitrophenylphosphate as a substrate. KH_2PO_4 was confirmed as a competitive inhibitor of phosphatase activity, with a K_I value of 2.06 mmol L^{-1}. Other substances that inhibited phosphatase activity were sodium molybdate and probably fluoride (in the toothpastes formulations).

References

1. A. T.S. Taylor, *Biochem. Mol. Biol. Educ*., 33 (**2004**) 16.
2. C. L. Araujo and P. T.Vihko, *Methods. Mol. Biol*., 1053 (**2013**) 155.
3. D. J. Rigden, *Biochem. J*., 409 (**2008**) 333.
4. G. Schenk, T. W.Elliott, E. Leung, L. E .Carrington, N. Mitic, L. R. Gahan and L. W. Guddat, *BMC Struct. Biol*., 8 (**2008**) 6.
5. G. Dionisio, C. K. Madsen, P. B. Holm, K. G. Welinder, M. Jørgensen, E. Stoger, E. Arcalis, and H. Brinch-Pedersen, *Plant Physiol*., 156 (**2011**) 1087.
6. A.L. Freitas-Mesquita and J. R. Meyer-Fernandes, *Int. J. Mol. Sci*., 15 (**2014**) 2289.
7. N. U. Gandhi and S. B. Chandra, *Acta Inform. Med*., 20 (**2012**) 167.
8. F. Rusnak, P. Mertz, *Physiol. Rev.*, 80 (**2000**) 1483.
9. D. Sharma, N. Shing and J. K. Kang, *Gen. App. Plant Physiol*. 31 (**2005**) 71.
10. M. M. Bradford, *Anal. Biochem.*, 72 (**1976**) 248.
11. N. Price, L. Stevens, *Fundamentals of Enzymology-Cell and Molecular Biology of Catalytic Proteins*, 3rd ed., Oxford University Press Inc., New York (**2001**).
12. D. Voet, J. G.Voet, and C. W. Pratt, *Fundamentals of Biochemistry, Life at the molecular level*, 4th ed., John Wiley & Sons, New York (**2013**).
13. X. Zhang, Y. He, S. Liu, Z. Yu, Z.X. Jiang, Z. Yang, Y. Dong, S. C. Nabinger, L. Wu, A. M. Gunawan, L. Wang, R. J. Chan and Z.Yin. Zhang, *J. Med. Chem*., 53 (**2010**) 2482.
14. P. K. Srivastava and A. Anand, *Prep. Biochem Biotechnol*., 45 (2015) 33.
15. J. Qin, G. Chai, J. M. Brewer, L. L. Lovelace and L. Lebioda, *Biochemistry*, 45 (**2006**) 793.

Annals of the University of Craiova
The Chemistry Series
Volume XLIV No. 1 (2017) 26-35
homepage: chimie.ucv.ro/anale/

The electrodeposition of composite coatings based on Sn/CeO_2; their surface chemistry and corrosion behaviour

Research article

Bogdan Tutunaru, Ioana Prunaru, Monica Mateescu

University of Craiova, Faculty of Sciences, Department of Chemistry, Craiova, Romania
*e-mail: tutunaruchim@yahoo.com

Received: 25.01.2017 / *Accepted*: 14.03.2017 / *Published*: 10.05.2017

Abstract
The development of corrosion protection systems for metallic substrates has been extensively investigated. In this work the composite coatings based on Sn/CeO_2 were prepared by electrodeposition on carbon steel surface from acidic bath containing sulfacetamide (SA), as a new additive. Scanning electron microscopy (SEM) was used to observe the surface morphology of deposits. The corrosion resistance of composite coating in 0.1 mol L^{-1} HCl solution was studied by potentiodynamic polarization and electrochemical impedance spectroscopy (EIS). Corrosion current (i_{corr}) measurements and charge transfer resistance (R_{ct}) values reveal the increased corrosion resistance and maximum protection of carbon steel surface.

Keywords: electrodeposited coating; metal matrix composite; cerium oxide; corrosion resistance

1. INTRODUCTION

The corrosion in pipes, pumps, turbine blades, coolers, water heaters, and other systems made of carbon steel causes enormous industrial expenses due to production downtime, accidental injuries, and replacement costs. The steel is an important metal in industrial applications, but it can be corroded in aqueous solutions, such as hydrochloric acid, because the Cl^- ions significantly promote the corrosion process [1-4]. For this reason, protection of metal surfaces against corrosion using effective methods involving inhibition or electrodeposition of coatings is necessary [1-8]

The composite material can be described as a mixture of materials specially designed for satisfying certain technological requirements, improving the desired properties of the components and reducing the undesirable properties of the same materials.

The development of composite materials has been extensively investigated in recent years. The combination a wide variety of compositions and production processes had permitted the use of these materials in different applications like coatings for corrosion protection of metals, abrasion resistant coatings and for repair and rehabilitation of concrete structures [9-13]. The metal matrix composite materials is an area of great interest, the composite layers providing superior electrical, optical, magnetic, mechanical, physical and chemical properties (e.g. excellent wear resistance and corrosion resistance) [5-12, 14].

Different compounds such as: SiC [15, 16], $CeO_2/Al_2O_3/Y_2O_3$ [6, 17-19] have been co-electrodeposited with nickel. Tin matrix was also used to obtain the effective protective composite coatings with Al_2O_3 [20] and $Zr_{0.74}Y_{0.16}Ti_{0.10}O_{2-\delta}$ [5].

The aim of this work was to investigate the surface chemistry and corrosion resistance of composite coatings based on Sn/CeO_2; these were electrodeposed on carbon steel surface from acidic bath, containing 10^{-2} mol L^{-1} sulfacetamide, IUPAC name N-[(4-aminophenyl) sulfonyl] acetamide (SA), as additive. The choice of SA, as additive, is based on the fact that it acts as corrosion inhibitor for carbon steel in acidic media [4] by suppressing simultaneously the cathodic and anodic processes, via adsorption on carbon steel surface [4]; anodic dissolution and cathodic hydrogen evolution reaction were both inhibited by this inhibitor through merely blocking the reaction sites of carbon steel surface [4]. Therefore, SA inhibits the formation of iron corrosion products which may infest the composite coating, during electrodeposition process. Moreover, SA is a sulfa drug which was healthy reported and very important in biological reactions (environmentally friendly); it acts as antimicrobial agents by inhibiting bacterial growth; it is easily soluble in water.

2. MATERIALS AND METHODS

2.1. Materials

The composite coating was electrodeposited on carbon steel surface, with the following composition: C = 0.1%, Mn = 0.5%, P = 0.025%, S = 0.025%, Fe remainder. The electrolyte bath for composite electrodeposition was prepared using 0.1 mol L^{-1} HCl solution containing 0.25 mol L^{-1} $SnCl_2$, 10^{-2} mol L^{-1} sulfacetamide (SA), as additive, and 2 g L^{-1} CeO_2 powder. All reagents were obtained from Fluka.

2.2. Methods

2.2.1. Sn/CeO_2 electrodeposition

The experiments were carried out in a standard electrochemical cell with a cathode made of carbon steel plate of 2x2x0.1 cm size and platinum plate used as anode. The plating bath has functioned at room temperature at different current densities. The cathodes were weighed before and after deposition and the electrodeposition efficiency (η) was calculated.

Before electrodeposition, the specimens were successively polished with 200, 600, 800 grade of emery paper, ultrasonically cleaned with bi-distilled water, degreased with acetone, and then stored in a vacuum desiccator. The pH (1.1 ± 0.05) of the electrolytic bath was measured using a digital pH-meter (Hanna instruments). To ensure a uniform dispersion of CeO_2 micro-particles, the electrolyte was stirred for 2 h, before the deposition. The stirring rate was kept constant at 300 rpm. The electrodeposition was performed with Keithley 2420 3A Source Meter potentiostat/galvanostat, at room temperature.

The deposits obtained at different current densities were observed visually and by scanning electron microscopy using a Vega Tescan Model microscope.

2.2.2. Corrosion tests

The corrosion resistance of Sn/CeO_2 was evaluated and it was compared to the corrosion resistance of carbon steel uncovered. The polarization behaviour was studied in 0.1 mol L^{-1} HCl solution, for electrodeposition efficiency (η) of 95.4 %. The electrodeposited specimens were marked to expose 1 cm^2 area on one side.

Electrochemical measurements were conducted using an electrochemical system, VoltaLab 40, with a personal computer and VoltaMaster 4 software. A standard corrosion cell was used. A platinum plate (1.0 cm^2) and $Ag/AgCl_{sat}$ electrode were used as auxiliary and reference

electrodes, respectively. The immersion time of the plates in 0.1 mol L^{-1} HCl solution, was 30 minutes in open circuit, at room temperature. Potentiodynamic polarization curves were obtained with the scan rate of 1.0 mV s^{-1}.

Electrochemical impedance spectroscopy (EIS) was measured in a frequency range from 10^5 Hz to 10^{-1} Hz by a parturition signal of 10.0 mV amplitude peak to peak at room temperature, after the immersion time of 30 minutes in open circuit.

3. RESULTS AND DISCUSSION

3.1. Electrodeposition of coatings

3.1.1. Electrodeposition efficiency

The operating parameters, time of deposition and current densities are given in Table 1. Electrodeposition efficiency (η) was calculated using Eq.1.

$$\eta = \frac{m_d}{m_t} \cdot 100 \qquad (1)$$

m_d is mass of Sn/CeO_2 deposit; $m_d = m_f - m_i$; where m_i is mass of carbon steel specimen before deposition; m_f is mass of sample after deposition.
The values of m_t were calculated from Faraday's law, Eq.2

$$m_t = \frac{A}{zF} \cdot I \cdot t \qquad (2)$$

m_t (g) is total mass of the substance which can be liberated at electrode; A is atomic mass of tin (118.7); z is the valence number of ions; F = 26.5 (A h) is the Faraday constant; I (A) is current intensity; t (h) is the total time, which the constant current was applied. The values obtained for η and visual appearance of coatings are given in Table 1.

Note that at low current densities matte deposits were obtained and carbon steel surface was partially covered. At current densities of 2.5 A dm^{-2} and 3 A dm^{-2} at high electrodeposition time, thick and non-adherent layers were deposited. Thus, the favorable deposits were obtained at: (i) current density of 2.5 A dm^{-2}, deposition time of 20 min.; (ii) 3 A dm^{-2}, deposition time of 15 min.; (iii) 3 A dm^{-2}, deposition time of 20 min. These deposits were analyzed using scanning electron microscopy (Fig. 1). However, the parameters modify the quality of the deposit, probably by incorporation in the metallic matrix different amount of tin and cerium oxides.

Table 1. Deposition efficiency and visual appearance of tin/cerium oxide composite electrodeposited from acidic baths containing sulfacetamide as additive, at room temperature at different current densities

Current density / A dm^{-2}	Time/ min	m_t/ g	m_d/ g	η/ %	Visual appearance of coatings
1.5 A dm^{-2} A = 0.04 dm^{-2} I = 0.06 A	5	0.0112	0.0044	39.6	Matte white
	10	0.0215	0.0086	40.2	Matte white
	15	0.0336	0.0136	40.6	Matte white
	20	0.0448	0.0184	41.1	Matte white
	25	0.056	0.0233	41.7	Matte white
	30	0.0672	0.0283	42.1	Matte white
2.0 A dm^{-2} A = 0.04 dm^{-2} I = 0.08 A	5	0.0149	0.0088	59.2	Matte white
	10	0.0298	0.0184	61.8	Matte white
	15	0.0447	0.0283	63.4	Matte white
	20	0.0596	0.0392	65.8	Matte white
	25	0.0745	0.0508	68.2	Matte white
	30	0.0895	0.0639	71.4	Silvery white
2.5 A dm^{-2} A = 0.04 dm^{-2} I = 0.1 A	5	0.0186	0.015	83.6	Silvery white
	10	0.0373	0.032	86.8	Silvery white
	15	0.056	0.0506	90.3	Silvery white
	20	0.0746	0.0706	94.6	Silvery white
	25	0.093	-	-	thick and non-adherent deposit
	30	0.112	-	-	thick and non-adherent deposit
3.0 A dm^{-2} A = 0.04 dm^{-2} I = 0.12 A	5	0.0223	0.0193	86.4	Silvery white
	10	0.0446	0.0405	90.8	Silvery white
	15	0.067	0.0626	93.5	Silvery white
	20	0.089	0.0849	95.4	Silvery white
	25	0.112	-	-	thick and non-adherent deposit
	30	0.134	-	-	thick and non-adherent deposit

3.2. Morphology of coatings. SEM images

The morphology and texture of tin coatings are important. The surface morphology of tin coatings examined by scanning electron microscopy (SEM) is shown in Fig. 1. Figs. 1b and 1c show deposits produced at 2.5 A dm^{-2}, and 3.0 A dm^{-2} for deposition time of 20 min and 15 min., respectively. In both cases the formation of specific layers is observed, with block-like tin crystals. Fig. 1d shows that SEM of electrodeposited tin obtained at current density of 3.0 A dm^{-2} (electrodeposition time of 20 min.) has a more regular surface morphology, suggesting that the coating is quite dense with no tendency to dendrite formation. The layer uniformity is more apparent and the feature of a metallic nucleation, forming a matrix in which are embedded certain oxide particles is nuanced.

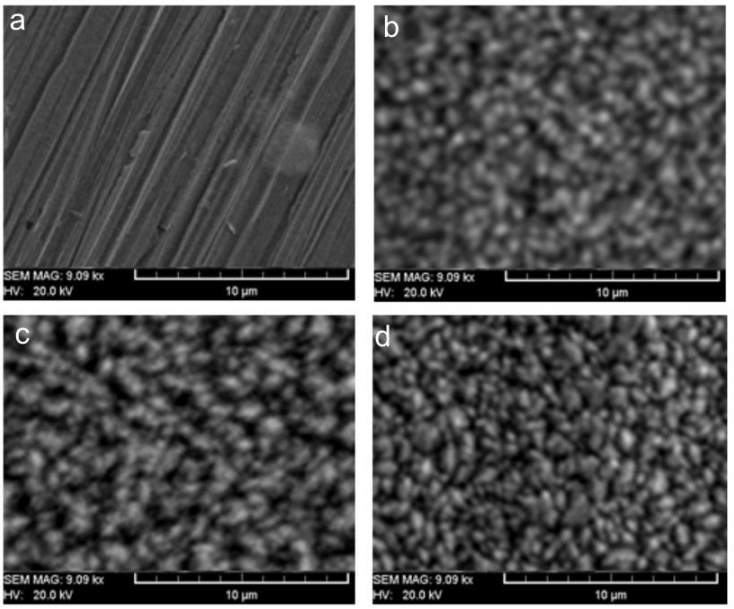

Figure 1. SEM images of: a - carbon steel substrate; b – Sn/CeO_2 deposit obtained at current density of 2.5 A dm^{-2}, deposition time of 20 min; c – Sn/CeO_2 deposit obtained at current density of 3 A dm^{-2}, deposition time of 15 min; d – Sn/CeO_2 deposit obtained at current density of 3 A dm^{-2}, deposition time of 20 min

3.3. Corrosion tests

The corrosion resistance of uncovered and covered carbon steel with Sn/CeO_2 deposit was investigated in 0.1 mol L^{-1} HCl solution using electrochemical measurements such as: potentiodynamic polarization and electrochemical impedance spectroscopy (EIS).

3.3.1. Potentiodynamic polarization

Polarization curves obtained in 0.1 mol L^{-1} HCl solution, for the corrosion of carbon steel uncovered and covered with composite coating, after immersion time of the electrode at its E_{corr} for 30 min, are shown in Fig. 2a.

The performed tests showed that: (i) the curves are shifted to lower current region, showing the better protection tendency of composite coating; (ii) the curves shifted to lower current region is correlate with a significant corrosion current decrease; (iii) the presence of deposit on carbon steel surface disturbs significantly cathodic reaction and reduces the anodic dissolution in a considerable manner.

The electrochemical parameters such as: corrosion potential (E_{corr}), corrosion current density (i_{corr}), anodic (b_a) and cathodic (b_c) Tafel slopes derived from polarization curves, and corresponding protection efficiency P(%) value for deposit, are given in Table 2. The protection efficiency was calculated using Eq. 3 [5, 6]:

$$P = \frac{i'_{corr} - i_{corr}}{i'_{corr}} \cdot 100 \qquad (3)$$

where i'_{corr} and i_{corr} are the corrosion current densities of uncovered and covered carbon steel, respectively.

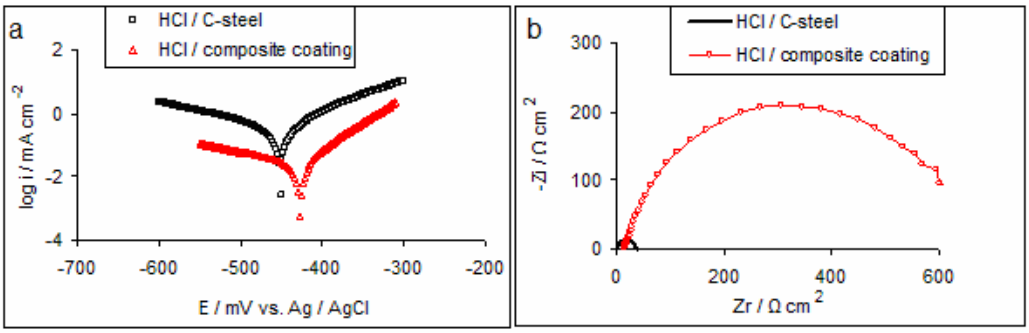

Figure 2. Electrochemical measurements result for corrosion behaviour:
a - potentiodynamic curves of carbon steel uncovered and covered with composite deposit, after corrosion in 0.1 mol L^{-1} HCl solution, at room temperature; b - Nyquist diagram of carbon steel uncovered and covered with composite deposit, exposed in 0.1 mol L^{-1} HCl solution, at room temperature.

3.3.2. Electrochemical impedance spectroscopy (EIS)

The electrochemical impedance measurements for all investigated samples in 0.1 mol L^{-1} HCl solution were carried out at the open circuit potential, after immersion time of 30 minutes, in the frequency range from 10^5 to 10^{-1} Hz, with a value of 10 mV for the amplitude. Fig. 2b shows Nyquist plots of investigated uncovered and covered carbon steel. It is also apparent from these plots that the Nyquist curves (Fig. 2b) consist of one capacitive loop. More pronounced frequency arc was obtained for the sample coated with composite deposit.

The equivalent circuit involves only one time constant [R_s - (R_{ct} - C_{dl})], fits well the experimental results. The intersection of the capacitive loop with the real axis represents the charge transfer resistance (R_{ct}), at very low frequencies, and the electrolytic resistance (R_s), at very high frequencies which enclosed between the working electrode and the reference one.

The double layer capacitance (C_{dl}) was derived from frequency, at which the imaginary component of the impedance (Z_{imax}) was maximal using the relationship, Eq. 4 [21-23]:

$$f(-Z_{i\max}) = \frac{1}{2\pi C_{dl} R_{ct}} \qquad (4)$$

The impedance parameters derived from EIS measurements R_s, R_{ct}, C_{dl} were calculated using VoltaMaster 4 software with an error of ±1 %, and are listed in Table 2.

The protection efficiency P (%) was determined by the following relationship, Eq. 5 [5, 6]:

$$P = \left(\frac{R_{ct} - R_{ct}^0}{R_{ct}} \right) \cdot 100 \qquad (5)$$

where R_{ct} and R_{ct}^0 represent the charge transfer resistances in the presence and the absence of composite deposit.

Table 2. Electrochemical parameters and protection efficiency (P) obtained from electrochemical measurements for corrosion of uncovered and covered carbon steel in 0.1 mol L^{-1} HCl solution, at room temperature

	Electrochemical results								
	From potentiodynamic polarization					From EIS			
C-steel	E_{corr}/ mV vs.Ag/ AgCl	i_{corr}/ mA cm^{-2}	b_a/ mV dec^{-1}	b_c/ mV dec^{-1}	P/ %	R_s/ Ω cm^2	C_{dl}/ μF cm^{-2}	R_{ct}/ Ω cm^2	P/ %
standard	-450	0.794	110	153	0	3.89	259.7	37.4	0
covered	-428	0.014	63	185	98.2	20.86	135.8	654.8	94.2

The inspection of the data in Table 2 reveals that the composite deposit increases R_{ct} and decreases i_{corr} and C_{dl}, and consequently enhances P%, reaching a value of 96.2 ± 2 %. It can be seen that the values of protection efficiency obtained from potentiodynamic polarization and EIS measurements are in good agreement.

Similar results were obtained in other studies [5, 6, 15-20], proving that the composite layers obtained by codeposition of metals and some oxide particles present a better adhesion and higher corrosion resistance than those obtained by the electrodeposition of pure metals. Consequently, protection efficiency increases with the increase of polarization resistance, while the corrosion current density decreases. The same trend of the composite deposits was observed compared to pure nickel or tin coatings obtained by electrodeposition [5, 6, 19, 20].

3.3.3. SEM observation

The SEM images of unprotected (Fig. 3a) and protected (Fig. 3b) carbon steel surface after occurrence of corrosive processes in 0.1 mol L^{-1} HCl solution are presented. In case of unprotected carbon steel surface corroded in 0.1 mol L^{-1} HCl solution random spread corrosion spots can be observed (Fig. 3a). When carbon steel surface was protected with Sn/CeO_2 (Fig. 3b) deposit, the texture was modified and the corrosion spots had a low intensity. It can be observed that the surface morphology shown in this case, is significantly different and more regular than that obtained for uncovered carbon steel surface. Moreover, metallic nucleation, although less nuanced than before corrosion is still observed, attesting the deposit stability and adhesion on carbon steel surface.

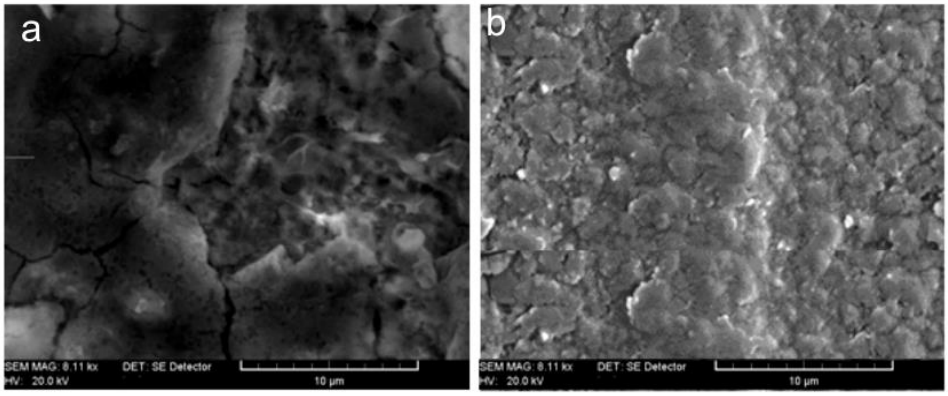

Figure 3. SEM images of: a - carbon steel substrate after corrosion in 0.1 mol L^{-1} HCl solution, at room temperature; b - Sn / CeO_2 deposit obtained at current density of 3 A dm^{-2}, deposition time of 20 min after corrosion in 0.1 mol L^{-1} HCl solution, at room temperature.

4. CONCLUSIONS

In this work the composite coatings based on Sn/CeO2 were prepared by electrodeposition on carbon steel surface from acidic bath, containing sulfacetamide (SA), as a new additive.

The choice of SA, as additive, for electrodeposition baths, is based on: (i) it acts as corrosion inhibitor for carbon steel in acidic media, inducing the better occurrence management of iron compounds during electrodeposition, avoiding the infestation of coatings with rust; (ii) sulfacetamide (SA) favors electrodeposition of metallic tin in greater proportion than that of tin oxides.

SEM images confirm the layer uniformity and that the feature of a metallic nucleation, forming a matrix in which tin oxides and cerium oxide

micro-particles may be embedded. Also, after corrosion the surface texture was modified without corrosion spots being evidenced.

Moreover, the corrosion behaviour of composite coatings was evaluated in acidic environment. Electrochemical measurements revealed a maximum protection of carbon steel surface, reaching a value of 96±2%.

References

1. A. S. Fouda, M. Abdallah, A. Attia, *Chem. Eng. Commun*., 197 (**2010**) 1091.
2. A. Samide, *J. Environ. Sci. Health A Tox. Hazard. Subst. Environ. Eng.*, 48 (**2013**) 159.
3. A. Samide, E. Turcanu, I. Bibicu, *Chem. Eng. Commun.*, 196 (**2009**) 1008.
4. A. Samide, B. Tutunaru, C. Negrila, I. Trandafir, A. Maxut, *Digest J. Nanomater. Biostruct.*, 6 (**2011**) 663.
5. A. Samide, A. Maxut, N. Cioatera, M. Preda, *Rev. Chim.*, 61 (**2010**) 439.
6. A. Samide, B. Tutunaru, *Chem. Biochem. Eng., Q.* 25 (**2011**) 203.
7. S. Kunst, E. Leal Da Silva, L. Antonini, J. Matos, C. Oliveira, C. Malfatti, *J. Chil. Chem. Soc.*, 57 (**2012**) 1464.
8. S. P. Fakrudeen, A. Murthyh. C, B. Raju V. *J. Chil. Chem. Soc.*, 57 (**2012**) 1364.
9. Y. S. Huang, X. T. Zeng, X. F. Hu, F. M. Liu, *Electrochim. Acta*. 49 (**2004**) 4313.
10. B. Szczygieł, M. Kołodziej, *Electrochim. Acta.* 50 (**2005**) 4188.
11. Z. Zeng, J. Zhang, *Surf. Coat. Tech.*, 202 (**2008**) 2725.
12. P. S. Sidky, M. G. Hocking, *Brit. Corros. J.*, 34 (**1999**) 171.
13. M. Chen, S. Das, *Steel Compos. Struct.*, 9 (**2009**) 103.
14. T. Markley, S. Dligatch, A. Trinchi, T. H. Muster, A. Bendavid, P. Martin, D. Lau, A. Bradbury, S. Furman, I. S. Cole, *Corros. Sci.*, 52 (**2010**) 3847.
15. A. F. Zimmerman, D. G. Clark, K. T. Aust, U. Erb, *Mat. Lett.*, 52 (**2002**) 85.
16. M. Rostami, A. Fahami, B. Nasiri-Tabrizi, R. Ebrahimi-Kahrizsangi, A. Saatchi, *Appl. Surf. Sci*., 265 (**2013**) 369.
17. A. Lozano-Morales, E. J. Podlaha, *J. Appl. Electrochem.*, 38 (**2008**) 1707.
18. S.T. Aruna, V. K. W. Grips, V. E. Selvi, K. S. Rajam, K. S., *J. Appl. Electrochem*., 37 (**2007**) 991.
19. N. Cioatera, A. Samide, A. Maxut, R. N. Vannier, M. Traisnel, *Rev. Roum. Chim.*, 56 (**2011**) 1003.
20. A. Samide, B. Tutunaru, *Adv. Sci. Lett.*, 19 (**2013**) 224.
21. A.S. Fouda, H.A. Mostafa, H.M. El-Abbasy, *J. Appl. Electrochem*., 40 (**2010**) 163.
22. M.I. Awad, *J. Appl. Electrochem*., 36 (**2006**) 1163.
23. B. Zerga, A. Attayibat, M. Sfaira, M. Taleb, B. Hammouti, M. Ebn Touhami, S. Radi, Z. Rais, *J. Appl. Electrochem*., 40 (**2010**) 1575.

Annals of the University of Craiova
The Chemistry Series
Volume XLIV, No. 1 (2017) 36-45
homepage: chimie.ucv.ro/anale/

Comparative study on the biochemical and physiological effects of Cd, Cu and Zn in wheat plants

Research article

Georgeta Ciobanu[*], *Cătălina Ionescu, Monica Mateescu*

University of Craiova, Faculty of Sciences, Department of Chemistry, Calea Bucuresti, 107i, Craiova, Romania
*e-mail: geo_ciobanu20@yahoo.com

Received: 18.01.2017 / *Accepted*: 19.03.2017 / *Published*: 10.05.2017

Abstract
Wheat seedlings grown on media with excess Cd^{2+}, Cu^{2+} and Zn^{2+}, ranging from 1 μmol L^{-1} to 500 μmol L^{-1}, presented a dose-dependent growth inhibition. Toxicity ranking of the three tested metals pointed out copper as the most harmful, with an EC_{50} value of 0.08 mmol L^{-1} for root elongation inhibition, zinc being the least toxic while Cd^{2+}occupied an intermediate position. Although growth inhibition was not observed in wheat plants exposed to lower levels of heavy metal cations, certain biochemical parameters were suggestive for the onset of defense responses. Increased peroxidase activity and glucose concentration, as well as decreased levels of chlorophylls and carotenoids, appeared as general, unspecific effects in wheat plants, subsequent to heavy metal exposure.

Keywords: heavy metals; wheat plants; growth inhibition; biochemical effects

1. INTRODUCTION

Heavy metals pollution is a real concern throughout the world, as many anthropic sources led to increased levels of these metals in different environmental compartments [1]. Even essential metals may become very toxic when specific thresholds are exceeded. For plants, soil is the main reservoir of microelements whose excess or deficit can be passed to higher trophic levels.

We aimed to assess and compare the effects of heavy metal excess on certain biochemical and physiological parameters in wheat plants. For the first part of our study, whose results are presented below, we chose three metals which adjoin each other in the periodic table of elements and often in nature, namely copper (Cu), zinc (Zn) and cadmium (Cd). In the second part of the study, we have evaluated wheat plants responses to chromium (Cr) treatment when applied in two different oxidation states; the obtained results will be presented in a separate article.

.

period	group	
	11	12
4	$_{29}$**Cu** $[Ar]3d^{10}4s^{1}$	$_{30}$**Zn** $[Ar]3d^{10}4s^{2}$
5	$_{47}$Ag $[Kr]4d^{10}5s^{1}$	$_{48}$**Cd** $[Kr]4d^{10}5s^{2}$

Figure 1. Copper, zinc and cadmium position in the periodic table of elements (detail), and their electron configuration

Examining their electron configuration and position in the periodic table of elements (Figure 1), it is apparent that the three heavy metals share a common characteristic, namely the *(n-1)d* shell filled with electrons, on top of which the *s* orbital has one electron in Cu, and two electrons in Cd and Zn atoms. The main oxidation state of the abovementioned metals is +2, but only copper may undergo redox reactions *in vivo*. Cu and Zn are essential microelements for all the plants and animals [2-7], while no utile function was documented to date for Cd in higher organisms. Cd is carginogenic to humans [8-10] and a possible estrogen mimetic [11].

Studies on the effects of heavy metal excess upon plants growth, development and biochemistry are needed for understanding the molecular mechanisms underlying toxicity and tolerance of plants toward heavy metals.

2. MATERIALS AND METHODS

2.1. Materials

Wheat grains (*Triticum aestivum* L, cv. PB-1) were obtained from the Agricultural Research and Development Station Simnic, Dolj. All the solutions used in these experiments were prepared with analytical grade reagents.

2.2. Method

2.2.1. Plant cultivation and heavy metal treatment

Surface sterilized wheat caryopses were placed between two layers of filter paper moistened with distilled water, at 4°C in the dark, for 24 hours. Uniformly germinated seeds were transplanted in Petri dishes filled with 50 mL nutrient solution [12] solidified with agar. In order to evaluate the effect of heavy metal cations on plants growth and metabolism, nutrient solutions were supplemented, in separated experiments, with Cd^{2+}, Cu^{2+} and Zn^{2+}, respectively. For each of the abovementioned cations, a series of dilutions ranging from 1 μmol L^{-1} to 500 μmol L^{-1} were obtained within the nutrient solutions, starting from 10 mmol L^{-1} stock solutions of the respective metal chlorides. Each probe was ruled in triplicate, while 3 dishes without heavy metal excess were kept as control (the nutrient solution itself contained 0.04 μmol L^{-1} Zn^{2+} and 0.024 μmol L^{-1} Cu^{2+}).

2.2.2. Plant growth assay

Wheat plants were harvested at seven days after the onset of imbibition, and the length of their root and stem was registered. Data on plant growth were used to calculate the growth inhibition index, GI (equation 1):

$$GI = \frac{L_{\text{control}} - L_{\text{probe}}}{L_{\text{control}}} \times 100 \qquad (1)$$

where $L_{control}$ and L_{probe} represent root or shoot length for the unexposed (control) and heavy metal exposed (probe) plants, respectively.

2.2.3.Biochemical assays

Plants grown at low heavy metal concentrations (1 μmol L^{-1} and 5 μmol L^{-1} respectively), in which no significant growth inhibition was observed, were

also analysed in terms of certain biochemical parameters relevant to heavy metal toxicity. For this purpose, tissue homogenates were obtained from fresh leaf samples by grinding with quartz sand and extraction of the soluble components in 0.1 mol L^{-1} Tris-HCl buffer, at pH 7.0.

The homogenates were centrifuged at 10000 r.p.m. for 10 min, in a Sigma K-216 centrifuge, and the supernatants were used for biochemical analysis. Total soluble protein content was assessed by the Bradford method [13]. Glucose oxidase-peroxidase method was used for glucose determination. Unspecific peroxidase activity (EC 1.11.1.7) was measured with guaiacol as a hydrogen donor [14]. Estimation of the secondary lipid peroxidation products was done by the TBARS assay [15].

Ethanolic extracts of leaf tissue were also obtained, and their absorption spectra in the visible domain were registered in order to assess photosynthetic pigments concentration.Absorbance values at specific wavelengths were used to calculate chlorophylls and carotenoids concentration [16]. Antocyanin content of the leaves was assayed by the pH differential method [17].

A Varian Cary 50 UV-VIS spectrophotometer was used to carry out the spectrophotometric measurements. All the biochemical parameters were expressed per fresh weight (FW) base.

3. RESULTS AND DISCUSSION

3.1. Biometric parameters of wheat plants

Growth parameters of wheat plants exposed to Cd^{2+}, Cu^{2+} and Zn^{2+} are presented in Figure 2.

Under the given circumstances, Zn^{2+} had the weakest effect, plant elongation inhibition occurring at exogenous concentrations exceeding 50 μmol L^{-1}. The maximum Zn^{2+} tested concentration, *i.e.* 500 μmol.L^{-1}, led to about 20% inhibition of both root and stem growth, compared to control. A similar trend of variation was observed in plants grown on media with Cd^{2+}, except that the effect was more intense on roots (60%) and weaker on stems (16%). The most evident effect was in Cu^{2+} treated samples, characterized by marked growth inhibition of stems (66%) and nearly complete of roots (93%), at the highest tested concentration. EC_{50} values for growth inhibition presented in

Table 1 pointed out the following toxic ranking of the heavy metals tested: $Zn^{2+}<Cd^{2+}<<Cu^{2+}$ with respect to root growth, and $Cd^{2+}<Zn^{2+}<<Cu^{2+}$ for stem growth. In all of the three cases, the inhibitory effect was greater on roots, compared to stems. This could be explained by the fact that the roots were exposed to direct contact with heavy metal cations. However, most of the

concentrations shown in Table 1 are unlikely to occur in ecosystems, except for the cases of very intense accidental pollution.

Table 1. EC_{50} values for the inhibitory effect of Cd^{2+}, Cu^{2+} and Zn^{2+} on wheat plants growth

Me^{2+}	*EC*$_{50}$/mmol L^{-1}	
	root	stem
Cd^{2+}	0.36	3.11
Cu^{2+}	0.08	0.35
Zn^{2+}	1.37	1.93

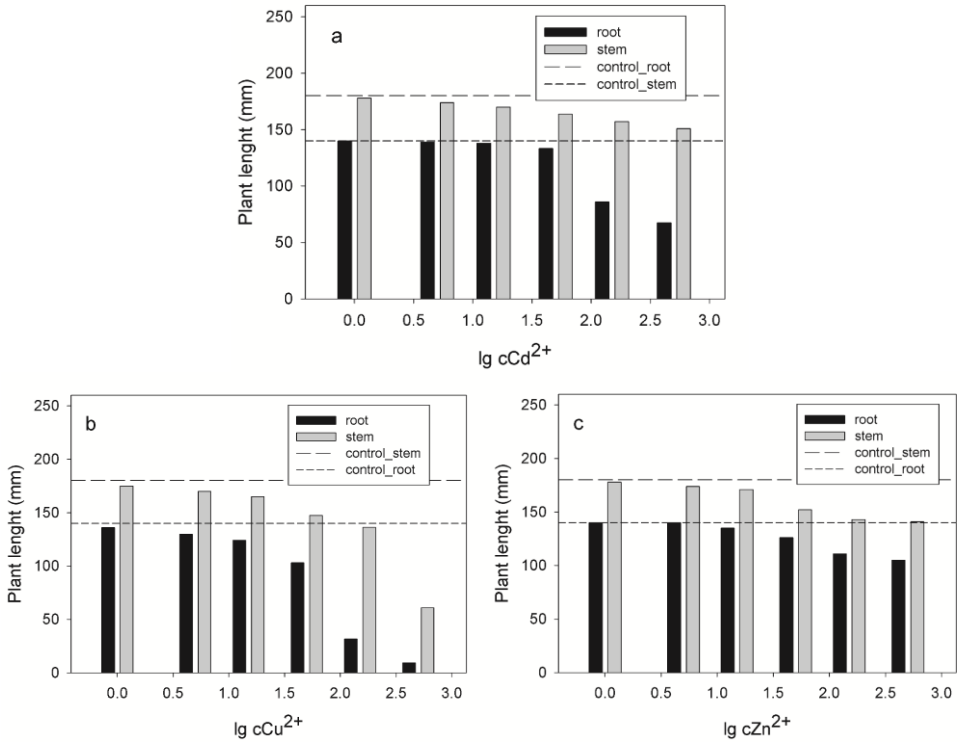

Figure 2. Growth parameters of wheat plants exposed to: a – Cd^{2+}, b – Cu^{2+} and c – Zn^{2+}

3.2. Antioxidant and metabolic indexes of wheat plants exposed to heavy metals

Peroxidase activity in the leaves of wheat plants unexposed to heavy metals was of 2.41 U g^{-1} FW. Enzyme's activity almost doubled compared to control in the leaves of wheat plants exposed to 5 µmol L^{-1} Cd^{2+} and Cu^{2+} respectively, and also increased but to a less extent at 1 µmol L^{-1} Cd^{2+} and 1

μmol L^{-1} Zn^{2+} (Figure 3a). As peroxidase is involved in H_2O_2 detoxification, increased activity might be related to excess generation of hydrogen peroxide. The obtained results suggested that, for each of the tested heavy metals, there is a specific threshold at which peroxidase activity intensifies, to diminish oxidative stress.

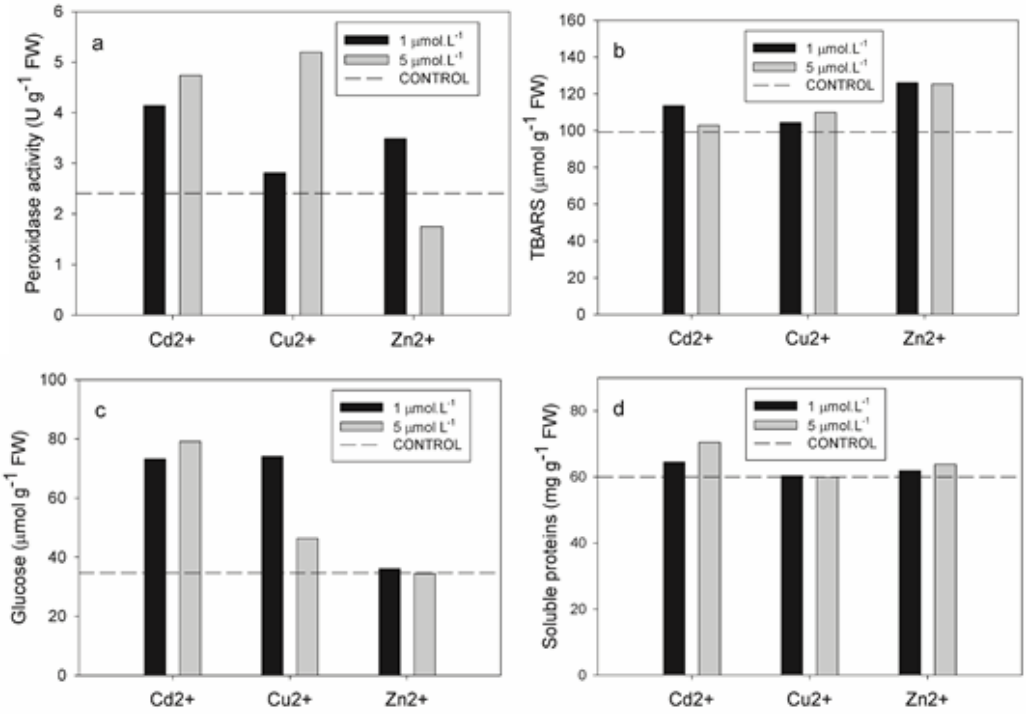

Figure 3. Biochemical parameters of wheat plants exposed to heavy metals: a – peroxidase activity; b – secondary peroxidation products (TBARS); c – glucose; d – soluble proteins. Vertical bars are averages of three measurements; standard deviations did not exceed 10%

Lipid peroxidation. The acronym TBARS (*thiobarbituric reactive substances*) refers to the products of advanced unsaturated lipids peroxidation, especially malondialdehyde and 4-hydroxynonenal. Leaves of wheat plants grown in the absence of contamination by heavy metals had a concentration of TBARS of approximately 100 μmol g^{-1} FW. TBARS concentrations about 10% higher than the amount measured in control were found in the leaves of wheat plants exposed to 1 μmol L^{-1} Cd^{2+} and 5 μmol L^{-1} Cu^{2+} (Figure 3b).

One can conclude that the respective wheat plants didn't experience oxidative stress strong enough to accelerate lipid peroxidation, since just small increases of TBARS concentrations were observed in heavy metal exposed ones compared to control plants. These data might indicate the effectiveness of

antioxidant defense in leaves of the plants grown on media containing excess $Cu^{2+}$and Cd^{2+}. However, a slighter increase of lipid peroxidative damage was noticed in the plants exposed to Zn^{2+}, where TBARS quantity grew by 25 % compared to control at both tested concentrations. Although Zn is not redox active within biological systems, it may generate oxidative stress in plants when present in excess [18]. To summarize, in the given conditions no advanced lipid peroxidation occurred in wheat plants leaves.

Glucose concentration in the leaves of unstressed wheat plants was of 34.69 μmol g^{-1} FW. Glucose content doubled in the plants grown on Cd^{2+} contaminated media, at both concentrations tested (1 μmol L^{-1} and 5 μmol L^{-1}), as well as in those grown at 1 μmol L^{-1} excess Cu^{2+}. In the other cases, glucose concentration didn't change compared to control plants (Figure 3c). Increased content of free glucose can indicate an involvement of this sugar in alleviating osmotic stress that often accompanies the toxic effects of heavy metals, and/or a decline in glucans synthesis.

Proteins are fundamental constituents of the cell, meeting various structural and functional roles. The great majority of soluble proteins in a cell are enzymes, catalysts of biochemical reactions.

Under the given experimental condition, the amount of soluble protein in the leaves of plants exposed to heavy metals didn't vary significantly compared to control, except for Cd^{2+} treatments that were followed by a slight increase of protein content (Figure 3d). These might represent cysteine rich, Cd^{2+}-chelating proteins, as plants are known to synthesize phytochelatins as a defense response to cadmium toxicity. [19].

3.3. Leaf pigments in wheat plants exposed to heavy metals

In wheat plants unexposed to heavy metals, concentrations of the photosynthetic pigments were as it follows: 1.52 μmol g^{-1} FW *total chlorophylls* (comprising 1.12 μmol g^{-1} FW Chl *a* and 0.4 μmol g^{-1} FW Chl *b*) and 0.40 μmol g^{-1} FW *total carotenoids*. Compared to control, leaf pigments concentration in the plants grown on media contaminated with heavy metals decreased as exogenous concentration of metallic cations increased (Fig. 4, a-c).

At 1.0 μmol L^{-1} heavy metal excess, the smallest quantities of pigments were noticed in Zn^{2+} probes, while at 5 μmol L^{-1} the lowest amounts of pigments were in plants contaminated with Cu^{2+}. Although heavy metal treatment was followed by decreased pigment concentration in wheat leaves, Chl a: Chl b ratio didn't register significant variations compared to control (Table 2), except for a slight increase observed in the plants exposed to 5.0 μmol L^{-1} Cu^{2+} and Zn^{2+}.

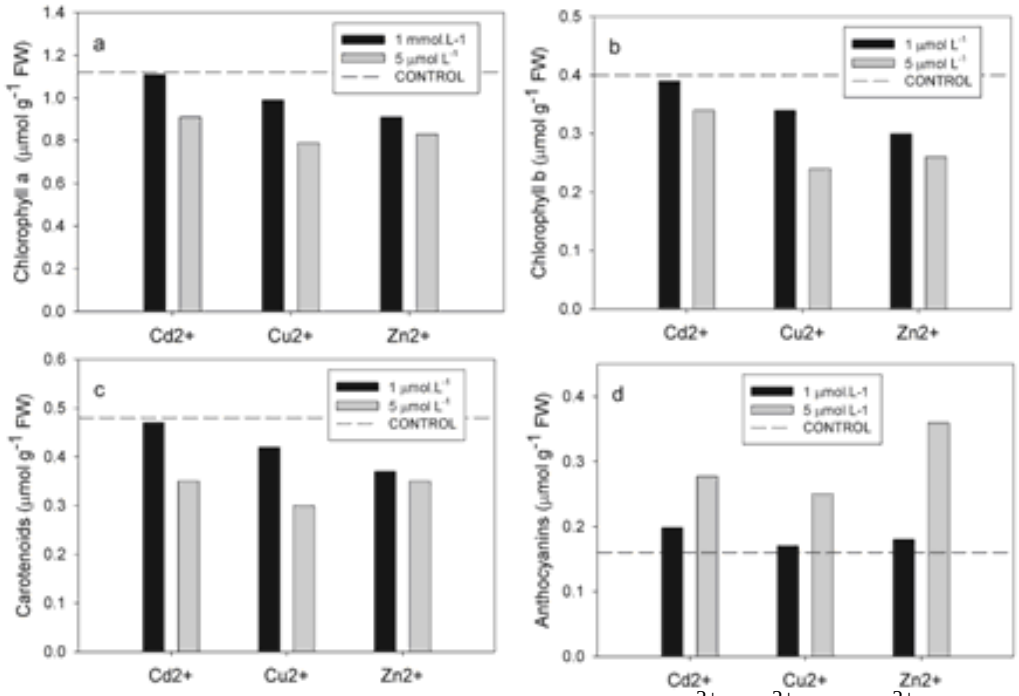

Figure 4. Leaf pigments in wheat plants exposed to Cd^{2+}, Cu^{2+} and Zn^{2+}: a – chlorophyll *a*, b – chlorophyll *b*, c – carotenoids, and d – antocyanins. Vertical bars are averages of three measurements; standard deviations did not exceed 10%.

The abovementioned index is often used to assess whether photosystem I or photosystem II was affected (or not) by different stresses to which plants are exposed [20]. Our results indicated that higher concentrations of Cu^{2+} and Zn^{2+} could induce modulations of the light-harvesting antennae of photosystem II where Chl *b* is mainly located, serving adaptive purposes.

Also, the values of Car: Chl ratios were quite similar, irrespective of whether plants were subjected or not to heavy metals excess (Table 2). Their variation didn't exceed 10% from control, except for a slight decrease observed at 5 µmol L^{-1} Cd^{2+}. These data suggested that wheat plants weren't exposed to high stress during the experiment, as increased carotenogenesis that may develop as a consequence of various stresses [21] wasn't noticed.

Table 2. Chl *a*: Chl *b* and Car: Chl ratios for wheat plants exposed to Cd^{2+}, Cu^{2+} and Zn^{2+}

Me^{2+}/ μmol L^{-1}	*Chl a: Chl b*				*Car: Chl*			
	control	Cd	Cu	Zn	control	Cd	Cu	Zn
1	2.8	2.85	2.91	3.03	0.32	0.31	0.32	0.31
5	2.8	2.68	3.29	3.19	0.32	0.28	0.29	0.32

Anthocyanins concentration in untreated wheat plants was of 0.16 μmol g^{-1} FW. At 1 μmol L^{-1} heavy metal excess, anthocyanin content significantly increased only in Cd^{2+} exposed plants, being 24% greater than in control plants. Anthocyanin content of wheat leaves markedly increased at 5 μmol L^{-1} of all the tested heavy metals. Thus, compared to control, the measured anthocyanin concentrations were of 125%, 75% and 56% in leaves of the plants exposed to Zn, Cd and Cu, respectively (Fig. 4, d). In photosynthetic tissues, anthocyanin's role is to screen damaging radiation and protect against photodeterioration by excess light. Anthocyanins may also provide protection against heavy metal-induced oxidative stress by acting as free radical scavengers, although such a role is controversial, as these water soluble pigments are located in vacuoles, separated from the sites of reactive oxygen species (ROS) generation [22].

4. CONCLUSIONS

As long as growth inhibition was concerned, it was obvious that the tested heavy metals interfered with the normal physiology of wheat plants, leading to dose-dependent alterations of growth rate. At low exogenous concentrations of the tested heavy metals (*i.e.* 1 μmol L^{-1} and 5 μmol L^{-1}), where no significant growth inhibition occurred, certain biochemical parameters registered variations that might be indicators for the activation of defense responses.

Among these, the dose-dependent decrease in chlorophylls and carotenoids content was a general response of wheat plants in our experiments. Increased peroxidase activity and glucose content were observed especially in wheat plants exposed to Cd^{2+} and Cu^{2+}, while protein content was almost the same in all probes. Zn^{2+} exposure may be associated with a slight increase in lipid peroxidation but also with higher levels of leaf anthocyanins. These data are suggestive for the onset of defense responses to heavy metal excess in wheat plants, and appear rather unspecific at low concentrations of the metals.

However, adaptive responses to cope with stress effects are resource consuming and may deplete plants reserves, leading to growth inhibition. Thus, the relevance of heavy metal toxic effects on plant physiology increases when

they are followed on longer duration, when either adaptation to the given conditions or accelerated decline may occur.

References

1. G. U. Chibuike, S. C. Obiora, *Appl. Environ. Soil Sci*., (**2014**) doi:10.1155/2014/752708.
2. R. A. Festa, D. J. Thiele, *Curr. Biol*., 21 (**2011**) R877.
3. I. Iakovidis, I. Delimaris, S. M. Piperakis, *Mol. Biol. Int.*, (**2011**) doi:10.4061/2011/594529.
4. I. Yruela, *Funct. Plant Biol.* 36 (**2009**) 409.
5. M. R. Broadley, P. J. White, J. P. Hammond, I. Zelko and A. Lux, *New Phytol*., 173 (**2007**) 677.
6. Wolfgang Maret. *Adv. Nutr*., 4 (**2013**) 82.
7. J. Osredkar, N. Susta,. *J. Clinic. Toxicol*., S:3 (**2011**) doi:10.4172/2161-0495.S3-001.
8. P. Joseph , T*oxicol. Appl. Pharmacol*., 238 (**2009**) 272.
9. M. Filipic, *Mutat. Res*., 733 (**2012**) 69.
10. J. Chmielowska-Bak, K. Izbianska, J. Deckert, *Acta Biochim. Pol*., 60 (**2013**) 369.
11. I. Ali, P. Damdimopoulou, U. Stenius, A. Adamsson, S. I. Mäkelä, A. Åkesson, M. Berglund, H. Håkansson, K. Halldin, *Toxicol. Sci*., 127 (**2012**) 66.
12. V. Page, U. Feller, *Ann. Bot-London*, 96 (**2005**) 425.
13. M. M. Bradford, *Anal. Biochem.*, 72 (**1976**) 248.
14. H. U. Bergmeyer, *Methods of Enzymatic Analysis 1*, Academic Press, New York (**1974**).
15. H. H. Draper, M Hadley, *Methods Enzymol.*, 186 (**1990**) 421.
16. H. K. Lichtenthaler, *Methods Enzymol.*, 148 (**1987**) 350.
17. T. Tsonev and F. J. C. Lidon, *Emir. J. Food Agric*., 24 (**2012**) 322.
18. R. E. Wrolstad, R. W. Durst, J. Lee, *Trends Food Sci. Tech*., 16 (**2005**) 423.
19. C. Cobbett, P.Goldsbrough, *Annu. Rev. Plant Biol*., 53 (**2002**) 159.
20. R. Tanaka and A. Tanaka, *Biochim. Biophys Acta*, 1807 (**2011**) 968.
21. A. Gitelson, Y. Zur, O. B. Chivkunova, M. N. Merzlyak, *Photochem. Photobiol.*, 75 (**2002**) 272.
22. K. Goluld, J. McKelvie, K. Markham, *Plant Cell Environ*. 25 (**2002**) 1261.

Annals of the University of Craiova
The Chemistry Series
Volume XLIV, No. 1 (2017) 47-53
homepage: chimie.ucv.ro/anale/

The corrosion control of metal materials using environmental-friendly inhibitors

An Overview

Ana-Cristina Vladu[1,2]

[1]University of Craiova, Faculty of Sciences, Department of Chemistry, Calea Bucuresti, 107i, Craiova, Romania
[2]Babes-Bolyai University, Faculty of Chemistry and Chemical Engineering, Arany Janos Street, no. 11, Cluj-Napoca, Romania
*e-mail: vladu.anacristina@gmail.com

Received: 20.02.2017 / *Accepted*: 15.03.2017 / *Published*: 10.05.2017

Abstract
The mettalic materials are generally characterized by intrinsic thermodynamic instability, and spontaneously changing their overall charge density by electron donation. Therefore, they inevitably degrade over time, the process having technical, economical and environmental implications. Corrosion preventions is an extremely important goal, since it is more practical technically and economically, also having a beggier achievement potential that the complete removal of affected parts and tools.

Keywords: corrosion; eco-friendly inhibitors; testing methods; action mechanism

1. INTRODUCTION

In the well defined by the need to preserve the environment context, the efforts of the scientific community involved in the field of corrosion protection conjugated to identify highly effective organic inhibitors with environmentally friendly properties [1-32]. In addition, theoretical methods of study based on quantum chemistry formalism and computational calculation resources with

remarkable results were added to the instrumental method of corrosion inhibitors testing [16, 18, 25]. Currently, the quantum-based correalations between chemical reactivity and corrosion protection performance are established in the literature of the field.

2. THE CURRENT STATE OF KNOWLEDGE IN THE FIELD

2.1. Processing of the literatura data

Many articles published in the field, especially from the last years were studied. The data selected [1-32] was centralized and processed in order to carry out a comparative analysis of inhibition efficiencies reported for certain organic compounds from the class of drugs, azo compounds and amino acids.

Thus, Table 1 presents the corrosion inhibitors tested, the corrosive environments and alloys on which they act as direct surface protectors or as substances that clearly influence the passive films that are developed on the metal surface.

DRUGS		
Name	Studied metal/alloy	Corrosive media
Cefoperazone [1]	carbon steel [1]	HCl 0,5 mol L^{-1}
Cefazolin [2, 3]	carbon steel [2, 3]	H_2SO_4 0,5 mol L^{-1} [2] HCl 1,0 mol L^{-1} [3]
Cefotaxime [2, 4]	carbon steel [2]	H_2SO_4 0,5 mol L^{-1} [2]
Phenytoin [5, 6]	mild steel [4]	HCl 1,0 mol L^{-1} [4]
	carbon steel [5, 6]	H_2SO_4 1,0 mol L^{-1} [5] HCl 1,0 mol L^{-1}[6]
Penicilin G [7]	carbon steel [7]	HCl 1,0 mol L^{-1}
Ampicilin [7]	carbon steel [7]	HCl 1,0 mol L^{-1}
Amoxicilin [7]	carbon steel [7]	HCl 1,0 mol L^{-1}
Meclizine [8]	aluminium [8]	HCl 1,0 mol L^{-1}
Esomeprazole [9]	mild steel [9]	HCl 0,5 mol L^{-1}
Doxycycline [10]	mild steel [10]	HCl 1,0 mol L^{-1}
Cefalexin [11]	mild steel [11]	HCl 1,0 mol L^{-1}
Gatifloxacin [12]	mild steel [12]	HCl 1,0 mol L^{-1}
Carbamazepine [13]	mild steel [13]	H_2SO_4 0,1 mol L^{-1}
Paracetamol [13]	mild steel [13]	CH_3COOH/CH_3COONa
Sulfathiazole [14-16]	mild steel [14, 15]	HCl 1,0 mol L^{-1} [14, 15]
	theoretical studies [16]	theoretical studies [16]
Sulfacetamide [16-18]	carbon steel [17, 18]	HCl 1,0 mol L^{-1} [17, 18]
	theoretical studies [16, 18]	theoretical studies [16, 18]
Quinine [19, 20]	carbon steel [19, 20]	HCl 1,0 mol L^{-1} [20] HCl 1,5 mol L^{-1} [19]
Trimethoprim [21]	carbon steel [21]	HCl 1,0 mol L^{-1}
Aminophylline [22]	carbon steel [22]	HCl 1,0 mol L^{-1}

Systematization of the literature data according to Gece [23]

The corrosion inhibitors in the class of β-lactam antibiotics

The corrosion inhibitors in the class of quinolones

The corrosion inhibitors in the class of tetracyclines
The corrosion inhibitors in the class of macrolides
The corrosion inhibitors in the class of lincosamides
The corrosion inhibitors in the class of sulphonamides
The corrosion inhibitors in the class of aminoglycosides
The corrosion inhibitors in the class of amphenicols
The corrosion inhibitors in the class of antifungal drugs
The corrosion inhibitors in the class of anthelmintics
The corrosion inhibitors in the class of muscle relaxants
The corrosion inhibitors in the class of antiviral drugs
The corrosion inhibitors in the class of opioid analgesics
The corrosion inhibitors in the class of histamines
The corrosion inhibitors in the class of antipsychotic drugs
The corrosion inhibitors in the class of antihypertensive drugs
The corrosion inhibitors in the class of ameobicidal drugs

AZO COMPOUNDS WITH ANTIMICROBIAL PROPERTIES		
Azo compounds of tiophenes [24]	carbon steel [24]	HCl 2,0 mol L^{-1}
Azoesthers: 4-(phenyldiazenyl)phenyl 2-furoate [25, 26]	carbon steel [25, 26]	0,15 mol L^{-1} NaCl/0,001 mol L^{-1} HCl [25, 26]
	theoretical studies [25]	theoretical studies [26]
Azoether: 4-[(4-chlorobenzyl)oxy]-4'-chloro-3,5-dimethyl-azobenzene [27]	carbon steel [27]	0,15 mol L^{-1} NaCl/ water-dioxane (1:1 - volume)
AMINO ACIDS		
3,5-diiodotyrosine[28]	iron [28]	HCl 1,0 mol L^{-1} [29]
Tryptophan [28, 29]	carbon steel [29]	CH_3COOH/CH_3COONa [29]
Glycin [30] Valine [30] Leucine [30]	316 L stainless steel [30]	H_2SO_4 0,1 mol L^{-1}
Sulfur amoni acids [31]	mild steel [31]	H_2SO_4 0,1 mol L^{-1}
Histidine [32]	carbon steel [32]	CH_3COOH/CH_3COONa

2.2. Investigation methods for corrosion inhibitors

The electrochemical methods are short-time investigation methods, which allow a quick evaluation of metal behaviour in different media, at different temperatures, in static or dynamic conditions. The most used are: potentiodynamic polarization and electrochemical impedance spectroscopy (EIS).

Weight loss evaluation by gravimetric or voltametric methods led to the estimation of corrosion rate expressed as an gravimetric index (g/m^2h) or as an corrosion index (mm/an).

This methods were associated with different comparative analysis techniques of the metal surface in the presence and absence of inhibitors, such as:

- X-ray photoelectronic spectroscopy (XPS);
- scanning electron microscopy (SEM);
- scanning electron microscopy coupled with energy-dispersive X-ray spectroscopy (SEM/EDS);
- thermal analysis (TG/DSC/DTA).

2.3. Inhibition efficiency

The studies made highlighted a pozitive correlation between de inhibition efficiency and the hydrocarbon chain lenght, that when increased it has a negative effect on the solubility in aqueous solution. The presence in the molecule of the hydrophilic functional groups has the effect of increasing the solubility of the inhibitor in the aqueous solution

The efficiency of corrosion inhibition is dependent on the nature of the organic compounds by means of geometry, size and electronic properties of such molecules, the concentration thereof in a corrosive solution, the nature of the metal surface and its load, the electrochemical potential at the interface, the nature of the corrosive environment.

Whatever the action mechanism of the inhibitor, its corrosion inhibition efficiency represents the slowing of corrosion or more, the decrease of the corrosion current (or the rate of corrosion). The inhibition efficiency of an inhibitor is expressed by the following equations: 1-3.

$$\%\, EI = \frac{i^{o}_{cor} - i_{cor}}{i^{o}_{cor}} \times 100 \qquad (1)$$

$$\%\, EI = \frac{R_{ct} - R^{o}_{ct}}{R_{ct}} \times 100 \qquad (2)$$

$$\%EI = \left(1 - \frac{CR}{CR^{o}}\right) \times 100 \qquad (3)$$

where:

- i_{corr}^{o} and i_{corr} represent the corrozion currents, in the absence and presence of the inhibitor;
- R_{ct}^{o} and R_{ct} represent the charge-transfer resistance, in the absence and presence of the inhibitor;
- CR^{o} and CR represent de corrosion rate, in the absence and presence of the inhibitor.

The inhibition efficiency of the drugs is shown in Fig. 1. It is noted that they have a significant protective capacity, most of them reaching an efficiency

greater than 90%, except paracetamol, sulfacetamide, trimethoprim and aminophylline.

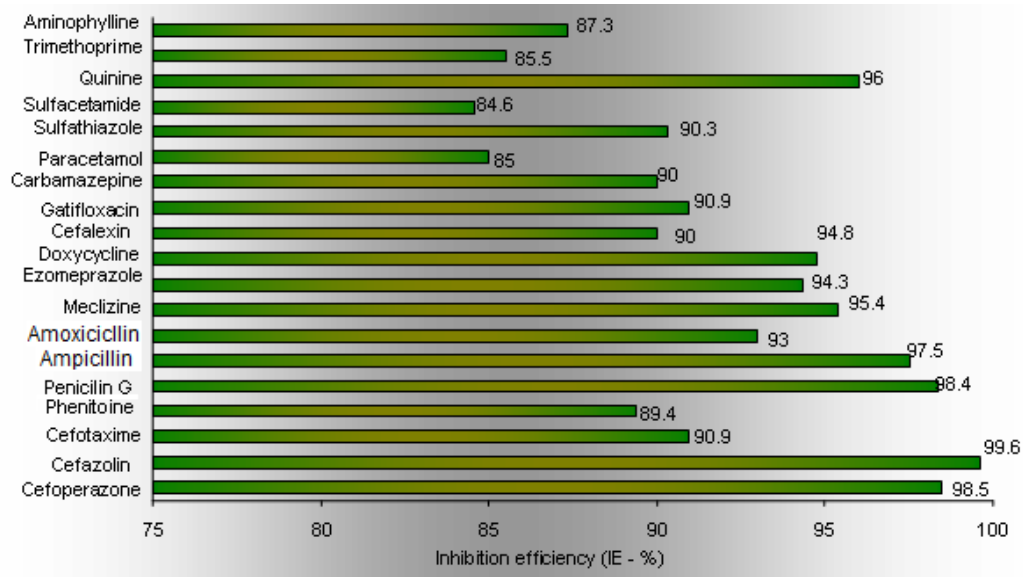

Figure 1. The efficiency of inhibition as evaluated by weight loss measurements and electrochemical techniques on the corrosion of metal substrates in various environments reported in literature studies [1-23]

A lower level of protective capacity was reported for azo compounds but bring significant contributions to the formation of stable and adherent surface films (Fig. 2).

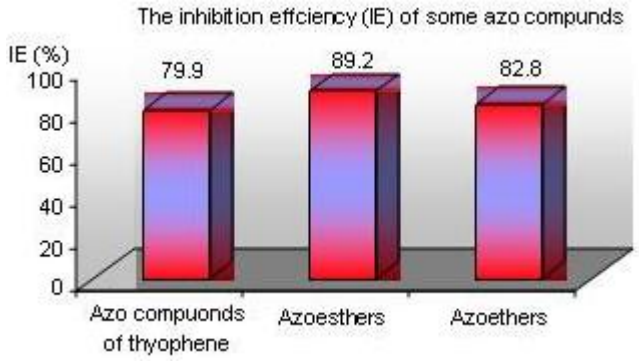

Figure 2. The inhibition efficiency of some azo compounds as evaluated by weight loss measurements and electrochemical techniques on the corrosion of carbon steel in various environments reported in literature studies [23-27]

The amino acids were substances of interest as corrosion inhibitors, the inhibitory efficiencies determined, however, have not always achieved the expected value. As shown in Fig. 3, valine and leucine have a low efficiency below 40%.

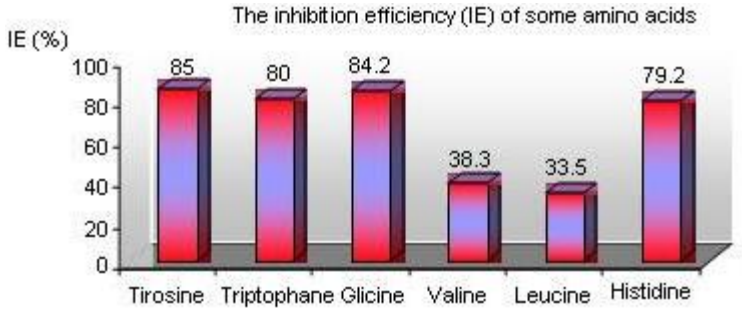

Figure 3. The inhibition efficiency of some amino acids as evaluated by electrochemical measurements on the corrosion of carbon steel and stainless steel, in various environments reported in literature studies [28-32]

2.4. The action mechanism

The results of studies that aim organic inhibitors [1-32] converge to the idea that most of them are adsorbed on the metal surface by replacing the water molecules and form a compact physical barrier that isolates the metal surface from the corrosive solution.

These organic inhibitors are concentrated in the surface layer of the metal/solution interface by noncovalent interactions (physisorption) and/or covalent bonds (chemisorption), forming thin films ont the metal surface with a thickness of the order of a few molecular diameters or monolayers. These molecule polilayers or molecular monolayers generate protection by blocking the annodic dissolution of the metal in the electrolyte solution: either by a geometrical blocking effect - the electrochemical reaction available surface area is reduces, or as a result of an energetic effect - the inhibitor layer increases the activation energy of the corresponding cathodic and/or anodic reaction.

The physical adsorbtion preserves the identity of the inhibitor's molecules and their preferential accumulation at the metal/corrosive solution interface through atractive electrostatic interactions ion-ion or ion-dipole.The electrical charges on the metal surface are the result of the existing electric field at the metal/electrolyte solution interface.

The chemical adsorbtion involves a reorganization of the inhibitor's molecular orbitals and electron density changes in the vicinity of points on the metal surface involved in chemical liasing. The process flows irreversibly with a slower rate due to the bigger demand of energy for overcoming the potential

barrier energy involved by the electron transfer between inhibitor and metal.

Chemisorption involves sharing the electric charge between polar molecules and metal surface or transfering of electrons from the organic compound to the metal surface by donor-acceptor covalent type interactions. These involve the ***π*** and/or ***n*** donor type orbitals and the vacant ***d*** orbitals of the elements from the alloy.

4. CONCLUSIONS

The efficiency of inhibition is strictly dependent on the molecular configuration of the inhibitor, the nature and pH of the media, the substrate on which the investigation is carried out, as well as temperature and mode of operation: static or dynamic.

In Fig. 4 is shown the maximum inhibition efficiency obtained for drugs, azo compounds and amino acids reported in the studied articles.

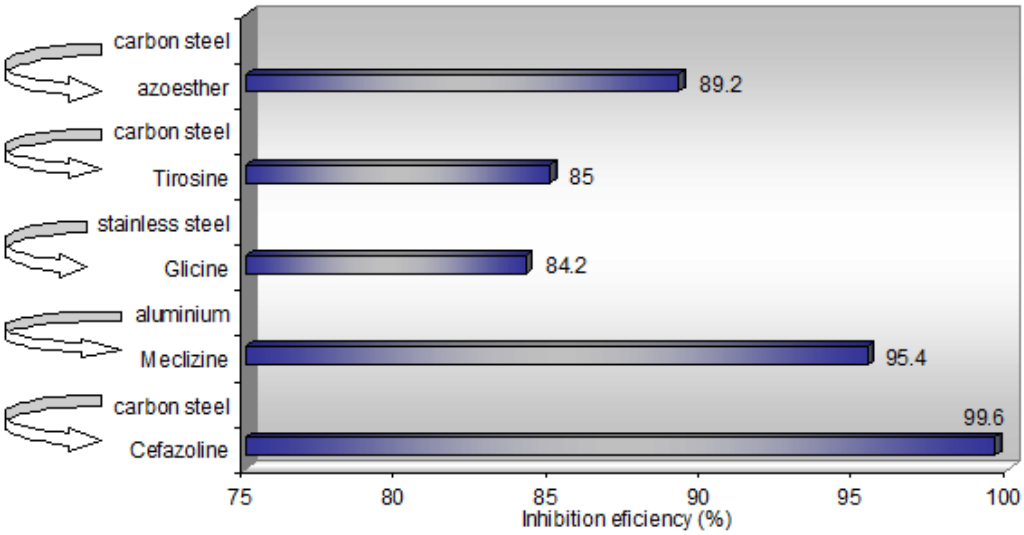

Figure 4. The highest level of the inhibition efficiency of the studied compounds on the corrosion of some substrates in acidic media, reported in the literature

References

1. A. Nazeer, H.M. El-Abbasy, A.S. Fouda, *J. Mater. Eng. Perform.*, 22 (**2013**) 2314.
2. A. A. Nazeer, H. M. El-Abbasy, A. S. Fouda, *Res. Chem. Intermed.*, 39 (**2013**) 921.

3. A. K. Singh, M. A. Quraishi, *Corros. Sci*., 52 (**2010**) 152.
4. S. K. Shukla, M. A. Quraishi, *Corros. Sci*., 51 (**2009**) 1007.
5. U. M. Eduok, M. Khaled, *Res. Chem. Intermed*., (**2014**) doi: 10.1007/s11164-014-1741-3.
6. H. I. Al-Shafey, R. S. Abdel Hameed, F. A. Ali, Abd el-Aleem S. Aboul-Magd, M. Salah, *Int. J. Pharm. Sci. Rev. Res*., 27 (**2014**) 146.
7. Gh. Golestani, M. Shahidi, D. Ghazanfari, *Appl. Surf. Sci*., 308 (**2014**) 347.
8. J. Ishwara Bhat, Vijaya D. P. Alva, *Trans. Indian Inst. Met*., 64 (**2011**) 377.
9. G. Karthik, M. Sundaravadivelu, P. Rajkumar, *Res. Chem. Intermed*., 41 (**2015**) 1543.
10. S. K. Shukla, M. A. Quraishi, *Corros. Sci*., 52 (**2010**) 314.
11. S. K. Shukla, M. A. Quraishi, *Mater. Chem. Phys*., 120 (**2010**) 142.
12. M. Sobhi, *Protect. Met. Phys. Chem. Surf*., 50 (**2014**) 825.
13. Nic. Vaszilcsin, V. Ordodi, A, Borza, *Int. J. Pharm*., 431 (**2012**) 241.
14. A. Samide, B. Tutunaru, *Chem. Biochem. Eng. Q*., 25 (**2011**) 299.
15. A. Samide, B. Tutunaru, C. Negrilă, I. Prunaru, *Spectr. Lett*., 45 (**2012**) 55.
16. E. E. Ebenso, T. Arslan, F. Kandemirli, I. Love, C. Ödretır, M. Saracoğlu, S. A. Umoren, *Int. J. Quantum Chem*., 110 (**2010**) 2614.
17. A. Samide, B. Tutunaru, C. Negrilă, I. Trandafir, A. Maxut, *Digest J. Nanomater. Biostruct*., 6 (**2011**) 663.
18. A. Samide, B. Tutunaru, C. Negrilă, A. Dobriţescu, *J. Therm. Anal. Calorim*., 110 (**2012**) 145.
19. A. Samide, B. Tutunaru, *Cent. Eur. J. Chem*., 12 (**2014**) 901.
20. M. I. Awad, *J. Appl. Electroche*., 36 (**2006**) 1163.
21. A. Samide, *J. Env. Sci. Heal., Part A*, 48 (**2013**) 159.
22. A. Samide, B. Tutunaru, C. Ionescu, P. Rotaru, L. Simoiu, *J. Therm. Anal. Calorim*., 118 (**2014**) 631.
23. Gokhan Gece, *Corros. Sci*., 53 (**2011**) 3873.
24. M. N. El-Haddad, A.S. Fouda, H.A. Mostafa, *J. Mater. Eng. Perform*., 22 (**2013**) 2277.
25. A. Moanţă, B. Tutunaru, P. Rotaru, *J. Therm. Anal. Calorim*., 111 (**2013**) 1273.
26. A. Moanţă, A. Samide, C. Ionescu, B. Tutunaru, A. Dobriţescu, *Int. J. Electrochem. Sci*., 8 (**2013**) 780.
27. A. Samide, B. Tutunaru, A. Moanţă, C. Ionescu, C. Tigae, A. C. Vladu, *Int. J. Electrochem. Sci*., 8 (**2015**) 4637.
28. V. Hluchan, B. L. Wheeler, N. Hackerman, *Mater. Corros*., 39 (**1988**) 512.
29. M. Bobina, N. Vaszilcsin, C. Muntean, *Rev. Chim*., 64 (**2013**) 83.
30. N.A. Abdel Ghanyl, *Mod. Appl. Sci*., 5 (**2011**) 19.
31. M. A. Abdel Rahim, Hanaa B. Hassan, M. W. Khalil, *Mater. Sci. Eng. Techn*., 28 (**1997**) 98.
32. M. Bobina, A. Kellenberger, J.-P. Millet, C. Muntean, N. Vaszilcsin, *Corros. Sci*., 69 (**2013**) 389.

Annals of the University of Craiova
The Chemistry Series
Volume XLIV, No. 1 (2017) 54-64
homepage: chimie.ucv.ro/anale/

Novel composite C_3N_4/CuO on layered double hydroxide matrix with enhanced oxidative catalytic activity

Research article

Geanina Maria Iovan (Cioana)[1,*], *Mihaela Mureșeanu*[1,*], *Mihaela Darie*[2]

[1] University of Craiova, Faculty of Sciences, Department of Chemistry, Calea Bucuresti, 107i, Craiova, Romania
[2]Faculty of Chemical Engineering and Environmental Protection, Technical University of Iasi, 71 D. Mangeron, Iasi, Romania
[*]e-mail: cioarnamariageanina@yahoo.com; mihaela_mure@yahoo.com

Received: 23.01.2017 / *Accepted*: 15.03.2017 / *Published*: 10.05.2017

Abstract
The present study reports the design of new composite catalysts based on layered graphitic carbon nitride (g-C_3N_4) and CuO nanoparticles on a lamellar double hydroxide matrix (ZnAlLDH) and the composite C_3N_4/mixed oxides obtained after LDH calcination. Firstly, a ZnAlLDH was synthesised by co-precipitation under low suprasaturation conditions of Zn and Al nitrated solutions with Na_2CO_3 and NaOH, at constant pH. The solid was thermally decomposed at 550^0 C in air, in absence or in presence of melamine, in order to obtain mixed oxides or composite g-C_3N_4/mixed oxides. These samples were used thereafter for the reconstruction of the hydrotalcite structure from a $Cu(OAc)_2$ solution, by means of memory effect and the simultaneous self-assembly of the CuO nanoparticles on the LDH matrix. The composite material crystalline phase, surface morphology and structural, optical and thermal properties were investigated by various physico-chemical techniques. The catalytic activity was succefuly tested in the cyclohexene oxidation by H_2O_2.

Keywords: layered double hydroxides; composite catalyst; g-C_3N_4, CuO nanoparticles; cyclohexene oxidation

1. INTRODUCTION

The development of environmental friendly technologies has promoted sustained research for obtaining novel efficient heterogeneous catalysts. The selective oxidation of hydrocarbons to oxygen-containing compounds is of great interest both in industry and in academic research [1, 2]. In particular, allylic oxidation of olefins into unsaturated ketones and alcohols is important in organic chemistry and chemical industry [3]. For example, the oxidation products of cyclohexene and their derivatives, viz. 2-cyclohexen-1-one, 1-methylcyclohex-1-en-3-one, etc., are utilized in cycloaddition reactions owing to the presence of a highly reactive carbonyl group [4].

The lamellar double hydroxides (LDH)-based catalysis is of high interest for green and sustainable chemistry [5] since the LDHs are able to provide distinct nanometer scaled layers and interlayers for engineering them as active catalysts [6]. Furthermore, the catalytic efficiency of the oxidation processes could be tailored by controlling the nature of the metal cations from the LDHs layers, but also the composition of the catalysts in such a way to control the microenvironment of the active sites. In order to tailor a more efficient catalyst for cyclohexene oxidation, new composite based on layered graphitic carbon nitride (g-C_3N_4) and a lamellar double hydroxide (ZnAlLDH) reconstructed from a $Cu(OAc)_2$ solution by means of memory effect were designed. These materials were successfully obtained for the first time and are shown to be efficient catalysts for the process of cyclohexene oxidation by H_2O_2.

2. MATERIALS AND METHODS

2.1. Materials

All chemicals were commercially purchased and used without further purification. Melamine (Aldrich, 99%), $Al(NO_3)_3 \cdot 9H_2O$, $Zn(NO_3)_2 \cdot 6H_2O$, $Cu(OAc)_2 \cdot H_2O$, Na_2CO_3, NaOH (Aldrich, 99.9%), were used for the LDH precursor and the composite catalyst synthesis.

2.2. Synthesis procedure of materials

The synthesis of ZnAlLDH was carried out following a simple coprecipitation method with the Zn/Al atomic ratio of 2.0 as previously described [7]. CuO supported on ZnAlLDH was obtained exploring the structural reconstruction of LDH in the aqueous solution of $Cu(OAc)_2$ [8]. Namely, 1.20 g ZnAlLDH was calcined in an oven at 500^{o}C for 10 h. The resulted calcined powder was cooled down in an oven till 200^{o}C and added,

under very vigorous stirring into 250 mL of an 0.1 M aqueous solution of Cu^{2+} acetate. The obtained sample was aged at room temperature for 1 h, washed, centrifuged, dried under vacuum and denoted as ZnAlLDH/CuONP. The composite ZnAlLDH/melamine was prepared as follows: 0.2 g melamine was added into a mixture of 30 mL methanol and 80 mL H_2O and dispersed for 30 min. in an ultrasonic bath. Thereafter, 1.2 g of freshly calcined ZnAlLDH (at 500^0C for 10 h) was added when still hot (200^oC) and the mixture was vigorously stirred at 65^oC for 1 h, then at room temperature for another 2 h. The solid sample was obtained after filtration and vacuum dried. For ZnAlLDH/g-C_3N_4/CuONP synthesis, ZnAlLDH/melamine was firstly calcined at 450^oC for 6 h in order to transform melamine in g-C_3N_4 and LDH in the corresponding mixed oxides (sample denoted ZnAlMMO/g-C_3N_4) and added thereafter when still hot in a $Cu(OAc)_2$ aqueous solution. The sample was denoted ZnAlLDH/g-C_3N_4/CuONP. For comparison, g-C_3N_4 was prepared by heating melamine at 500^oC for 2 h under N_2 atmosphere according to the literature [9].

2.3. Material characterization

The X-ray powder diffraction (XRD) patterns were obtained on a Bruker AXS D8 diffractometer by using Cu Kα radiation and Ni filter. Fourier tranform infrared (FTIR) spectra were recorded using a Bruker Alpha spectrometer in KBr matrix in the spectral range of 4000–400 cm^{-1}, at a resolution of 4 cm^{-1}. The copper content was determined by flame atomic absorption spectrometry (AAS) on a Spectra AA-220 Varian Spectrometer with an air-acetylene flame.

Thermogravimetric analysis (TG/DTG) was carried out in a Netzsch TG 209C thermobalance, heating rate of 10^0C/min, in nitrogen flow.

XPS measurements were performed with a SPECS PHOIBOS 150 MCD instrument, equipped with monochromatized Al Kα radiation (1486.69 eV) at 14 kV and 20 mA, and a pressure lower than 10^{-9} mbar. The binding energy scale was referenced to the C 1s photoelectron peak at 285eV. A low energy electron flood gun was used for all measurements to minimize sample charging. The elemental composition on the outermost layer of samples (about 5 nm deep from surface) was estimated from the areas of the characteristic photoelectron lines in the survey spectra assuming a Shirley type background. High-resolution spectra were recorded in steps of 0.05 eV using the analyser pass energy of 30 eV. The spectra deconvolution was accomplished with Casa XPS (Casa Software Ltd., UK).

2.4. Catalytic tests

The oxidation of cyclohexene (CH) was carried out in the liquid phase over ZnAlLDH/g-C_3N_4/CuONP, under air, using H_2O_2 as oxidant. The typical

catalytic oxidation of CH was carried out as follows: 2.26 mmoles of CH, 0.03 mmoles of catalyst and 10 mL of acetonitrile were added successively at a controlled temperature in a two-necked round-bottom flask with a reflux condenser. The corresponding amount of hydrogen peroxide (30% H_2O_2) was then added drop wise. The reaction was performed at 60^oC during different time intervals. After the reaction took place for the established time period, the reaction mixture was cooled, the products were filtered to separate them from the catalyst and they were analyzed using a Thermo DSQ II system with gas chromatograph GC-Focus and mass spectrometer DSQ II. A Thermo TR-5MS capillary column, 30 m x 0.25 ID x 0,25 μm film was used for the analysis of separated compounds present in the samples. H_2O_2 consumption was determined by an iodometric titration after the reactions. The H_2O_2 efficiency was calculated as the percentage of this reactive converted to oxidized products.

The persistence of the catalytic activity was checked for 5 consecutive runs in the oxidation of cyclohexene.

3. RESULTS AND DISCUSSION

3.1. Catalyst characterization

The powder X-ray diffraction patterns of LDH-like clays were illustrated in Fig. 1. The XRD pattern of ZnAlLDH revealed the presence of a single crystalline phase with a series of sharp and symmetrical basal reflections of the 003, 006 and 009 planes, assigned to the regular layered structure of $Zn_{0.7}Al_{0.3}(OH)_2(CO_3)_{0.15}H_2O$ (PDF 48-1022). The interlayer space was 0.76 nm, on the basis of the (003) diffraction angle of $2\theta=11.6^o$.

ZnAlLDH/CuONP showed the main LDHs reflections becoming broader and shifted to lower 2θ values (i.e. (003) reflection was shifted from 11.6^o for ZnAlLDH to 7.1^o for ZnAlLDH/CuONP), indicating that the LDH reconstruction in $Cu(OAc)_2$ solution gave rise to an expanded LDH structure with the acetate anions intercalated into the interlayers and the interlayer space of 12.9 Å. This value was in good agreement with that previously reported for materials of the same type [8]. There were not significant differences between the two reconstructed LDH-type samples from a copper acetate solution, in presence and in absence of g-C_3N_4. The increase of the *c* parameter for these reconstructed samples was related to the expansion of the interlayer region after acetate anions intercalation.

Another phase, such as ZnO (Zincite, PDF:89-7102) indicated an incomplete incorporation of zinc to the brucite-like sheets of the reconstructed LDH and the formation of ZnO nanocrystals. This was because Zn^{2+} underwent a partly hydrolysis at high pH to precipitate ZnO in alkaline conditions, so the

reconstructed materials were a composite of ZnO and ZnAlLDH. On the other hand, characteristic diffraction reflections neither of CuO nor of g-C_3N_4 were noticed in the XRD patterns of ZnAlLDH/CuONP and ZnAlLDH/g-C_3N_4/CuONP, probably because of the lower loading, the low crystallinity and/or the good dispersion of the CuO nanoparticles on the clay surface.

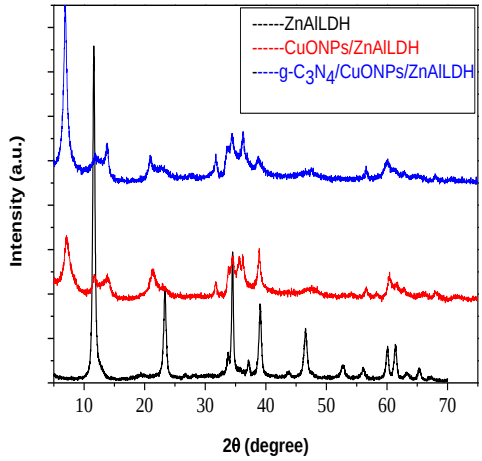

Figure 1. X-ray diffraction pattern of LDH-type samples

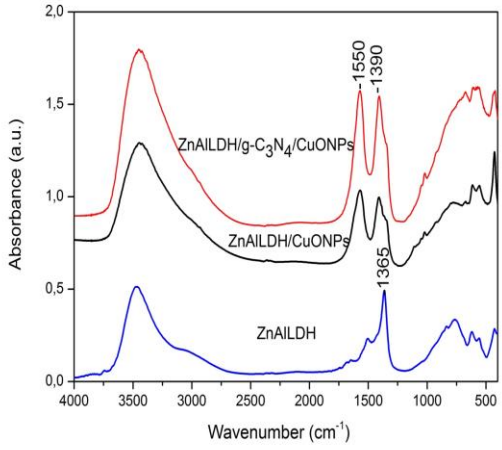

Figure 2. Comparison of the FTIR spectra of LDH-type samples

The FTIR spectra of the as-synthesised ZnAlLDH and the two reconstructed LDH-type photocatalysts from $Cu(OAc)_2$ solution were presented in Fig.2. For all samples, the strong bands around 3600-3200 cm^{-1} were associated to the ν_{OH} mode of the H-bonded hydroxyl groups, both from the brucite-like layers and from interlayer water molecules. The spectrum of pure

LDH showed a band at 1365 cm^{-1} that was attributed to antisymmetric ν_3 mode of interlayer carbonate anions. In the same range, the ν_3 vibration mode of the nitrate anion could have appeared, if this anion had still been present in the brucite interlayer [10].

The FTIR spectra of ZnAlLDH/CuONP and ZnAlLDH/g-C_3N_4/CuONP samples revealed that the absorption band at 1550 cm^{-1} and 1390 cm^{-1} originated from the antisymmetric and symmetric COO^- stretching vibration mode. This indicated the presence of CH_3-COO^- as interlayer anion, after the clay reconstruction in copper acetate solution. The difference between antisymmetric and symmetric COO^- stretching vibration bands was 160 cm^{-1}. This large difference meant that COO^- was in monodentate state rather than free group state, being coordinated to the cations of the brucite layer. The bands at wavenumber lower than 850 cm^{-1} were due to the M-O and O-M-O vibrations of the hydrotalcite.

The characteristic bands of g-C_3N_4 could not be observed in the FTIR spectra of ZnAlLDH/g-C_3N_4/CuONP. They were either overlapping with the LDH peaks or the carbon nitride concentration was too low.

The thermal stability and phase transformation of the LDHs samples reconstructed from $Cu(OAc)_2$ solution were studied and the TG-DTG curves are presented in Fig. 3. For the ZnAlLDH/CuONP sample, the thermal decomposition proceeded in four steps, as previously reported for LDH materials [11]. The first two steps (30-170^{0}C, 9.8% mass loss) corresponded to the removal of physically adsorbed and intergallery water. The third step (170-230^{0}C, 7.0% mass loss) could be attributed to dehydroxilation of the brucite like sheets. The sharp mass loss observed in the 230-350^{0}C range (14.3% mass loss) was due to the partial loss of structural H_2O and interlayer anions. The mass loss in the 350-800^{0}C (1.6%) could be associated with the collapse of the layered structure and the formation of a stable mixed oxide phase. The presence of CuONP in the composite LDH/CuO did not substantially affect the thermal stability, but there was observed a slight shift of the temperature stability range towards lower values compared to pristine ZnAlLDH. ZnAlLDH/g-C_3N_4/CuONP presented a total mass loss of 29.4% with the same decomposition steps as for the reconstructed LDH sample without carbon nitride: mass losses of 7.7% (30-170^{0}C), 7.2% (170-230^{0}C), 12.7% (230-350^{0}C) and 1.8% (350-800^{0}C).

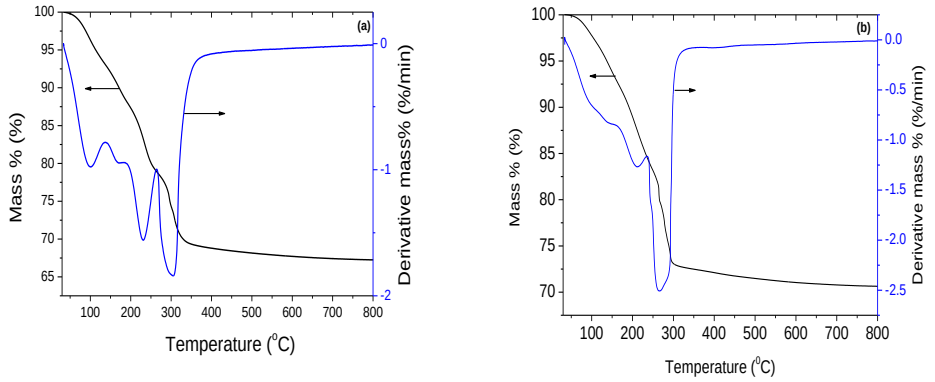

Figure 3. Thermal analysis of the ZnAlLDH/CuONP (a), ZnAlLDH/g-C_3N_4/CuONP (b)

The sample surface was investigated by XPS analysis to characterize the chemical state of Cu, Zn, Al, C, N and O with particular attention given to the Cu oxidation states.

The XPS survey spectra presented in Figs. 4 and 5 confirmed the presence of these elements in the ZnAlLDH/CuONP and ZnAlLDH/g-C_3N_4/CuONP samples. Furthermore, in these figures, the deconvoluted spectra for the present elements with their assignments were also shown.

The high resolution XPS spectrum of Cu2p in ZnAlLDH/CuONP presented a $Cu2p_{3/2}$ signal that could be deconvoluted into two peaks accompanied by a shake-up structure on the high binding energy side. The respective main peaks at 933.3eV and 935.6 eV were attributed to the Cu^{2+} species, which occupied octahedral and tetrahedral sites [12]. The appearance of satellite peak at 943.2 eV was a clear evidence of the Cu^{2+} state, which was probably present either as CuO or as $CuAl_2O_4$ spinel. Neither of these copper crystalline forms was identified in the XRD spectra, due to their low dimensions or good dispersion on the catalyst surface.

In the deconvoluted Cu2p spectra of this sample, a peak assigned to Cu^{+1} species was also present. We consider that it was an artefact of the XPS method. During acquisition time, X-ray irradiation of the XPS source caused a reduction in CuO film. Moreover, according to Chusuei et al. [13], XPS induced an increased reduction of Cu^{2+} to Cu^{+} in the presence of carbonaceous overlayer. This Cu^{+} extra-peak was not present in the Cu2p spectra of ZnAlLDH/g-C_3N_4/CuONP sample. Only the $Cu2p_{3/2}$ peaks, at 934.2 and 938.0 eV, for Cu^{2+} in octahedral and tetrahedral coordination, and the shake-up satellite at 943.3 eV were present (Fig. 5).

The presence of g-C_3N_4 that resulted from melamine calcination was evidenced in the N1s and C1s deconvoluted spectra and corresponded to the

reported data for the same type of materials [14]. Thus, in the N1s spectra, the peak at ca. 400 eV was usually attributed to N atoms bonded to two carbon atoms (C=N-C) (graphite like sp^2-bonded graphitic carbon nitride). The C1s spectrum could be deconvoluted in two peaks, at binding energies of 284.9 eV and 288.9 eV which were assigned to C-C bond and to carbon atom bonded to three nitrogen atoms in the g-C_3N_4 lattice, respectively.

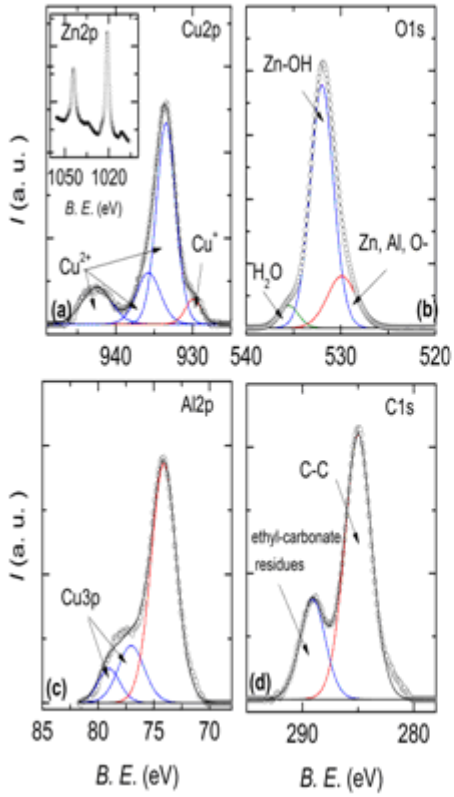

Figure 4. XPS images of ZnAlLDH/CuONP

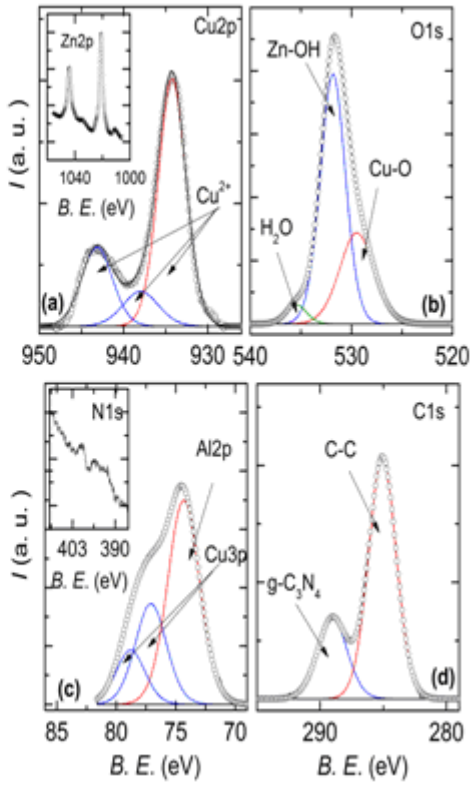

Figure 5. XPS images of ZnAlLDH/g-C_3N_4/CuONP

3.2. Catalytic oxidation of cyclohexene

The catalytic activity of the studied ZnAlLDH support and ZnAlLDH/CuONP and ZnAlLDH/g-C_3N_4/CuONP samples was tested for the oxidation of CH with H_2O_2 as oxygen source in acetonitrile as solvent, under air atmosphere.

Cyclohexene is a good model substrate for oxidation reactions since it contains both C=C and C-H bonds which could be attacked differently, depending on the used catalyst, the oxidant and the solvent, producing both allylic and epoxidation products. Acetonitrile was chosen as solvent as it allows higher

catalytic activity than other solvents, due to its high dielectric constant and the solubility of H_2O_2. Hydrogen peroxide is probably the second best terminal oxidant after dioxygen as regards environmental and economic considerations. Furthermore, the acetonitrile solvent, the H_2O_2 oxidant and the base sites of the LDH surface, joint effects which could be interesting from the catalytic point of view. The optimization of the CH oxidation was previously done [15]. The results of the catalytic tests are presented in Table 1.

Table 1 Catalytic performance of LDH type catalysts

Sample	CH conversion (%)	TOF (h^{-1})	Selectivity (%)		
			I	II	III
ZnAlLDH	40	18	16	36	48
ZnAlLDH/CuONP	78	105	48	20	32
ZnAlLDH/g-C_3N_4/CuONP	98	214	54	20	26

Reaction conditions: catalyst (50 mg), substrate (2.26 mmols), ACN (10 mL), H_2O_2 (4.75 mmols), 5h, 60^0C; Products formed: cyclohexene oxide (I), 2-cyclohexen-1-ol (II) and 2-cyclohexen-1-one (III); CH conversion (%) = [CH converted (moles) / CH used (moles)] x 100; Product selectivity (%) = [product formed (moles) / total product detected (moles)] x 100; TOF = Substrate converted (moles) / [Copper in catalyst (moles) x reaction time (h)]; t=20 min

The reaction did not proceed in the absence of the catalyst and the CH conversion on ZnAlLDH was moderate (40% of max.). For the ZnAlLDH/CuONP, the introduction of Cu ions in the brucite layers leads to an enhancement of the CH conversion up to 78%. The XRD and XPS analysis proved a good dispersion of Cu^{II} ions in the brucite layers either as isolated species or coordinated in spinels. It is clear that this Cu^{II} ions represent the active sites for the CH oxidation. Considering the great amount of copper in this sample (0.43 moles%), we can suppose that the copper ions act as an initiator of free radical oxidation ZnAlLDH/CuONP rather than as a catalyst if taking into account that the CH oxidation proceeds mainly via a free radical oxidation process.

The maximum CH conversion was 98% over ZnAlLDH/g-C_3N_4/CuONP (initial turnover frequency of 214 h^{-1}). The surface nature of the LDH support plays an important role in establishing catalyst selectivity. The main products obtained during CH oxidation are cylohexene oxide (I), 2-cyclohexen-1-ol (II) and 2-cyclohexen-1-one (III). According to GS-MS analysis, the products mixture is composed of species formed by oxidation of double bond and allylic C-H. The epoxide selectivity was 54% for the hybrid based on g-C_3N_4 immobilized onto the ZnAlLDH/CuONP support. For this last catalyst, a

synergetic effect due to the presence of both base sites and copper metal sites well isolated and separated from each other, facilitated the epoxidation reaction [15]. In the present reaction system, the CH oxidation is accompanied by the side-reaction of H_2O_2 self-decomposition. The effective utilization of H_2O_2 was found to be 42% for ZnAlLDH, 56% for ZnAlLDH/CuONP and 63% for ZnAlLDH/g-C_3N_4/CuONP, respectively.

The most significant advantage of these new hybrid catalysts is their reusability. By measurements of initial reaction rates and conversions over five cycles, it was proved that the catalyst was still active during the fifth run, with a slight decrease of the initial TOF value.

4. CONCLUSIONS

Novel hybrid catalysts based on g-C_3N_4 and CuNP immobilized into ZnAlLDH matrix were prepared and tested in the process of oxidation of cyclohexene with 30% H_2O_2.

The joint action of the copper nanoparticles, the carbon nitride basicity and the LDH structure, beneficially contributed to the catalytic performance in comparison to their unmodified analogues.

The obtained results can pave the way for the development of new hybrid materials based on the joined ensemble of metal nanoparticles into LDH matrices with controllable basicity that could be used as highly effective heterogeneous oxidation catalysts.

References

1. F. Caveni, *Catal. Today*, 157 (**2010**) 8.
2. T. Forester, S.A. Schunk, S.A. Jenty and J.A. Lercher, *Chem. Commun.*, 47 (**2011**) 3254.
3. G. Cainelli and G.Cardillo, *Chromium Oxidation in Organic Chemistry*, Springer-Verlag, New York (1984).
4. A.B. Smith and J.P. Konopelski, *J. Org. Chem*., 49 (**1984**) 4094.
5. C.H. Zhou, *Appl. Clay Sci*., 53 (**2011**) 87.
6. Z.P. Xu, J. Zhang, M.O. Adebajo, H. Zhang and C. Zhou, *Appl. Clay Sci*., 53 (**2011**) 139.
7. G. Mikami, F. Grosu, S. Kawamura, Y.Yoshida, G. Carja and Y. Izumi, *Appl. Catal. B Environ.* 199 (**2016**) 260.
8. G. Carja, L. Dartu, K. Okada and E. Fortunato, *Chem. Eng. J.*, 222 (**2013**) 60.
9. S. Martha, K.H. Reddy, N. Biswal and K.M. Parida, *Dalton Trans*., 41 (**2012**) 14107.

10. S. Kannan, V. Rives and H. Knözinger, *J.Solid.State.Chem*., 177 (**2004**) 319.
11. E.M. Seftel, E. Popovici, M. Martens, P. Cool and E.F. Vansant, *Appl. Catal. B Environ.*, 84 (**2008**) 699.
12. A. Białas, P. Kuśtrowski, B. Dudek, Z. Piwowarska, A. Wach, M. Michalik and M. Kozak, *Thermochim. Acta*, 590 (**2014**) 191.
13. C.C. Chusuei, M.A. Brookshier and D.W. Goodman, Langmuir, 15 (**1999**) 2806.
14. S. Nayak, L. Mohapatra and K. Parida, *J. Mater. Chem. A*, 3 (**2015**) 18622.
15. M. Mureşeanu, I. Georgescu, L.E. Bibire and G.Cârjă, *Catal. Commun*., 54 (**2014**) 39.

Annals of the University of Craiova
The Chemistry Series
Volume XLIV, No. 1 (2017) 65-73
homepage: chimie.ucv.ro/anale/

Double-charged and mono-charged tautomeric forms of three hexacoordinated complex compounds of Fe(II)

Research article

Liana Simona Sbîrnă[1,*], *Anișoara Oubraham*[2], *Clementina Moldovan*[3], *Monica Mateescu*[1]

[1] University of Craiova, Faculty of Sciences, Department of Chemistry, Calea București, 107I, Craiova, Romania
[2] National R&D Institute for Cryogenics and Isotopic Technologies - ICIT Rm. Vâlcea, Romania
[3] University of Petroșani, Faculty of Mining, Department of Management, Environmental Engineering and Geology, Strada Universității, 20, Petroșani, Romania;
[*]e-mail: simona.sbirna@gmail.com

Received: 15.03.2017 / *Accepted*: 27.04.2017 / *Published*: 10.05.2017

Abstract
This paper presents the results of the elemental analysis, followed by a physical-chemical study (molar conductivity measurements, mass spectrometry and electronic spectroscopy) for three iron(II) complexes, containing a pyridine imine, 2-(pyridin-2-yl)-1*H*-benzo[*d*]imidazole, or two 2-(pyridin-2-yl)-1*H*-benzo[*d*]imidazole derivatives alongside two 2,2'-dipyridyl molecules. The results thus gathered (combined with the results of a quantum-mechanical study that will be reported in a further paper) lead to the deduction that all the complex compounds exhibit an octahedral geometry, having three (N, N) bidentate ligands.

Keywords: octahedral geometry; tautomeric forms; heterocyclic (N, N) ligands; Fe(II) complex compounds; spectral analysis

1. INTRODUCTION

The coordination chemistry has been significantly enriched due to the synthesis and characterization of a large number of six-coordinate octahedral complexes of the transition elements in which the metal is coordinated by nitrogen atoms. Particular attention has been given to the complex compounds formed by transition metals with heterocycles that act as bidentate ligands, using two nitrogen atoms as electron donors [1-3].

Within this area, three iron(II) complexes will be described here – containing a pyridine imine, namely 2-(pyridin-2-yl)-1*H*-benzo[*d*]imidazole, and two of its derivatives beside two 2,2'-dipyridyl molecules: 2-(1*H*-benzo[*d*]imidazol-2-yl) isonicotinic acid and prop-2-yn-1-yl 2-(1*H*-benzo[*d*]imidazol-2-yl)isonicotinate.

These complexes have been synthesized and then structurally were investigated by usual physical-chemical analysis (molar conductivity measurements, as well as mass spectrometry and electronic spectroscopy), preceded by elemental analysis [4].

All the data thus gathered (joint with the results of a quantum-mechanical study that will be reported in a further paper) have lead to the conclusion that all the complex compounds exhibit an octahedral geometry, the chemical bond obviously involving only nitrogen atoms as electron donors [5].

2. MATERIALS AND METHODS

2.1. Materials

The following reagents (Aldrich) were used in obtaining the three iron (II) complexes compounds presented within this study: ethanol, pyridine-2-carbaldehyde, 3,4-diaminobenzoic acid, copper acetate, sodium sulfide nonahydrate, hydrochloric acid, potassium hydroxide, dichloromethane, thionyl chloride, dimethylformamide, propargyl alcohol, triethylamine, potassium nitrate.

The elemental analysis was performed on a Perkin Elmer 2380 analyzer. The elemental analysis was performed on a Perkin Elmer 2380 analyzer. The molar conductivities were found in chloroform by using an OK-102 conductivity-meter at 300 K.

The mass spectra were obtained on a Mass Spectrometer Micromass LCT-type, by applying the ElectroSpray Ionization (ESI) technique. The electronic spectra were performed in 10^{-4} M ethanolic solutions, with an Ocean Optics spectrophotometer.

2.2. Methods

The first ligand, 2-(pyridin-2-yl)-1*H*-benzo[*d*]imidazole, denoted as L, was synthesized by an already published procedure, firstly obtaining its dihydrochloride and then recovering the ligand itself [5].

In order to obtain the second ligand, 2-(1*H*-benzo[*d*]imidazol-2-yl) isonicotinic acid, denoted as L', 2-(1*H*-benzo[*d*]imidazol-2-yl) isonicotinic acid dihydrochloride was formerly obtained: 12.82 g of pyridine-2-carbaldehyde were added to a mixture of a solution of 16.31 g of 3,4-diaminobenzoic acid in 150 ml of ethanol with a solution of 21.82 g of copper acetate in 250 ml of water, then the reaction mixture was heated for three hours on a boiling water bath. The redish-brown precipitate of the formed copper complex compound was filtered off and then dispersed in 150 ml of ethanol.

To decompose this complex, 51.58 g of $Na_2S{\cdot}9H_2O$ was put in the suspension, then the mixture was heated for two hours on the water bath, copper sulfide was filtered off from the hot solution and washed with hot water on the filter. The two filtrates were combined and highly acidified with hydrochloric acid. H_2S was removed from the solution by heating the water bath. On cooling the precipitated 2-(1*H*-benzo[*d*]imidazol-2-yl) isonicotinic acid dihydrochloride was filtered off to recrystallize it from the solvent [4].

The ligand itself, 2-(1*H*-benzo[*d*]imidazol-2-yl) isonicotinic acid (L') was obtained by mixing its dihydrochloride with an equivalent quantity of KOH in ethanol, the precipitated KCl was filtered off and finally the ethanol was distilled off.

In order to obtain the third ligand, namely prop-2-yn-1-yl 2-(1*H*-benzo[*d*]imidazol-2-yl) isonicotinate, denoted as L", prop-2-yn-1-yl 2-(1*H*-benzo[*d*]imidazol-2-yl) isonicotinate dihydrochloride was previously obtained: 1 g of $SOCl_2$ and one drop of DMF were added to a dispersion of 1 g of 2-(1*H*-benzo[*d*]imidazol-2-yl) isonicotinic acid dihydrochloride in 20 mL of dichloromethane; this mixture was heated for one hour on a water bath, the solvent was vacuum distilled, and 5 g of propargyl alcohol together with 0.9 g of triethylamine were added to the mixture in order to cool it; the reaction mixture was heated at the same time, continuously stirring for another hour on the water bath, then it was cooled, and poured into water.

The precipitate was filtered off, washed with water, and recrystallized from concentrated hydrochloric acid.

The ligand itself, prop-2-yn-1-yl 2-(1*H*-benzo[*d*]imidazol-2-yl) isonicotinate, (L") was recovered from its dihydrochloride by mixing it with an equivalent quantity of KOH in ethanol; the precipitated KCl was filtered off, and the ethanol was finally distilled off.

Iron complex compound $[Fe(dpy)_2Cl_2]{\cdot}2H_2O$ (dpy standing for 2,2'-dipyridyl) was synthesized by an already published method.[5]

To synthesize the three complex compounds, in each case, to an amount of 0,098 g of the crystalline complex $[Fe(dpy)_2Cl_2]\cdot 2H_2O$ were added 0.2 mmol ligand (L, L' or L") and then 10 ml of ethanol, thus obtaining a dark-purple solution.

The reaction mixture was boiled for three hours, while the solution turned redish-brown. The solvent was removed on a rotary evaporator, the oily residue was extracted with water, this solution being added to a saturated solution of potassium nitrate.

The isolated fine crystalline precipitate was finally filtered off, washed with diethyl ether and air dried.

3. RESULTS AND DISCUSSION

3.1. Structure of the ligands

The results obtained by elemental analysis for the three ligands involved in this study are the following:

L: 2-(pyridin-2-yl)-1*H*-benzo[*d*]imidazole dihydrochloride
Procentual formula found: %C 53.76; %H 4.15 %N 15.64; %Cl 26.45.
Procentual formula calcd.: %C 53.73; %H 4.11 %N 15.67; %Cl 26.49.
Molecular weight: 268
Molecular formula: $C_{12}H_{11}N_3Cl_2$
2-(pyridin-2-yl)-1*H*-benzo[*d*]imidazole
Procentual formula found: %C 73.90; %H 4.57; %N 21.53.
Procentual formula calcd.: %C 73.85; %H 4.61; %N 21.54.
Molecular weight: 195
Molecular formula: $C_{12}H_9N_3$

L': 2-(1*H*-benzo[*d*]imidazol-2-yl) isonicotinic acid dihydrochloride
Procentual formula found: %C 50; %H 3.5; %O 10.27; %N 13.5; %Cl 22.73.
Procentual formula calcd.: %C 50; %H 3.53; %O 10.26; %N 13.46; %Cl 22.75.
Molecular weight: 312
Molecular formula: $C_{13}H_{11}O_2N_3Cl_2$
2-(1*H*-benzo[*d*]imidazol-2-yl) isonicotinic acid
Procentual formula found: %C 65.23; %H 3.83; %O 13.38; %N 17.56.
Procentual formula calcd.: %C 65.27; %H 3.77; %O 13.39; %N 17.57.
Molecular weight: 239
Molecular formula: $C_{13}H_9O_2N_3$

L": prop-2-yn-1-yl 2-(1*H*-benzo[*d*]imidazol-2-yl) isonicotinate dihydrochloride
Procentual formula found: %C 54.9; %H 3.7; %O 9.16; %N 11.96; %Cl 20.27.

Procentual formula calcd.: %C 54.86; %H 3.71; %O 9.14; %N 12; %Cl 20.29.
Molecular weight: 350
Molecular formula: $C_{16}H_{13}O_2N_3Cl_2$
prop-2-yn-1-yl 2-(1*H*-benzo[*d*]imidazol-2-yl) isonicotinate
2-(1*H*-benzo[*d*]imidazol-2-yl) isonicotinic acid
Procentual formula found: %C 69.35; %H 3.98; %O 11.53; %N 15.14.
Procentual formula calcd.: %C 69.32; %H 3.97; %O 11.55; %N 15.16.
Molecular weight: 277
Molecular formula: $C_{16}H_{11}O_2N_3$

Their structural formulae are shown below.

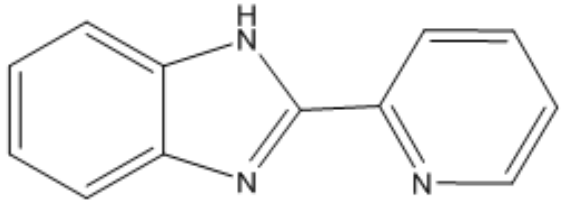

2-(pyridin-2-yl)-1H-benzo[*d*]imidazole (referred to as L)

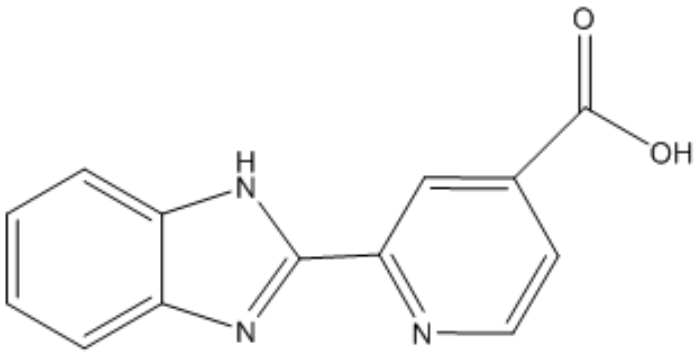

2-(1*H*-benzo[*d*]imidazol-2-yl)isonicotinic acid (referred to as L')

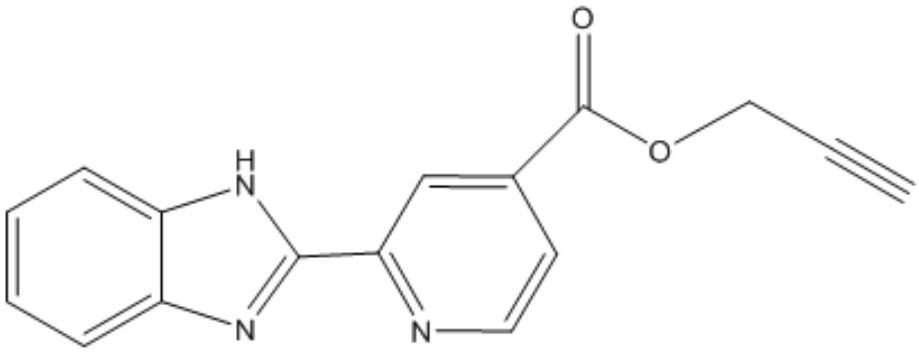

prop-2-yn-1-yl 2-(1H-benzo[*d*]imidazol-2-yl)isonicotinate (referred to as L")

In the reaction of the neutral complex $[Fe(dpy)_2Cl_2]\cdot 2H_2O$ with these three bidentate ligands of pyridylbenzimidazole series, a substitution occurs, specifically the one of the two chloroligands, leading to the formation of a double-charged cation in each case, thus resulting, $[Fe(dpy)_2L_2]^{2+}$, $[Fe(dpy)_2L'_2]^{2+}$ and $[Fe(dpy)_2L''_2]^{2+}$.

The substitution reactions may be written as follows, in the three cases taken for the present study:

$$[Fe(dpy)_2Cl_2]\cdot 2H_2O + L \rightarrow [Fe(dpy)_2L_2]^{2+} + 2Cl^- \quad (1)$$

$$[Fe(dpy)_2Cl_2]\cdot 2H_2O + L' \rightarrow [Fe(dpy)_2L'_2]^{2+} + 2Cl^- \quad (2)$$

$$[Fe(dpy)_2Cl_2]\cdot 2H_2O + L'' \rightarrow [Fe(dpy)_2L''_2]^{2+} + 2Cl^- \quad (3)$$

The composition of the complex compounds thus obtained, $[Fe(dpy)_2L_2]^{2+}$, $[Fe(dpy)_2L'_2]^{2+}$ and $[Fe(dpy)_2L''_2]^{2+}$ was found from the results of mass spectrometry measurements.

By using the ElectroSpray Ionization (ESI) technique, in the mass spectrum of the complex compound $[Fe(dpy)_2L_2]^{2+}$, molecular ion peaks were detected corresponding to double-charged and mono-charged forms of the complex.

The existence of these two forms originated from the possibility of deprotonation of the benzimidazole fragment in the ligand L, resulting in decrease by one unit of the charge and mass of the species.

In the mass spectra of the complex compounds $[Fe(dpy)_2L'_2]^{2+}$ and $[Fe(dpy)_2L''_2]^{2+}$, as in that of complex $[Fe(dpy)_2L_2]^{2+}$, two signals from molecular cations of each compound exhibited, corresponding to species with one and two positive charges.

In all these cases, the isotopic distribution within the molecular ions signals entirely corresponded to the theoretically calculated form of peaks for the presumed compositions of the complex compounds.

The results obtained by mass spectrometry measurements (ElectroSpray Ionization – EIS method) and molar conductivity measurements for the three complex compounds involved in this study are the following:

$[Fe(dpy)_2L_2]^{2+}$:
Mass spectrum, m/Z: 609.0, 305.5.
Molar conductivity: 1.89 $\Omega^{-1}\cdot cm^2\cdot mol^{-1}$ (it acts as an electrolyte).

$[Fe(dpy)_2L'_2]^{2+}$:
Mass spectrum, m/Z: 653.0, 327.8.
Molar conductivity: 1.93 $\Omega^{-1}\cdot cm^2\cdot mol^{-1}$ (it acts as an electrolyte).

$[Fe(dpy)_2L''_2]^{2+}$:
Mass spectrum, m/Z: 689.0, 342.3.
Molar conductivity: 1.97 $\Omega^{-1}\cdot cm^2\cdot mol^{-1}$ (it acts as an electrolyte).

3.2. Proposed structural formulae for the complex compounds

On this basis, structural formulae exhibiting an octrahedral geometry may be proposed for all these complex compounds. Their proposed structural formulae are shown in Figures 1-3.

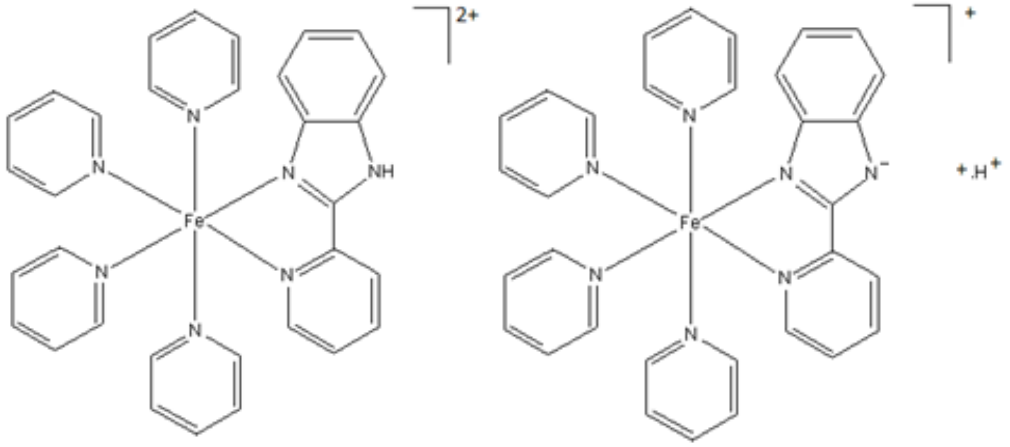

a) b)

Figure 1. Structural formula of $Fe(dpy)_2L_2]^{2+}$: a) double-charged form; b) mono-charged form

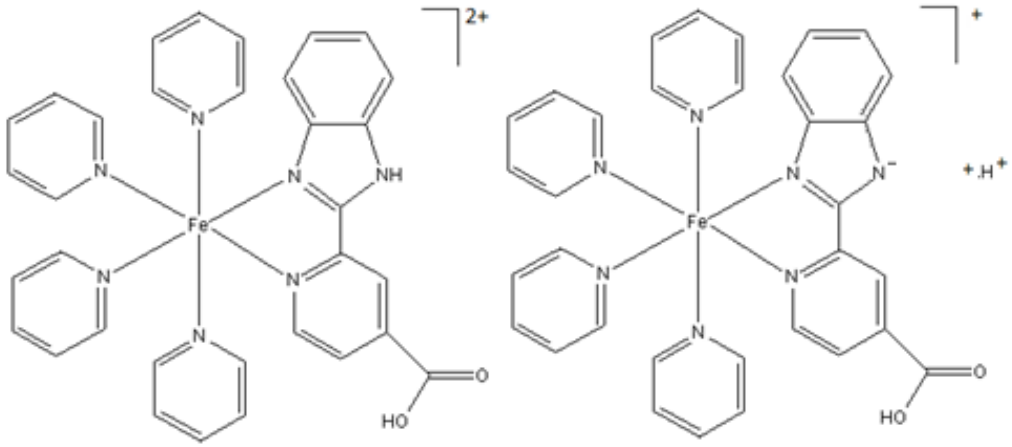

a) b)

Figure 2. Structural formula of $Fe(dpy)_2L'_2]^{2+}$: a) double-charged form; b) mono-charged form

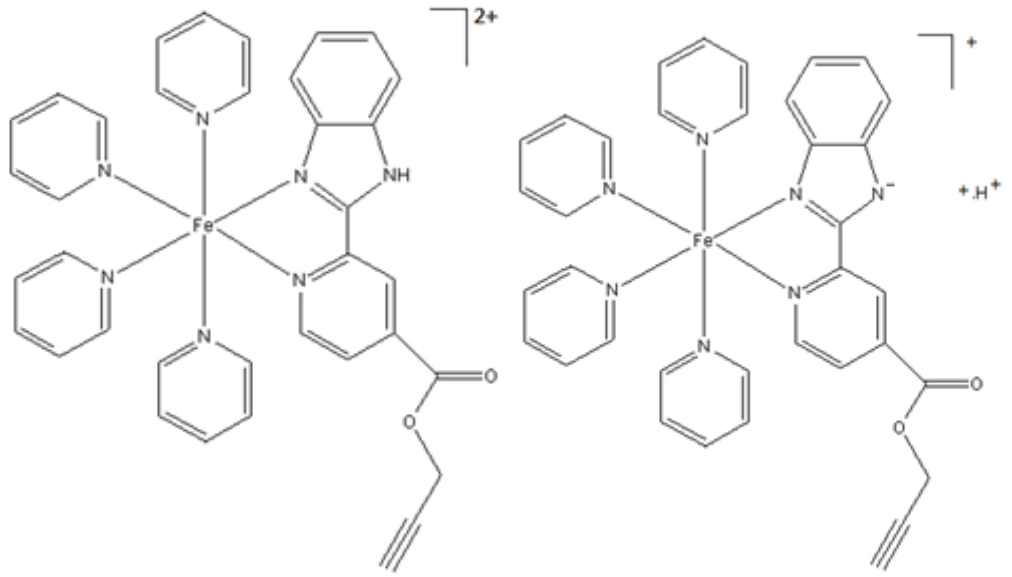

a) b)

Figure 3. Structural formula of $Fe(dpy)_2L''_2]^{2+}$: a) double-charged form; b) mono-charged form

As far as the electronic spectra are concerned, it was presumed that the introduction of these ligands into the composition of the complex compounds $[Fe(dpy)_2L_2]^{2+}$, $[Fe(dpy)_2L'_2]^{2+}$ and $[Fe(dpy)_2L''_2]^{2+}$ might lead to a shift of the absorption band in the visible region.

Indeed, due to the potential opportunity of the application of the iron(II) dipyridyl complexes for sunlight conversion, the visible part of the electronic spectra of these compounds is the most interesting.[6]

Experimental absorption spectra of the complex compounds $[Fe(dpy)_2L_2]^{2+}$, $[Fe(dpy)_2L'_2]^{2+}$ and $[Fe(dpy)_2L''_2]^{2+}$ performed in the visible range (in 10^{-4} M ethanolic solutions) is given in Figure 7.

All the three electronic spectra are characterized by a wide band having a maximum at about 460 nm (the extinction coefficient was about 3000 $l \cdot mol^{-1}cm^{-1}$, indicating that the presence of a substituent at the benzo[*d*]imidazole fragment of the first ligand (either –COOH or $–COO–CH_2–C\equiv CH$) does not significantly influence the absorption in the visible range. As compared to the iron(II) tris-dipyridyl complex, this band suffered a red shift by almost 10 nm, but its intensity in the absorption maximum is several times less than for the corresponding band of $[Fe(dpy)_3]^{2+}$.

4. CONCLUSIONS

About the complex compounds that this work dealt with, the first results (obtained by gathering information from their elemental composition, conductometric behavior, mass spectrometry and electronic spectroscopy) suggest that they all exhibit octrahedral geometry, two forms co-existing for them: a double-charged form and a mono-charged one, acting as electrolytes in both cases. As stated earlier, a quantum-mechanical study (confirming these conclusions) will be reported in a further paper.

References

1. J. O. Edwards, *Progress in Inorganic Chemistry - Inorganic Reaction Mechanism, Part 2*, John Wiley & Sons, New York (**2009**).
2. K. Nakamoto, *Infrared and Raman Spectra of Inorganic and Coordination Compounds, Part B*, John Wiley & Sons, New York (**2009**).
3. M. A. Haga, *Inorg. Chim. Acta*, 75 (**1983**) 29.
4. L. S. Sbîrnă, A. Reiss, A. Preda, F. Ciolan, I. Nicolaescu, *Rev. Roum. Chim.*, 56 (**2011**) 975.
5. L. S. Sbîrnă, A. Oubraham, I. Dabuleanu, F. Ciolan, *Annals of the University of Craiova, the Chemistry Series*, XLII/1 (**2013**) 25.

Annals of the University of Craiova
The Chemistry Series
Volume XLIV, No. 1 (2017) 74-83
homepage: chimie.ucv.ro/anale/

Extended Hückel Theory applied on three complex compounds formed by Fe(II) with two dipyridyl molecules and one ligand containing both pyridine and benzo[*d*]imidazole as heterocyclic rings

Research article

Liana Simona Sbîrnă[1*], *Sebastian Sbîrnă*[2], *Aurora Reiss*[1], *Monica Mateescu*[1]

[1] University of Craiova, Faculty of Sciences, Department of Chemistry, Calea București, 107I, Craiova, Romania
[2]Alro S. A., Strada Pitești, 116, Slatina, Romania
[*]e-mail: simona.sbirna@gmail.com

Received: 25.03.2017 / *Accepted*: 30.04.2017 / *Published*: 10.05.2017

Abstract
This paper reports the results of a quantum-mechanical study performed for two organic ligands, namely 2-(pyridin-2-yl)-1*H*-benzo[*d*]imidazole and two of its derivatives) and three of their complex compounds with iron(II), containing two 2,2'-dipyridyl molecules beside the above-mentioned ligands. For all of them, the results of the elemental analysis, as well as the ones of a physical-chemical study (involving molar conductivity measurements, together with mass and electronic spectroscopy) have been presented in a previous paper. The results support the deduction that all the complex compounds with three (N,N) bidentate ligands exhibit an octahedral geometry.

Keywords: octahedral complex compounds; heterocyclic (N,N) ligands; quantum-mechanical study; HOMO-LUMO method; EHT calculations

1. INTRODUCTION

In a previous paper [1], a study has been reported, involving three (N,N) heterocyclic ligands (2-(pyridin-2-yl)-1*H*-benzo[*d*]imidazole and two of its derivatives) and the three iron(II) complexes obtained whith each of them and two 2,2'-dipyridyl molecules. This study has suggested that the investigated complex compounds with these (N,N) bidentate ligands exhibit an octahedral geometry [2, 3]. The present work presents the results of a quantum-mechanical study about the previously investigated chemical compounds.

One of the reasons for the synthesis and investigation of these iron complexes involves was introducing into the coordination sphere of a complex possessing a photosensible moiety, $[Fe(dpy)_2]^{2+}$ a bidentate ligand of (N,N) type that would modify the electronic structure of the complex and thus would make it possible to utilize the energy of the quantum absorbed along one of the predetermined deactivation channels (luminescence, charge transfer, *etc*.).

Inasmuch as the directional synthesis of complexes with desired properties is impossible without the understanding of the relation between the composition of the coordination sphere, electronic structure of the complex, and the observed characteristics of its excited states [6, 7], a significant attention is paid to quantum-mechanical studies of the electronic structure of polypyridine iron complexes and to the interpretation of electronic spectra based on the calculations of the excited electronic states [4].

Within this study, we have investigated the effect on the spectral characteristics of the complexes of two substituents added to the ligand (–COOH, $–COO–CH_2–C\equiv CH$) located in the peripheral part of a pyridine imine, 2-(pyridin-2-yl)-1*H*-benzo[*d*]imidazole.

It was presumed that the introduction of these ligands into the composition of the studied polypyridine iron(II) complexes might result in a shift of the absorption band in the visible region, that presumption being confirmed by the electronic spectral analysis that we have formerly repoted [5].

2. MATERIALS AND METHODS

2.1. Materials

Preparation of the ligands, as well as the preparation of their complexes with Fe(II), were described in the anterior paper that we have mentioned above.

2.2. Methods

A specialised chemistry software, HyperChem 8.0.9.- trial version [5] was used for this quantum-mechanical study based on HOMO-LUMO EHT (Extended Hückel Theory) calculations [4].

3. RESULTS AND DISCUSSION

3.1. Computational modeling of ligands' structure

As far as the three organic compounds are concerned, we shall remind that they are the following ones: 2-(pyridin-2-yl)-1*H*-benzo[*d*]imidazole, 2-(1*H*-benzo[*d*]imidazol-2-yl) isonicotinic acid and prop-2-yn-1-yl 2-(1*H*-benzo[*d*]imidazol-2-yl)isonicotinate, and also that they will be reffered to as L, L'and L" respectively. Their structures (obtained by using the specialised chemistry software HyperChem 8.0.9.- trial version [5]) are shown in Figures 1-3:

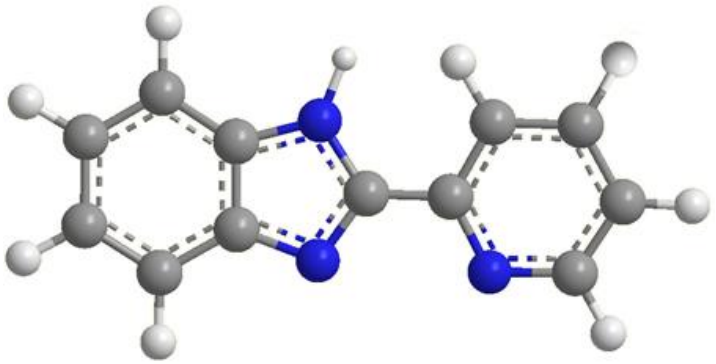

Figure 1. Computational modeling for the structure of the ligand L [5]

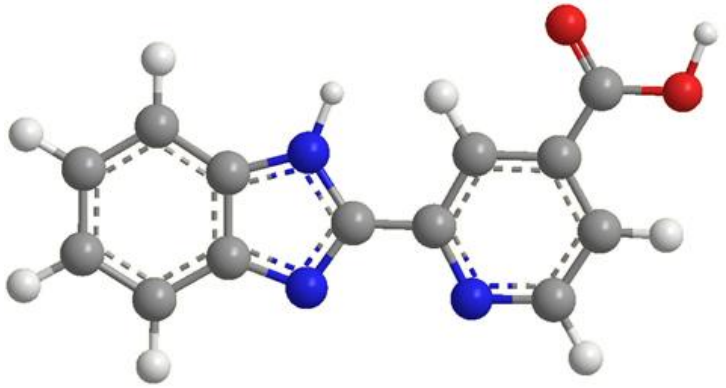

Figure 2. Computational modeling for the structure of the ligand L' [5]

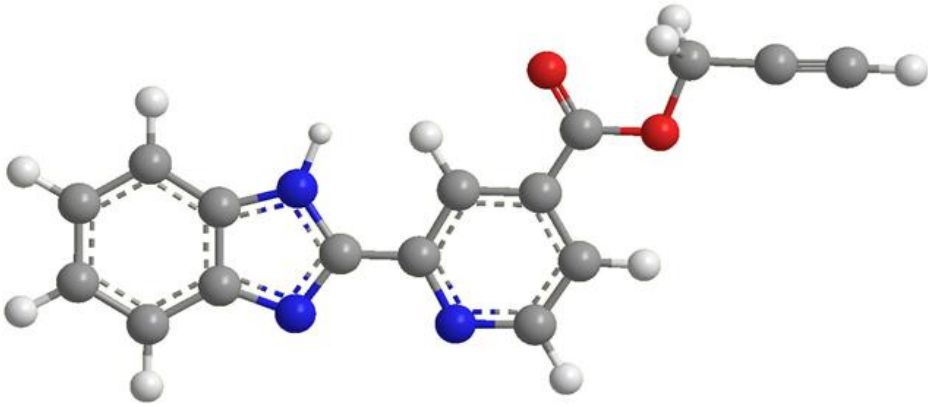

Figure 3. Computational modeling for the structure of the ligand L" [5]

The previous data sugest that they act as bidentate ligands in the complex compounds formed with Fe(II), involving nitrogen atoms in the coordination, so the chelate rings obtained contain five atoms each ($[Fe(dpy)_2L_2]^{2+}$, $[Fe(dpy)_2L'_2]^{2+}$ and $[Fe(dpy)_2L''_2]^{2+}$).

In order to verify the accuracy of this statement, a quantum-mechanical study was performed on the ligands and their corresponding complex compounds.

The molecular geometry was optimized using the Molecular Mechanics approach (MM^+), the cartesian coordinates for all the atoms being obtained by using HyperChem 8.0.9.- trial version [5].

The cartesian coordinates for all the atoms were used into the ICONC program – an improved version of ICON [4]. The VSIP's and Slater exponents have been those recommended by ICONC library, apart from the VSIP's for the 4*s*, 4*p* and 3*d* levels for the Fe^{2+} ion, that would lead to the unacceptable conclusion that the sigma coordinative bonding would have a "back-donation" character. Thus, these parameters were replaced by the ones proposed by Calzaferri and Brände [4], so the EHT calculations were performed without iteration upon charge and configuration, taking into account that the EHT practice has been shown that the results obtained this way seem to be more reliable.

3.2. EHT (HOMO-LUMO) calculation

In order to establish the electronic structure of the free ligands L, L' and L", a quantum-mechanical study was carried out in two modes: with the optimization of the geometric structures, and then using geometric parameters corresponding to the ligand state in the coordination sphere of the complex.

The ligands have planar structure. In their free state, the nitrogen atoms of the dipyridyl ligands, as well as the nitrogen atoms in the ligands, are in the *trans* position with regard to the C–C bond between the cyclic aromatic fragments.

Energies and contributions of different molecular fragments on the higher occupied molecular orbitals (HOMOs) and lower unoccupied molecular orbitals (LUMOs) of complex compounds (%) are presented in Table 1.

To facilitate the involvement in the coordination to the iron(II) ion, the three bidentate ligands should suffer a transition into a less energy state, this engaging a considerable rising of the energy of the molecular orbital (MO) ruling the donor properties of the ligand (~1.2 eV). The main contribution to this MO originates in the atomic orbitals of the nitrogen atoms located in the ligand plane. An orbital from the ligand dpy becomes the highest occupied molecular orbital (HOMO, simply denoted as "-0" in Table 1), whereas an orbital from the ligands L, L' or L" becomes HOMO-1 (simply denoted as "-1" in Table 1).

The energies of the other occupied frontier MOs suffer smaller changes (up to 0.2 eV) and can either increase or decrease.

The energy of the lowest unoccupied molecular orbital (LUMO, simply denoted as "+0" in Table 1) will be interesting in explaining the spectral characteristics of the studied complex compounds, remaining practically unchanged while the ligand conformation changes.

In the electronic state right before coordination, the LUMOs of ligand dpy and L, L' or L" (called "+0", "+1", "+2" *etc*.) have the same energy (within an accuracy of 0.05 eV). The presence of a substituent introduced at the benzo[*d*]imidazole fragment of the first ligand (–COOH or –COO–CH_2–C≡CH) leads to a decrease in energy of MOs formed by the AOs of the acceptor nitrogen atom. In particular, LUMO of the ligands L' and L" are lower by about 0.5 eV than LUMO of L.

In Table 1 energies and contributions of different molecular fragments on the higher occupied and lower unoccupied molecular orbitals of complexes (%) are presented of highest occupied and lowest unoccupied molecular orbitals of the three complex compounds, $[Fe(dpy)_2L_2]^{2+}$, $[Fe(dpy)_2L'_2]^{2+}$ and $[Fe(dpy)_2L"_2]^{2+}$.

The accounting for the solvation shell is found for the most part of the orbitals with an important contribution of substituent atoms.

Consequently, taking into account the large negative charge on the oxygen atoms of the substituent, the symmetry of the solvate shell of the complex seem to be distorted, so the energy of the corresponding MOs decrease compared to the energy of MOs localized on the dpy ligands of the studied complexes [8-10].

Amongst the frontier orbitals of all three complex compounds, the following orbitals can be stressed out as having a major contribution from the *d*-orbitals of the central iron(II) ion: (HOMO-2 ("-2"), HOMO-1 ("-1"), HOMO ("-0"), LUMO+12 ("+12"), LUMO+13 ("+13"), the rest of MOs being localized on the ligands.

The introduction of the acceptor substituent (–COO–CH_2–C≡CH or –COOH) into the the benzo[*d*]imidazole fragment of the ligand L affects the MO energy as follows [11]:

- additional MOs come out among the frontier MOs: for $[Fe(dpy)_2L'_2]^{2+}$: HOMO-7 ("-7"), LUMO+4 ("+4"); for $[Fe(dpy)_2L''_2]^{2+}$: HOMO-8 ("-8"), HOMO-7 ("-7"), LUMO+4 ("+4"), HOMO+12 ("+4"); therefore, the occupied orbitals (HOMOs) are practically localized on the atoms of the substituent, whereas the occupied orbitals (LUMOs) are delocalized over all ligand surrounding;

- the energy decreases for the MOs whose formation occur with the involvement of AOs of the substituent atoms with about 0.15 eV for HOMO-4 ("-4") and 0.24 eV for HOMO-3 ("-3"), (these being localized on the benzo[*d*]imidazole fragment with the contribution from the AOs of the substituent ~2% and ~4% respectively); a proportionality can be observed between the energy decrease of the MOs and the contribution of the acceptor fragment to the MOs (as presented in Table 1);

- the gap that appears between the HOMO and LUMO in complexes $[Fe(dpy)_2L'_2]^{2+}$ and $[Fe(dpy)_2L''_2]^{2+}$ decreses by about 0.2 eV compared with the one in complex $[Fe(dpy)_2L_2]^{2+}$.

The effective charges distribution on atoms (calculated by using the EHT method) in the three complexes – $[Fe(dpy)_2L_2]^{2+}$, $[Fe(dpy)_2L'_2]^{2+}$ and $[Fe(dpy)_2L''_2]^{2+}$ – are quite identical except for the benzene ring in the ligands L, L' or L'' – where the charge distribution depends on the presence of the substituent.

By introducing the carboxylic substituent, the negative charge on the carbon atom increases, so the atoms next to it become less negative.

Moreover, introducing the prop-2-yn-1-yl fragment leads to a stronger polarization of the benzene ring.

The same charge on the central atom in all the three complexes indicates the equal degree of the overall transfer of the electron density during the formation of the coordinative bond metal-ligand in these compounds, disregarding the presence of a substituent at the benzene ring [11].

As previously stated, all these observations may be made by carefully analyzing the computational results gathered in Table 1, presenting the energies and contributions of different molecular fragments on the higher occupied molecular orbitals (HOMOs) and lower unoccupied molecular orbitals (LUMOs).

Table 1. Energies and contributions of different molecular fragments on the higher occupied molecular orbitals (HOMOs) and lower unoccupied molecular orbitals (LUMOs) of complex compounds (%)

	Complex compound																	
	$[Fe(dpy)_2L_2]^{2+}$					$[Fe(dpy)_2L'_2]^{2+}$						$[Fe(dpy)_2L''_2]^{2+}$						
MO	E,eV	Fe(II)	dpy1	dpy2	L *	E,eV	Fe(II)	dpy1	dpy2	*	L' **	E,eV	Fe(II)	dpy1	dpy2	*	L'' **	***
-10	-8.76	2.3	78.1	5.3	14.3	-8.70	0.7	8.1	55.3	35.7	0.2	-8.54	0.0	0.2	0.3	10.4	53.7	35.3
-9	-8.67	0.6	7.8	51.5	40.0	-8.61	0.3	44.5	50.8	4.4	0.2	-8.53	0.3	1.1	2.4	91.0	4.7	0.4
-8	-8.62	0.3	44.7	50.1	4.9	-8.52	0.3	1.1	2.3	90.3	6.1	-8.05	0.0	0.0	0.0	11.4	48.5	40.2
-7	-8.40	0.4	1.2	1.6	96.8	-8.16	0.0	0.0	0.0	15.9	84.0	-7.96	0.1	0.1	0.0	1.6	5.7	92.5
-6	-7.42	1.4	55.7	41.3	1.6	-7.45	2.4	63.3	24.2	9.6	0.4	-7.45	2.3	62.1	26.2	8.7	0.4	0.2
-5	-7.38	0.5	41.0	57.7	0.8	-7.40	0.8	22.0	74.4	2.8	0.0	-7.40	0.8	23.7	72.3	3.0	0.0	0.0
-4	-7.06	8.8	5.6	1.2	84.4	-7.29	5.7	16.8	0.9	74.8	1.9	-7.29	5.5	15.8	0.8	75.3	1.8	0.7
-3	-6.88	2.5	0.8	0.6	96.2	-7.19	1.0	0.5	0.8	93.7	4.0	-7.20	1.3	0.7	0.9	92.5	4.1	0.5
-2	-6.13	74.2	7.9	10.5	7.5	-6.19	74.3	7.9	10.4	7.4	0.0	-6.19	74.3	7.9	10.4	7.4	0.0	0.0
-1	-6.05	72.4	9.4	6.4	11.8	-6.11	72.4	9.4	6.5	11.7	0.1	-6.12	72.4	9.4	6.5	11.7	0.1	0.0
-0	-5.89	71.9	6.3	7.6	14.2	-5.96	73.1	6.6	7.6	11.7	0.2	-5.97	73.9	6.6	7.6	11.7	0.2	0.0
+0	-2.63	0.2	28.8	40.4	30.6	-2.84	1.9	2.4	3.0	85.9	6.7	-2.85	1.9	2.3	2.8	85.3	7.3	0.4
+1	-2.52	5.9	54.9	2.1	37.1	-2.61	3.2	44.2	47.9	4.3	0.5	-2.62	3.1	42.9	49.4	4.1	0.5	0.0
+2	-2.52	6.3	11.5	52.5	29.6	-2.55	6.3	48.4	44.0	1.3	0.0	-2.55	6.3	49.7	42.7	1.3	0.0	0.0
+3	-1.82	1.0	34.1	43.0	21.9	-1.93	1.1	12.2	15.4	58.9	12.4	-1.95	1.2	9.8	12.2	60.3	15.5	0.9
+4	-1.60	1.7	36.7	2.7	58.9	-1.77	2.3	31.6	32.0	23.3	10.7	-1.78	2.2	31.9	34.8	20.3	10.2	0.6
+5	-1.54	2.2	45.3	48.5	4.0	-1.60	1.3	34.3	4.4	53.8	6.2	-1.61	1.3	33.6	2.4	57.0	5.4	0.4
+6	-1.49	2.2	17.0	75.8	5.0	-1.57	2.1	46.3	45.0	6.1	0.4	-1.57	2.2	46.1	46.8	4.7	0.2	0.0
+7	-1.45	1.4	61.7	24.5	12.3	-1.50	1.8	11.2	78.3	7.8	0.9	-1.50	1.9	12.3	77.7	7.3	0.7	0.0
+8	-0.61	2.0	2.3	1.1	94.6	-1.47	1.2	59.7	20.3	17.8	0.9	-1.48	1.2	61.5	21.2	15.4	0.6	0.0
+9	-0.26	0.7	28.8	43.8	26.7	-0.78	1.3	2.3	0.9	95.0	0.4	-0.78	1.3	2.3	0.9	94.9	0.4	0.1
+10	-0.19	0.8	28.0	6.7	64.5	-0.26	0.9	46.4	49.8	2.9	0.0	-0.26	0.9	45.6	50.5	2.9	0.0	0.0
+11	-0.14	0.9	45.1	49.1	5.0	-0.16	0.8	51.4	46.6	1.2	0.0	-0.16	0.8	52.2	45.8	1.2	0.0	0.0
+12	0.01	42.1	24.0	9.1	24.6	-0.04	42.5	22.0	30.3	25.1	0.0	-0.09	3.4	1.1	1.5	18.3	18.9	56.8
+13	0.08	42.2	17.6	31.5	8.7	-0.02	42.1	19.5	30.4	8.0	0.0	-0.04	41.2	22.3	9.5	23.9	0.7	2.4

* - the benzo[*d*]imidazole fragment
** - the carboxyl group
*** - the prop-2-yn-1-yl fragment

3.3. Comparison between the experimental and theoretical spectra

Whithin this study, the experimental and theoretical spectra were compared. Therfore, this calculation method allowed a detailed analysis about the effect of the substituents on the absorption electronical spectrum of the three iron(II) complex compounds (all the three spectra were presented in the previous paper [1]). As far as the electronic spectrum is concerned, it was presumed that the introduction of these ligands into the composition of the complex compounds $[Fe(dpy)_2L_2]^{2+}$, $[Fe(dpy)_2L'_2]^{2+}$ and $[Fe(dpy)_2L''_2]^{2+}$ might lead to a shift of the absorption band in the visible region [11].

Indeed, due to the potential opportunity of the application of the iron(II) dipyridyl complexes for sunlight conversion, the visible part of the electronic spectra of these compounds is the most interesting.[1]

Experimental absorption spectra of the complex compounds performed in the visible range (in 10^{-4} M ethanolic solutions) was given in the former paper[1]. All the three electronic spectra are characterized by a wide band having a maximum at about 460 nm (the extinction coefficient was 3000 $l \cdot mol^{-1}cm^{-1}$, indicating that the presence of a substituent introduced at the benzo[*d*]imidazole fragment of the first ligand (either –COOH or –COO–CH_2–C≡CH) does not significantly influence the absorption spectrum in the visible range [1].

None of the energies over 4.5 eV occurring in the experimental spectrum in the region 200-250 nm was taken into account. Although the energy of the transitions was overestimated in some way (by 0.2-0.3 eV), the results of this calculation were consistent with the experimental findings.

To be more specific, the performed HOMO-LUMO EHT calculations [4] showed that the absorption spectrum of al the three complex compounds taken into study shall be divided in three regions [11]:

- the first region (2.5-3.5 eV) corresponds only to charge-transfer (CT) transitions from the 4*d* orbitals of Fe(II) to antibonding orbitals of the ligand surrounding, n*(L, L' or L"); the close energy values of the low unoccupied MOs of ligands dpy and L, L' or L" provides an availability of their mixing within the complex leading to a delocalization of the electron density obtaineded by photo-excitation over the three ligands (dpy1, dpy 2 and L, L' or L");
- the second region (3.5-4.2 eV) involves mixed transitions where MOs of different kinds are involved: from *d*(Fe) to either n (L, L' or L") or n* (L, L' or L").
- the third region (the one over 4.2 eV) generally contains the ligand-ligand MO transitions.

Although the presence of an acceptor substituent in ligands L' and L" leads to a lower energy in the corresponding n* MO and therefore to the already mentioned reduced energy gap between the occupied and occupied molecular orbitals (HOMOs and LUMOs) of complexes $[Fe(dpy)_2L'_2]^{2+}$ and $[Fe(dpy)_2L''_2]^{2+}$, these facts do not create a considerable modification of the waves in the first region, whereas the lowest energy transitions (HOMO-LUMO transitions) in the complexes $[Fe(dpy)_2]^{2+}$, $[Fe(dpy)_2L'_2]^{2+}$ and $[Fe(dpy)_2L''_2]^{2+}$ are similar for the three complex compounds. Therefore, the results obtained by EHT procedure [4] are presented in Table 2 for only one of them, $[Fe(dpy)_2L_2]^2$.

The MOs with a large contribution (over 70%) of AOs of the carboxylic substituent (–COOH or –COO–CH_2–C≡CH) only take part in the transitions of high energy (*i.e.,* over the energy of 4.2 eV).

Table 2. Theoretical and experimental values of energy, the oscillator force and the extinction coefficient for different HOMO-LUMO transitions in the complex compound $[Fe(dpy)_2L_2]^{2+}$ (the other two tables are similar)

Theoretical spectrum		Assignment			Experimental spectrum	
E, eV	Oscillator force, f				E, eV	Extinction coefficient
2.64	0.0140	*d*(Fe)	—	dpy1, dpy2, L	2.56	2810
		d(Fe)	—	π(Fe-dpy1), δ(Fe- L)		
		d(Fe)	—	δ(Fe-dpy2), δ(Fe- L)		
2.78	0.1204	*d*(Fe)	—	dpy1, dpy2, L		
		d(Fe)	—	π(Fe-dpy1), δ(Fe-L)	2.69	2010
		d(Fe)	—	δ(Fe-dpy2), δ(Fe-L)		
2.82	0.1331	*d*(Fe)	—	π(Fe-dpy1), δ(Fe-L)		
		d(Fe)	—	δ(Fe-dpy2), δ(Fe-L)		
3.61	0.0237	*d*(Fe)	—	dpy2, dpy1	3.54	3300
3.65	0.0375	*d*(Fe)	—	dpy1, dpy2		
		d(Fe)	—	L, dpy1		
3.70	0.0241	*d*(Fe)	—	L, dpy1		
		d(Fe)	—	σ(Fe-dpy2), σ(Fe-dpy1), σ(Fe-L)		
3.73	0.0328	*d*(Fe)	—	L, dpy1	3.94	1782
		L	—	dpy1, dpy2, L		
		d(Fe)	—	σ(Fe-dpy2), σ(Fe-dpy1), σ(Fe-L)		
3.75	0.0428	L	—	dpy1, dpy2, L		
		L	—	π(Fe-dpy1), δ(Fe- L)		
3.78	0.0855	*d*(Fe)	—	L, dpy1		
		L	—	π(Fe-dpy1), δ(Fe-L)		
3.76	0.0935	*d*(Fe)	—	dpy2, dpy1		
		d(Fe)	—	L, dpy1		
		d(Fe)	—	dpy1, dpy2		
3.82	0.0465	*d*(Fe)	—	dpy2, dpy1		
		L	—	π(Fe-dpy1), δ(Fe-L)		
		d(Fe)	—	dpy1, dpy2		
3.87	0.0434	*d*(Fe)	—	dpy1, dpy2		
3.88	0.0431	L	—	δ(Fe-dpy2), δ(Fe-L)		
		d(Fe)	—	dpy1		
		d(Fe)	—	dpy2		
3.89	0.0350	*d*(Fe)	—	dpy1, dpy2		
		d(Fe)	—	σ(Fe-dpy2), σ(Fe-dpy1), σ(Fe-L)		
3.91	0.0635	*d*(Fe)	—	σ(Fe-dpy2), σ(Fe-dpy1), σ(Fe-L)		
		d(Fe)	—	dpy1, dpy2		
3.94	0.2302	L	—	π(Fe-dpy1), δ(Fe-L)		
		L	—	δ(Fe-dpy2), δ(Fe-L)		
		π(Fe-pb)	—	π(Fe-dpy1), δ(Fe- L)		
4.00	0.1449	π(Fe-pb)	—	π(Fe-dpy1), δ(Fe-L)		
4.01	0.1462	*d*(Fe)	—	dpy1, dpy2	4.32	2310
		*d**(Fe)	—	dpy2, dpy1		
4.25	0.0193	dpy2, dpy1	—	dpy1, dpy2, L		
4.29	0.0210	dpy1, dpy2	—	dpy1, dpy2, L		
		dpy2, dpy1	—	δ(Fe-dpy2), δ(Fe- L)		
4.42	0.2582	dpy1, dpy2	—	δ(Fe-dpy2), δ(Fe- L)		
		dpy1, dpy2	—	π(Fe-dpy1), δ(Fe- L)		
4.44	0.0142	dpy2, dpy1	—	δ(Fe-dpy2), δ(Fe-L)		
		dpy1, dpy2	—	dpy1, dpy2, L		
4.48	0.0515	*d*(Fe)	—	σ(Fe-dpy2), σ(Fe-dpy1), σ(Fe-L)		
4.53	0.0597	L	—	dpy1, dpy2, L		

4. CONCLUSIONS

The quantum-mechanical study consisting in HOMO-LUMO EHT calculations (based on specialised chemistry software), supports the already presented1 statement that the complex compounds of Fe(II) with one of the ligands (L, L' or L") along with two dpy ligands are octahedral, the three bidentate ligands being coordinated by means of nitrogen atoms to the central metal ion. Moreover, L' and L" are able to act as bridging ligands in supra-molecular structures.

The comparison between the experimental and theoretical spectra shows that complexes $[Fe(dpy)_2L'_2]^{2+}$ and $[Fe(dpy)_2L"_2]^{2+}$ exhibit absorption in the same spectral region of the spectrum as $[Fe(dpy)_3]^{2+}$.

Moreover, the complex compound $[Fe(dpy)_2L_2]^{2+}$ proved itself to exhibit the availability to act as an "antenna", so that the ligands L' and L", containing in their structure a second group able to be involved in the coordination to the Fe(II) ion, may be used as "bridging ligands" in the synthesis of polynuclear supramolecular structures of the "antenna-bridge" kind.

References

1. L. S. Sbîrnă, A. Oubraham, C. S. Moldovan, *Annals of the University of Craiova, the Chemistry Series*, XLIV/1 (**2017**) 67.
2. J. F. Jensen, *Introduction to Computational Chemistry*, 3rd Edition, Wiley (**2016**).
3. C. J. Cramer, *Essentials of Computational Chemistry: Theories and Models*, 3rd Edition, Wiley (**2015**).
4. Calzaferri G., Brände M., *QCPE Bulletin*. 73 (**1992**) 1020.
5. www.hyper.com
6. J. O. Edwards, *Progress in Inorganic Chemistry - Inorganic Reaction Mechanism, Part 2*, John Wiley & Sons, New York (**2009**).
7. K. Nakamoto, *Infrared and Raman Spectra of Inorganic and Coordination Compounds, Part B*, John Wiley & Sons, New York (**2009**).
8. F. L. Pilar, *Elementary quantum chemistry*. 2nd edition, Dover Publications (**2011**).
9. S. I. Pechenyuk, D. P. Domonov, *J. Struct. Chem.*, 52 (**2011**) 412.
10. R. A. Evarestov, *Quant. Chem. Solids*. 153 (**2012**) 201.
11. L. S. Sbîrnă, S. Sbîrnă, *Annals of the University of Craiova, the Chemistry Series*, XLII/2 (**2013**) 42.

Annals of the University of Craiova
The Chemistry Series
Volume XLIV, No. 1 (2017) 84-92
homepage: chimie.ucv.ro/anale/

The electrochemical response of tartrazine in electrified salted aqueous solution

Research article

Bogdan Tutunaru[*], *Cristian Neamțu, Cristian Tigae, Aurelian Dobrițescu, Cezar Spînu*

University of Craiova, Faculty of Sciences, Department of Chemistry, Calea București, 107i, Craiova, Romania
[*]e-mail: tutunaruchim@yahoo.com

Received: 23.02.2017 / *Accepted*: 17.03.2017 / *Published*: 10.05.2017

Abstract
The effect of food additives on human health and on the environment has been widely investigated. Their electrochemical degradation / mineralization constitute an important method to transforms these chemical compounds into harmless ones.
In this study we investigated the electrochemical behavior of tartrazine (TRZ) food additive (E102) in the presence of NaCl and Na_2SO_4 supporting electrolyte using the cyclic voltammetry method and current constant density electrolysis. The variation of dye concentration in time was analyzed by UV-Vis spectrophotommetry.
The presence of different supporting electrolyte leads to different degradation / mineralization processes of tartrazine.

Keywords: tartrazine, electrochemical degradation, electroactive species, degradation degree

1. INTRODUCTION

Synthetic organic dyes are widely used in industrial processes such as: confectionery, beverages, drugs colorants, textile dye. Although they presents some advantages (stability to acids, light, temperature, oxygen), on the other hand represents a source of pollution, and consumed in high quantity are genotoxic to humans and animals [1, 2]. Di(Azoic) dyes are one of the synthetic dye types with a large use in food, cosmetic, textile and pharmaceutical processing. Based on their individual physico-chemical properties, diverse electrochemical, spectrophotometric and thermic methods have been reported for the characterization, determination, retention and degradation of single or mixed dyes [3-10].

It was observed that after systemic exposure of mice to tartrazine resulted in gut and hepatic inflammation without periportal inflammatory cell recruitment [11]. The genotoxic, cytotoxic and cytostatic potentials of food dyes, tartrazine, amaranth and erythrozine have been tested in human peripheral blood cells. The authors [12] observed that amaranth (8 mM) presents genotoxicity, cytotoxicity and cytostaticity, tartrazine is toxic at 8 and 4 mM and erythrozine shows high cytotoxicity and cytostaticity at 2, 4 and 8 mM.

The content of tartrazine in food products must be controlled due its negative effects. Multi-walled carbon nanotubes were used for the electrochemical determination of tartrazine [13], Ponceau 4R and Allura red [14]. ZnO/cysteic acid nanocomposite electrochemically deposited on glassy carbon electrode was used for simultaneous determination of tartrazine and sunset yellow [15]. Modified gas diffusion electrode [16]; alumina microfibers-based sensor [17] and expanded graphite paste electrode [18] were used for electrochemical determination/degradation of tartrazine, Ponceau 4R and Amaranth.

Also, tartrazine was used in the preparation of active electrodes used for removing heavy metal ions, Pb(II), Cd(II) and Cr(III) [19, 20].

The removal of tartrazine has been investigated using TiO2 catalyst under UV light [21]; carbon nanotubes decorated with silver nanoparticles [22]; Photo-Fenton process [23] or using electrocoagulation coupled with electrochemical advanced oxidation processes [24].

This work reports the results of direct and indirect electrochemical degradation of tartrazine food dye by constant current density on platinum electrode.

2. MATERIALS AND METHODS

2.1. Materials

Tartrazine (IUPAC name: trisodium 5 - hydroxyl - 1 - (4 - sulfonatophenyl) - 4 - [(E) - (4 - sulfonatophenyl) diazenyl] - 1H - pyrazole - 3 - carboxylate), commonly known as E number - E102 was purchased in the form of crystalline powder from a local confectionery.

NaCl and Na_2SO_4 were purchased from Sigma-Aldrich and it presented analytical reagent grade. For achieving the aqueous electrolyte solutions was used bidistilled water. The electrochemical cell used was made of heat resistant glass and was jacketed thermostatic.

Metallic electrodes (anode and cathode) used in the electrochemical assembly were made of pure platinum plate (99.99 %) and were of Sigma-Aldrich provenience (active surface = 2 cm^2). The reference electrode was represented by the $Ag/AgCl,KCl_{sat}$ electrode.

2.2. Methods

Three stock solutions were prepared as follows: i) 100 mL 10^{-3} $mol \cdot L^{-1}$ tartrazine solution; ii) 100 mL 1.0 $mol \cdot L^{-1}$ NaCl solution; iii) 100 mL 1.0 $mol \cdot L^{-1}$ Na_2SO_4 solution. For the preparation of working solutions were taken the appropriate volumes of stock solution and diluted accordingly to obtain 100 mL mixed solution: a) $5 \cdot 10^{-5}$ $mol \cdot L^{-1}$ TRZ, 10^{-1} $mol \cdot L^{-1}$ NaCl and b) $5 \cdot 10^{-5}$ $mol \cdot L^{-1}$ TRZ, 10^{-1} $mol \cdot L^{-1}$ Na_2SO_4.

Cyclic voltammograms of the platinum electrode in supporting electrolyte solution, both in the absence and presence of tartrazine, were recorded using the dynamic electrochemical system VoltaLab 40 with VoltaMaster 4 software. In all cases, the scanning rate of the working electrode potential was of 100 $mV \cdot s^{-1}$.

Electrolysis at constant current density (50 $mA \cdot cm^{-2}$) of the tartrazine solution, in the presence of various supporting electrolytes, was made using also the dynamic electrochemical system VoltaLab 40. The electrolysis was carried out under dynamic condition of agitation.

Tartrazine solutions were spectrophotometrically analyzed at different times of the electrolysis process. Thus, the UV-Vis spectra of solutions were recorded in the wavelength range of 200-400 nm using a Varian Cary conc. spectrophotometer equipped with a quartz cuvette.

3. RESULTS AND DISCUSSION

3.1. Direct electrochemical degradation of tartrazine (TRZ)

3.1.1. Cyclic voltammetry study

Direct electrochemical degradation of tartrazine was studied by cyclic voltammetry associated with UV-VIS spectrophotometry using sodium sulfate as the supporting electrolyte. Figure 1 presents the cyclic voltammograms of the platinum electrode in the 10^{-1} mol·L^{-1} sodium sulphate solution in the absence and in the presence of $5 \cdot 10^{-5}$ mol·L^{-1} tartrazine. Into this figure are inserted the detail of cyclic voltammograms at low values of current densities and the UV-Vis spectra of the solution before and after recording the cyclic voltammograms.

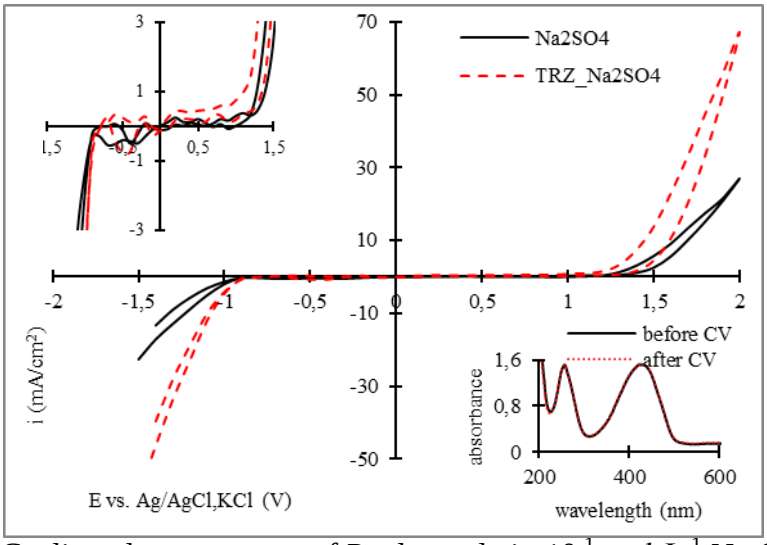

Figure 1: Cyclic voltammograms of Pt electrode in 10^{-1} mol·L^{-1} Na_2SO_4 in the absence and in the presence of $5 \cdot 10^{-5}$ mol·L^{-1} TRZ, sweep rate 100 mV·s^{-1}.

As can be seen from Figure 1, the two voltammograms are very similar and they differ only at high values of anodic (> 1.5 V) and cathodic (< -1.0 V) potentials. At potential values greater than 1.5 V, the values of recorded current densities are much higher when in the electrolyte solution are present the tartrazine molecules; this shows an increase in the electron transfer processes at the interface of metal / electrolyte solution.

The UV-Vis spectra of $5 \cdot 10^{-5}$ mol·L^{-1} tartrazine in 10^{-1} mol·L^{-1} Na_2SO_4 solution, before and after cyclic voltammogram registration are presented in insert of Figure 1. According to these spectra, it is observed that the absorbance values are almost identical for the two cases. At a high scanning rate of working

potential, used for recording the cyclic voltammograms, the electrochemical degradation of TRZ is very small.

3.1.2. Constant current density electrolysis / Spectrophotometry

Constant current density electrolysis (50 $mA \cdot cm^{-2}$) was performed over a time period of one hour. Tartrazine solution was spectrophotometrically analyzed during electrolysis. The UV-Vis spectra of $5 \cdot 10^{-5}$ $mol \cdot L^{-1}$ TRZ, 10^{-1} $mol \cdot L^{-1}$ Na_2SO_4 electrolyzed solution, registered form 10 to 10 mins. are presented in Figure 2.

The initial spectrum, registered before the start of electrolysis, shows one absorption peak at 430 nm, in the Visible domain, attributed to extended chromophore system and one absorption peak around 258 nm in the Ultraviolet domain.

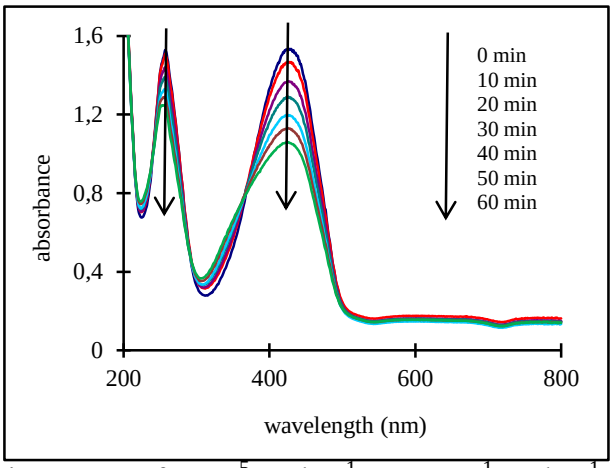

Figure 2: UV-Vis spectra of $5 \cdot 10^{-5}$ $mol \cdot L^{-1}$ TRZ, 10^{-1} $mol \cdot L^{-1}$ Na_2SO_4 solution at different times of electrolysis.

The electrochemical degradation process of tartrazine molecules in the presence of the sodium sulfate supporting electrolyte was evaluated by monitoring the absorbances values at λ = 430 nm. The electrochemical degradation degree (%) of azorubine was calculated with the following equation:

$$electrochemical\ degradation\ (\%) = \left(\frac{A_0 - A_t}{A_0}\right) \cdot 100$$

where A_0 is the initial value of absorbance (time = 0 min.), and A_t is the absorbance of tratrazine solution at reaction time t (min.).

The values of absorbance registered at the characteristic wavelength of 430 nm decrease with the increasing of time value (Figure 2). This indicates

that the tartrazine molecules are degradated over time, reaching a degree of electrochemical degradation of approximately 37 % at the end of the electrolysis (t = 60 min.).

3.2. Indirect electrochemical degradation of tartrazine (TRZ)

3.2.1. Cyclic voltammetry study

Indirect electrochemical degradation of tartrazine was studied by cyclic voltammetry associated with UV-VIS spectrophotometry using sodium chloride as the supporting electrolyte. Figure 3 presents the cyclic voltammograms of the platinum electrode in the 10^{-1} mol·L^{-1} sodium chloride solution, in the absence and in the presence of $5 \cdot 10^{-5}$ mol·L^{-1} tartrazine. Into this figure are inserted the detail of cyclic voltammograms at low values of current densities and the UV-Vis spectra of the solution before and after recording the cyclic voltammograms.

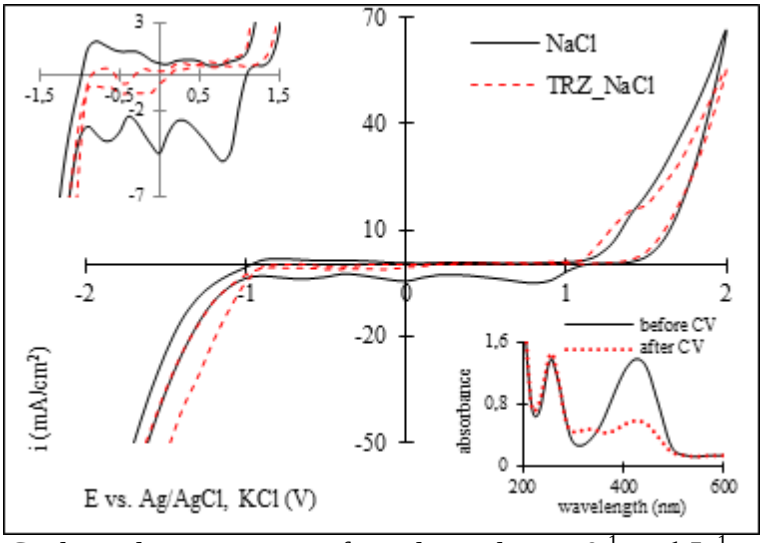

Figure 3: Cyclic voltammograms of Pt electrode in 10^{-1} mol·L^{-1} NaCl in the absence and in the presence of $5 \cdot 10^{-5}$ mol·L^{-1} TRZ, sweep rate 100 mV·s^{-1}.

Cyclic voltammograms of the Pt electrode (Figure 3) shows a decrease of current densities in the presence of tartrazine molecules. Chloride anions are reduced at the platinum electrode to form clorine molecules, which reacts with water molecules to forms hypochlorite anions. Consequently, the tartrazine molecules are indirectly degraded by hypochlorite anions. The detail of cyclic voltammograms shows the presence of current density peaks attributed to electrochemical generation of chloride active species. The cyclic voltammogram recorded in the presence of tartrazine indicates the appearance

of a new peak (1.4 V vs. Ag/AgCl,KCl) of current density, this peak being most probably attributed to the electro-oxidation of organic dye molecules.

The interaction of tartrazine molecules with active chloride ions is one of the strongest interactions. The UV-Vis spectra of $5 \cdot 10^{-5}$ mol·L^{-1} tartrazine, 10^{-1} mol·L^{-1} NaCl solution, before and after cyclic voltammogram registration, shows that the absorbance value decreases significantly. Only by recording the cyclic voltammogram, the chromophore system of tartrazine is electrochemical degraded approximately 75 %, according to the UV-Vis spectra inserted in Figure 3.

3.2.2. Constant current density electrolysis / Spectrophotometry

Indirect electrochemical degradation of E102 food dye was studied by the electrolysis of the salted tartrazine solution at a constant current density (50 mA·cm^{-2}). In saline solution, both the chemical and electrochemical processes occur much faster. Figure 4 shows the UV-Vis spectra of the electrolyzed tartrazine solution, recorded form 1 min. to 1 min..

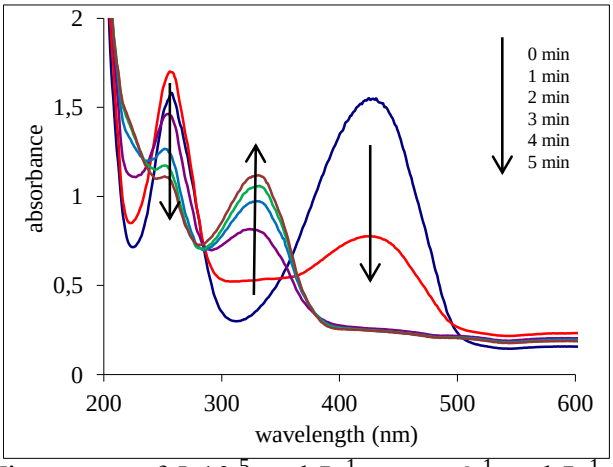

Figure 4: UV-Vis spectra of $5 \cdot 10^{-5}$ mol·L^{-1} TRZ, 10^{-1} mol·L^{-1} NaCl solution at different times of electrolysis.

The UV-Vis absorption spectra in the domain of high wavelengths (430 nm) indicate a rapid electrochemical degradation. After 2 minutes from the start of the electrolysis process, the maximum absorption wavelength corresponding to 430 nm disappears completely. The UV-Vis absorption spectra in the domain of low wavelengths (258 nm) indicate a more complex process. While the absorption maximum at 258 nm decreases, it is noted the appearance of a new peak at a wavelength of 332 nm, whose intensity increases with time. This indicates the formation of an intermediate species with an increasing concentration during the electrolysis process (absorbance values increase). In

saline solution, the UV-Vis spectra show the disappearance of the initial absorption peaks (258 nm and 430 nm) and the appearance of a new absorption peak (332 nm). As a conclusion, it can be said that, in the presence of chloride ions, occurs only a partial electrochemical degradation of the tartrazine molecule.

4. CONCLUSIONS

This study reports the application of electrochemical methods such as direct and indirect electrochemical degradation in removing the tartrazine, an azoic food additive, from salted aqueous solutions.

The method of constant current density electrolysis was used to investigate the effect of supporting electrolyte on tartrazine removal efficiency. The influence of supporting electrolyte was evaluated using spectrophotometric analysis. In the presence of sulfate anions the electrochemical degradation degree reaches a value of 37 % at 60 minutes of electrolysis, while in the presence of chloride anions the degradation degree reaches the maximum value of 100 % in just 2 minutes.

Experimental results indicate a total electrochemical degradation of the tartrazine molecules in the sodium sulfate solution, while in the sodium chloride solution only a partial electrochemical degradation occurs.

References

1. S. Kobylewski, M. F. Jacobson, J. Occup. Environ. Health., 18 (**2012**) 220.
2. M. A. Rauf, S. S. Ashraf, J. Hazard Mater., 166 (**2009**) 6.
3. A. Samide, B. Tutunaru, J. Therm. Anal. Calorim., 127 (**2017**) 863.
4. A. Samide, B. Tutunaru, J. Therm. Anal. Calorim., 127 (**2017**) 597.
5. B. Tutunaru, C. Tigae, C. Spînu, I. Prunaru, Int. J. Electrochem. Sci., 12 (**2017**) 396.
6. A. Samide, B. Tutunaru, C. Tigae, R. Efrem, A. Moanta, M. Dragoi, Environm. Protect. Eng., 2014 (**2014**) 93.
7. A. Samide, M. Dumitru, A. Ciuciu, B. Tutunaru, M. Preda, Stud Univ. Babes-Bolyai, Chemia, 4 (**2009**) 157.
8. A. Samide, G. E. Iacobescu, B. Tutunaru, C. Tigae, Int. J. Electrochem. Sci., 12 (**2017**) 2088.
9. A. Idris, M. S. Suhaimi, N. A. M. Zain, R. Rashid, N. Othman, Desalin. Water Treat., 52 (**2014**) 6694.
10. E. Z. Godlewska, W. Przystas, E. G. Sota, Water Air Soil Pollut., 225 (**2014**) 1.
11. Stephanie K. Meyer, Philip M.E. Probert, Anne F. Lakey, Andrew R. Axon, Alistair C. Leitch, Faith M. Williams, Paul A. Jowsey, Peter G. Blain, George E.N. Kass, Matthew C. Wright, Toxicol. Lett., 273 (**2017**) 55.

12. P. Mpountoukas, A. Pantazaki, E. Kostareli, P. Christodoulou, D. Kareli, S. Poliliou, C. Mourelatos, V. Lambropoulou, T. Lialiaris, Food Chem. Toxicol., 48 (**2010**) 2934.
13. L. Zhao, B. Zeng, F. Zhao, Electrochim. Acta, 146 (**2014**) 611.
14. Y. Zhang, X. Zhang, X. Lu, J. Yang, K. Wu, Food Chem., 122 (**2010**) 909.
15. P. S. Dorraji, F. Jalali, Food Chem., 227 (**2017**) 73.
16. W. R. P. Barros, S. A. Alves, P. C. Franco, J. R. Steter, R. S. Rocha, M. R. V. Lanza, J. Electroch. Soc., 161 (**2014**) H438.
17. Y. Zhang, L. Hu, X. Liu, B. Liu, K. Wu, Food Chem. 166 (**2015**) 352.
18. J. Zhang, M. Wang, C. Shentu, W. Wang, Z. Chen, Food Chem., 160 (**2014**) 11.
19. L. Monser, N. Adhoum, J. Hazard. Mater., 161 (**2009**) 263.
20. M. Soylak, Z. Topalak, J. Ind. Eng. Chem. 20 (**2014**) 581.
21. V. K. Gupta, R. Jain, A. Nayak, S. Agarwal, M. Shrivastava, Mat. Sci. Eng., C 31 (**2011**) 1062.
22. J. Goscianska, R. Pietrzak, Catalysis Today, 249 (**2015**) 259.
23. P. Oancea, V. Meltzer, J. Taiwan Inst. Chem. Eng., 44 (**2013**) 990.
24. A. Thiam, M. Zhou, E. Brillas, I. Sires, Appl. Catal. B: Environ., 150-151 (**2014**) 116.

Annals of the University of Craiova
The Chemistry Series
Volume XLIV, No. 1 (2017) 93-117
homepage: chimie.ucv.ro/anale/

Materials for solid oxide fuel cells

Review

Adriana Voinea[*]*, Andreea Simionescu, Alexandru Popescu*

University of Craiova, Faculty of Sciences, Department of Chemistry, Calea Bucuresti, 107i, Craiova, Romania
[*]E-mail: voineaadrianaa@yahoo.com

Received: 23.01.2017 / *Accepted*: 20.02.2017 / *Published*: 10.05.2017

Abstract
Solid-oxide fuel cells (SOFCs) present a particular interest due to their fuel flexibility, power generation efficiency, and low pollution. In order to achieve the best performance, the SOFC components must be compatible regarding thermal expansion, chemical interaction at their interfaces, electric and ionic conductivity and electrochemical performance. New electrode and electrolyte materials are developed during past decades. Research of new materials for SOFC components proved to be a major and challenging task. However, yttria stabilized zirconia, nickel cermet and lanthanum strontium manganite or lanthanum strontium cobaltite ferrite are the state-of-the-art materials for electrolyte, anode, and cathode, respectively. This work provides a review regarding the aspects related to material development.

Keywords: solid oxide; fue cell; materials

1. INTRODUCTION

The solid oxide fuel cells (SOFCs) are energy conversion devices that directly convert chemical energy of a fuel into electricity through a series of electrochemical reactions. They are delivering high electrical efficiency and significant environmental benefits in terms of fuel flexibility, as well as clean and efficient electric power generation [1, 2]. In addition, these fuel cells are

quiet, vibration-free and also produce no or very low levels of SO_x and NO_x emissions.

A SOFC consist in a dense electrolyte layer sandwiched between two porous electrodes (i.e., cathode and anode) as shown in Figure 1. The SOFC can use either an oxide ion conduction (Figure 1a) and/or proton conduction (Figure 1b) through the electrolyte. In principle, during operation the electrons generated in the oxidation process of fuel on anode travel through the external circuit to the cathode, where are involved in the oxygen reduction process. Since current is obtained via diffusion of oxide ions (or protons) through a solid electrolyte, it becomes imperative to use high operating temperatures (~800–1000^{o}C) for achieving high ionic conductivity (of ~0.1 S/cm) [1-7].

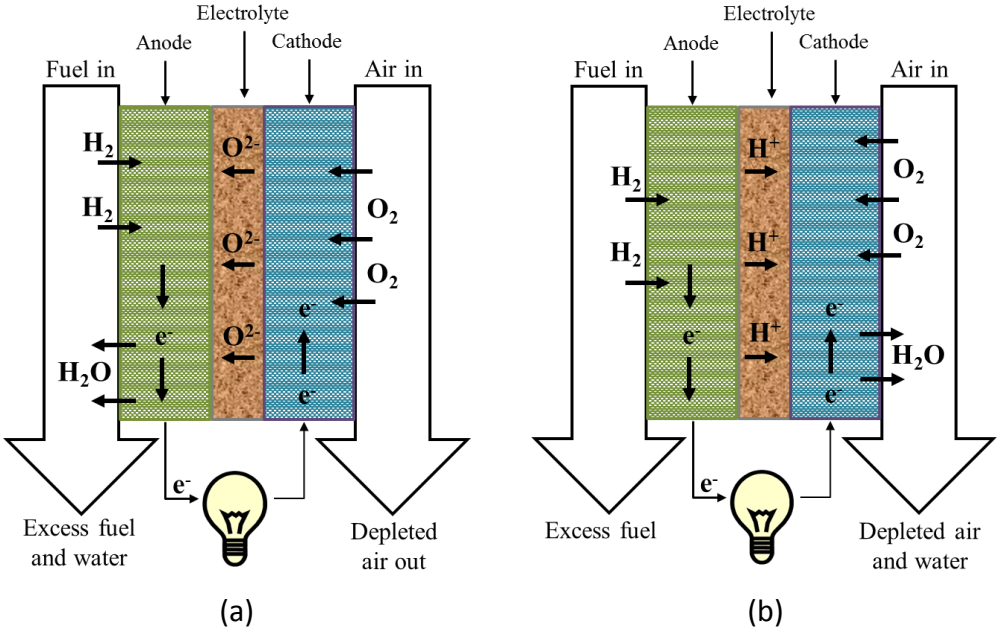

Figure 1. Schematic diagram of solid oxide fuel cell (SOFC) showing: a – oxide-ion conducting electrolyte, and b – proton conducting electrolyte during its operation. Adapted from: [8]

The most common SOFC are based on the standard materials: yttria stabilized zirconia for the electrolyte, $La_{(1-x)}Sr_xMnO_3$ for the cathode and Ni-cermets for the anode [9, 10]. These fuel cells operate at high temperatures (900-1000°C), due to the thermally activated processes running in electrodes and electrolyte. These high operation temperatures impose drastic requirements on cell components. The problems arising from long term operation at high temperatures are well-known: electrode sintering, catalyst poisoning, interfacial diffusion between electrolyte and electrode materials, thermal instability, and mechanical (or thermal) stresses due to differences in thermal expansion

behavior of the cell components. Such problems have limited the development and use of SOFCs to a greater extent.

To overcome these problems, new materials and processing technologies must be developed in order to decrease the operation temperature down to intermediate temperature range (500-700^{o}C).

2. ANODE

SOFC anode is the site of the fuel oxidation according to the following reaction:

$$H_2 + O^{2-} = H_2O + 2e^-$$

The main requirements for the anode are [11-17]:

- electrically conductive;
- high electrocatalytic activity;
- avoid coke deposition;
- large triple phase boundary;
- stable in a reducing environment;
- can be made thin enough to avoid mass transfer losses;
- able to provide mechanical support to electrolyte and cathode if the cell is anode supported;
- similar thermal expansion coefficient for neighboring cell component;
- chemically compatible with neighboring cell component;
- has a fine particle size;
- relatively inexpensive materials.

Conventionally, metals (or carbon) were both used as anode and cathode, which include graphite, platinum, iron, cobalt, and nickel. Due to low cost, good chemical stability and excellent catalytic activity towards hydrogen oxidation and reforming of hydrocarbon fuels, Ni had been used as an anode for several years. However, pure Ni has a considerable CTE mismatch with commonly used electrolyte material, such as, YSZ, which leads to weakening of its interface with the electrolyte material. While optimizing metal electrodes, cermets (i.e., ceramic–metallic composite e.g., Ni–YSZ) and metal oxides were introduced. Over the last few years, improvements in anode material properties have been addressed by selecting new materials [18].

2.1. Nickel-based anodes

Nickel metal anode

Ni electrodes were investigated as potential SOFC anode materials. Yamamura et al. [19] and Norby et al. [20] have reported patterned Ni anode and Ni mesh, respectively as a model anode to study the anodic reaction kinetics. Mizusaki et al. [21, 22] investigated the anode kinetics of the electrochemical oxidation reaction of H_2 on patterned Ni anodes with YSZ as electrolyte. Varying the P_{H_2} and P_{H_2O} in the anode feeds, Mizusaki et al. [23]

observed that the electrode interface conductivity is proportional to the length of TPB, and the rate of the electrode reaction is essentially determined by the reaction process on the Ni surface close to TPB.

Aaberg et al. [24] investigated Ni–YSZ point electrode using long-term potential step measurements and impedance spectroscopy and evidenced a redistribution of materials in the reaction zone (Ni and YSZ interface) on applying anodic overpotentials, which was attributed to the migration of Ni particles around the electrode-electrolyte interface. This was suggested to increase the length of TPB, which in turn enhances the electrode activity. According to Pizzini et al. [25], new catalytic sites are generated by such treatment, leading to an enhancement of anode activity.

Mizusaki et al. [22], Boer [26], and Bieberle et al. [27] studied anodic reaction mechanism on model anodes possessing well defined structures: metallic Ni thin films fabricated by photolithography and wet-chemical etching. At temperatures higher than 700^{o}C, Ni was found vulnerable to grain growth and coarsening [22]. The electrochemical performance of the anodes obtained by Bieberle et al. [27] was similar to that of Boer [26], but it differs from that reported by Mizusaki et al. [22] due to lower electrode conductivity. It is important to note that the TBP length was directly correlated with electrode conductivity [28].

Nickel/YSZ cermet anode

Ni–zirconia cermet anodes, which were first introduced by Liu et al. [29] in 1995, are the most used anode materials for SOFCs. Ordinarily, the thermal expansion of Ni mismatches that of stabilized zirconia at high temperatures [17]. However, Ni particles aggregate and reduce the porosity of an anode by eliminating the triple-phase boundary (TPB) required for cell operation, thereby decreasing cell performance. A pioneering research performed by the Westinghouse Electric Corporation developed Ni–YSZ cermet anodes to enhance the compatibility of thermal expansion coefficients between anodes and YSZ electrolytes. YSZ is electronically insulating; therefore, Ni phases in the cermet must be present in concentrations high enough to allow a complete conducting pathway through the anode. The percolation threshold, which is the common name of this parameter, has been studied in a number of systems. This characteristic normally occurs at approximately 30 vol% of the conducting phase. Studies on balancing thermal expansions and achieving sufficient conductivity have led to the development of anodes with Ni concentrations of 40-60 vol% [30].

One of the main disadvantages of Ni is the promotion of carbon formation. Anode specifications have changed as fuel requirements are increasingly focusing on hydrocarbon fuels with low steam ratios. Discussions on anode materials have highlighted direct oxidation of hydrocarbon fuels at the anode. Traditional Ni-based cermets are unsuitable in this process due to carbon

deposition. The usual method of producing Ni–YSZ cermets involves calcining mixed powders of NiO and YSZ to set up channels for ion conduction in YSZ. NiO is then reduced to Ni metal to achieve porosity. This material remains the most promising anode material for hydrogen conversion [31], but exhibits properties that are highly dependent on particle size, porosity, and microstructure of the final electrode [32, 33]. Anode porosity affects the fuel supply and reaction product removal in SOFCs.

Thus, despite its many advantages, the low sulfur tolerance and carbon deposition in Ni/YSZ composites lead to degradation in its performance. Thus there is a need to search alternative anode materials.

2.2. Copper and other noble metal cermets

New alternative composite anode materials such as Cu, Co, and phosphorous cermets are currently under evaluation [34]. Cu has been found inactive to carbon deposition [35] during the reformation of hydrocarbon fuels, such as CH_4 and syngas. However, Cu has a lower melting point (1083^oC) compared to Ni (1453^oC), and therefore, sintering at high temperatures is impractical. Instead, a new fabrication method, i.e., wet impregnation method was adopted to fabricate Cu based anodes [36-38]. Lu et al. [39] investigated impedance and current–voltage characteristics of SOFCs prepared with samaria doped ceria (SDC) as an electrolyte and anode based on either Cu-SDC or Au-SDC. The SOFCs were tested in H_2 and n-butane fuels at 650^oC. Similar performances were observed for both the cells based on Au-SDC and Cu-SDC, which suggest that both Au and Cu are acting solely as electronic conductors in the anode. This also leads to increase in activation polarization of the cell. One possible solution is to combine Cu with other materials exhibiting higher catalytic activity, such as ceria, to achieve enhanced activity and stability.

Ceria acts as an excellent oxidation catalyst, while Cu provides electronic conductivity to the anode. Kim et al. [40] fabricated and tested Cu–Ni alloys (with 0%, 10%, 20%, 50% and 100% Ni) as anode at 800^oC in dry CH_4. It was demonstrated that carbon deposit was greatly suppressed on the Cu–Ni alloys compared to that on pure Ni. Nevertheless, a significant increase in power density of cells based on Cu–Ni alloys was observed over time. This was attributed to an enhanced electronic conductivity of anode. Finally, authors suggested that the direct oxidation fuel cells based on Cu–Ni alloy cermet are feasible at 800^oC for CH_4.

Costa-Nunes et al. [35] compared the performance of SOFCs with Cu-CeO_2-YSZ composite anode to the SOFCs based on Ni–YSZ anodes operating under H_2, CO and syngas as fuel environments. Cu-CeO_2-YSZ were found to exhibit marked improvement in the anode performance compared to Ni-YSZ anode. Authors also explored the role of cobalt (Co) addition in Cu-CeO_2-YSZ cermet [35]. A significant enhancement in catalytic activity of Co-Cu-CeO_2-YSZ cermet was found in CO fuel compared with that in H_2 at 700^oC.x

2.3. Oxide Anodes

Compared with a metallic nickel catalyst, oxide catalysts show much higher coking resistance due to their different electronic structures. In addition, many oxide materials also show much higher redox stability than nickel. Thus, during the past decade, oxide-based anodes have also received considerable interest for use in SOFCs.

Fluorite Oxides

CeO_2 is a mixed ionic-electronic conductor in reducing atmospheres. It possesses higher electronic conductivity than YSZ (1 S/cm at 900^{o}C and P_{O_2} ~10^{-18} atm). Its ionic conductivity can be controlled by adding acceptor dopant oxides such as CaO, Y_2O_3, GdO_3, and Sm_2O_3 [41-46].

Doping CeO_2 with Sm_2O_3 (SDC) is however reported to slightly reduce the cell performance as well as catalytic activity (in spite of increasing conductivity) for direct electrochemical oxidation of butane [47]. Replacing YSZ in Ni– YSZ with ScSZ (scandia stabilized zirconia) and GDC (gadolinia doped ceria), i.e., Ni–ScSZ [48], and Ni–GDC [49-52], results in the enhancement in power outputs, with additional benefits in terms of sulfur tolerance.

A Mn-doped ceria–ScSZ anode for SOFCs operating on hydrogen and methane fuels has been reported [53]. It was found that the addition of Mn could remarkably decrease the sintering temperature of ceria, and the conductivity of ceria could also be improved with proper Mn doping in the fuel atmosphere.

Other elements, such as Mo, Zr and Fe, were used to dope ceria, and certain good results have been obtained [54-56]. Song et al. reported the creation of ceria–zirconia mixed oxides of $Ce_{1-x}Zr_xO_2$ (x = 0.1, 0.25, 0.5, 0.75, and 0.9, respectively, as anodes for SOFCs when hydrogen and methane were applied as fuels [54]. Lv et al. also reported $Ce_{1-x}Fe_xO_{2-\delta}$ (FDC, x = 0.1 and 0.2) anodes for methane-fueled SOFCs [56].

$Ce_{0.8}M_{0.2}O_{2-\delta}$ (M = Mn, Fe, Ni, Cu) was evaluated by Tu et al. for suitability as anodes for SOFCs running on hydrogen and methane [57]. It was found that $Ce_{0.8}M_{0.2}O_{2-\delta}$ have high coking resistance in a methane atmosphere. $Ce_{0.8}M_{0.2}O_{2-\delta}$ (M = Mn, Fe, Ni, Cu) presented relatively low electrochemical activity in both H_2 and CH_4.

Perovskite Oxides

With the aim to develop sulfur tolerant anode materials, oxides with perovskite structure were invented [58, 59], e.g., $Sr_{1-x}La_xTiO_3$ (LST; x = 0.3–0.4) [60, 61], Y-doped $SrTiO_3$ [62], $La_{1-x}Sr_xVO_3$ (LSV; x = 0.5) [63-68], $Ce_{0.9}Sr_{0.1}VO_x$ (x = 3,4) and its doped variations [69, 70], $La_{1-x}Sr_xCr_{1-y}Mn_yO_3$ (LSCM; x = 0.25, y = 0.5) [71], and double perovskite structured materials such

as $Sr_2Mg_{2-x}Mo_xO_6$ (SMMO; x =1) [72, 73], $Sr_2Fe_{4/3}Mo_{2/3}O_6$ [74], and pyrochlore structured $Gd_2Ti_{2-x}Mo_xO_7$ (x = 0.6) [75, 76]. Conductive oxides exibited improved sulfur tolerance, but lower electrical conductivity than Ni-cermet counterparts which leads to inferior anode performance [77], poor fuel oxidation, reduced catalytic activity, and incompatibility with the adjoining cell components during service at high temperatures.

Tao and Irvine reported $La_{1-x}Sr_xCr_{0.5}Mn_{0.5}O_{3-\delta}$ (LSCM) as a single-phase anode for SOFCs operating on H_2 and CH_4 [78]. This anode was stable in both reducing and oxidizing atmospheres and also showed good redox stability and operation stability in methane. The effects of the content and/or the variety of the LSCM dopants on the electric and electrocatalytic properties for high-performance SOFC anodes at reduced temperatures were studied [79, 80, 81]. Strontium was substituted by barium in LSCM, and the addition of Ba enhanced the electrical conductivity in air, whereas the conductivity in wet H_2 was well maintained compared with that of LSCM [79].

$SrTiO_3$ presents high chemical stability under air and fuel atmospheres and also has a high resistance toward carbon deposition and a high sulfur tolerance. Doping of the A and B sites of $SrTiO_3$ was also extensively exploited to make it applicable as anodes of SOFCs. For example, A-site La-doped $SrTiO_3$ (LST) perovskite anodes are attractive due to their high electronic conductivity and high dimensional and chemical stability in repeated redox cycling [61, 82].

3. ELECTROLYTE

The electrolyte conducts oxide ions from cathode to anode where it reacts with hydrocarbons to form H_2O and CO, and thus completes the overall electrochemical reaction. The oxide ion conduction occurs via oxygen vacancy hopping mechanism, which is a thermally activated process. For achieving a high ionic conductivity in electrolyte materials, their crystal structure must possess large interionic open space that allows high level of point defect disorder, and low migration enthalpy $\leq$1 eV [83].

The main requirements for the electrolyte are [84-86]:

- ionically conductive (should be characterized by oxygen ion transport numbers close to 1);
- electronically insulating;
- chemically stable at high temperatures;
- chemically stable in reducing and oxidizing environments;
- gas tight/free of porosity;
- production as a uniformly thin layer (to minimize ohmic losses);
- thermal expansion that matches electrodes;
- inexpensive materials.

The large number of oxygen ion electrolytes that have been investigated can be grouped into a small number of structure types: fluorite-based systems (doped bismuth oxide, zirconia, ceria, pyrochlore); [87] perovskite and related intergrowth structures (lanthanum gallate, brownmillerites, BiMeVOX); [88] LaMOX and apatites.

3.1. Fluorite based electrolytes

Y_2O_3 stabilized ZrO_2 (YSZ) materials were first recognized by Nernst in 1890s as a potential electrolyte owing to their high oxide ion conductivity. The mechanism of ionic conduction in YSZ is similar to that of acceptor doped CeO_2. Thus, the oxygen vacancies generated by adding acceptor dopant cation not only stabilizes the cubic phase of ZrO_2, but also enhances its oxide ion conductivity [89]. Among the various Y_2O_3–ZrO_2 solid solutions, 8 mol % Y_2O_3–ZrO_2 (8YSZ) is reported to exhibit highest ionic conductivity of 0.1 S/cm at 1000^oC, which is a minimum ionic conductivity required for an electrolyte [90].

Among other doped ZrO_2 systems, Sc_2O_3 doped ZrO_2 (ScSZ) materials have received considerable interest for SOFC electrolyte. At 850^oC, the ionic conductivity of 11 mol % Sc_2O_3 doped ZrO_2 is roughly 1.5 times higher than that of 8YSZ [91]. With high ionic transference (and negligible electronic conductivity) over a wide operation temperature range and partial pressures of oxygen, and good thermochemical properties, they offer an advantage of lowering the working temperature of SOFCs to intermediate temperature range. However, ScSZ suffers phase transitions as a function of temperature, conductivity ageing behavior over time at high temperatures, poor accessibility. Moreover, it has a quit high market price [92].

The high temperature fluorite structure of bismuth oxide polymorph (δ-Bi_2O_3) exhibits high intrinsic oxygen vacancies concentration (25% of the oxygen sublattice sites) [93], which leads to a remarkably high ionic conductivity in δ-Bi_2O_3. In fact, the ionic conductivity of δ-Bi_2O_3 is highest among all the studied oxide ion conductors. However, these materials undergoes a phase transformation from cubic (δ) to poorly conducting monoclinic (α) phase on cooling below 600^oC, which results in concomitant drop in the ionic conductivity. Furthermore, bismuth-oxide has structural stability issues in fuel environments (700^oC), and it possess low bending strength and toughness [93].

In order to enhance the oxide ion conductivity, numerous compositions based on CeO_2 have been explored. Acceptor dopants such as trivalent lanthanide cations, and divalent alkaline earth cations, were extensively used with varying doping level to understand the correlation between the physical properties of dopant and conductivity. Doping CeO_2 with lanthanide cations exhibit improved performance in the intermediate temperature range [94-97]. According to Kharton et al. [83] doped ceria materials exhibit higher ionic

conductivity than YSZ, so they can be utilized in the intermediate temperatures. In this category, solid solutions, such as, $Ce_{1-x}M_xO_{2-\delta}$ (where, M = Gd or Sm, x = 0.10–0.20) show the highest level of oxide ion transport [83]. Doped CeO_2 is relatively chemically inert towards electrode materials and renders high power density (~400mW/cm^2) at intermediate temperatures [98-103]. Gd- and Sm-doped ceria are generally recognized as the best conductors. Excellent conductivity has been observed in yttria-doped ceria [104]. Several co-doped ceria electrolytes have been investigated, for example, $Ce_{0.85}Gd_{0.1}Mg_{0.05}O_{1.9}$ [105], $Ce_{1-a}Gd_{a-y}Sm_yO_{2-0.5a}$ [106], $Ce_{1-x-y}Gd_xPrO_{2-z}$ [107], $Ce_{0.8}Sm_{0.2-x}Y_{x}O_{1.9}$ [108] and $Ce_{0.8}Gd_{0.2-x}Y_x$ [109] with some positive results.

3.2. Pyrochlores based electrolytes

Materials possessing pyrochlore structure (a superstructure of fluorite structure (AX_2)) with a general formula of $A_2B_2O_7$ have been actively investigated for ionic conduction since 1960 [110-114]. The oxide ion conductivity exhibited by pyrochlore based oxides (e.g., $Gd_2Zr_2O_7$ ~ 5x10^{-2} S/cm) is comparable to that of YSZ at 1000^{o}C. The ionic conduction in these materials can be tailored either by chemical substitution [115] or thermal treatment [114]; e.g., substituting Zr^{4+} for Ti^{4+} in $Gd_2(Ti_{1-x}Zr_x)_2O_7$ from $Gd_2(Zr_{0.3}Ti_{0.7})_2O_7$ to $Gd_2Zr_2O_7$ results in conductivity enhancement by two orders of magnitude [116]. Among various pyrochlore compositions, $Gd_{2-x}Ca_xTi_2O_{7-\delta}$ (x = 0.20) is reported to exhibits the highest conductivity [115,117]. Substitution of Gd^{3+} with Ca^{2+} in $Gd_2Ti_2O_{7-\delta}$ increases the *p*-type conductivity and lowers the *n*-type electronic conductivity of the material [117]. However, electron transference number of $(Gd,Ca)_2Ti_2O_{7-\delta}$ in air is reported to be on the higher side of acceptable values for solid electrolytes. In addition, few compositions in this category also possess ionic transference number lower than stabilized ZrO_2. These pyrochlore materials are most likely to find application as protective films on $LaGaO_2$- or CeO_2-based electrolytes. Furthermore, with a moderate CTE (~10.4–10.8x10^{-6}/K), these materials possess good compatibility with other cell components [83].

3.3. Perovskite based electrolytes

Perovskite type oxides with the chemical formula ABO_3 were investigated as ionic conductors by various groups [118, 119]. They exhibit exceptionally high ionic conductivity, better than most of the other oxide ion conductors [83].

Addition of acceptor dopant cation to $LaBO_3$ oxides, such as, Sr^{2+}, Ca^{2+},Mg^{2+} or Ba^{2+} at La^{3+} sites have been reported to enhance the catalytic activity and ionic conductivity [120-125]. The reduction of effective valence at A-site, creates oxygen vacancies, which, in turn, increase the ionic conductivity. Doping with Sr^{2+} results in the highest ionic conductivity as the tendency towards the formation of pair cluster is low, except for $LaCoO_3$ [126]. In case

of $La_{1-x}Sr_xGa_{1-y}Mg_yO_{3-\delta}$ (LSGM) series, maximum ionic transport have been observed for compositions with x and y lying in the range of 0.10–0.20 and 0.15–0.20, respectively [127]. Furthermore, it has been reported that replacing Ga^{3+} with Co^{3+} will result in an increase in ionic conductivity. However, this will also slightly increase the electronic conductivity in the material [128, 129]. Perovskite aluminates, such as, $LaAlO_3$ were extensively investigated since 1970s [127, 130-132]. Compared to $LaGaO_{3-\delta}$ and $CeO_{2-\delta}$, perovskites based on $LnBO_3$ (B = Al, In, Sc and Y) exhibit better stability to reduction and volatilization. Doping with Sr^{2+} at A-site has been shown to provide maximum enhancement in the conductivity and minimum vacancy-association.

Among various Sr^{2+} doped $LaGaO_3$ compositions, the maximum conductivity value has been reported in the case of $La_{0.9}Sr_{0.1}AlO_{3-\delta}$ [133-135]. Although, adding Mg^{2+} on B-site increases the oxygen vacancy concentration, however, it has a negative effect on the oxygen vacancy mobility which leads to lower ionic conductivity [136].

Brownmillerite-like phases

Oxides having a brownmillerite structure (with chemical formula of $A_2B_2O_5$) consist in alternating layers of perovskite [137]. The brownmillerites exhibit different types of electrical conduction, viz., in dry atmosphere and moderate P_{O_2}, it is typically ionic (oxide ion conductivity). Under oxidizing conditions, they exhibit mixed ionic and *p*-type electronic conduction, whereas in H_2O containing gas mixtures, they exhibits protonic conduction.

$Ba_2In_2O_5$ exhibits mixed conductivity, with oxide ion conductivity dominating the total conductivity in dry air. The rise in temperature causes a phase transition to a disordered perovskite phase at 930^{o}C that results in a significant increase in the ionic conduction [138]. The disordered cubic perovskite phase can be stabilized by substituting In-sites with higher-valance cations, e.g., Zr^{4+}, Ce^{4+}, Sn^{4+} or Hf^{4+} that can enhance intermediate temperature ionic conduction [139]. Doping with other cations, such as, Y^{3+}, Yb^{3+}, Ga^{3+} and Sc^{3+} at In-sites, i.e., $Ba_2In_{2-x}M_xO_5$, where x = 0.1–0.2 have also been investigated [140-142].

3.4. $La_2Mo_2O_9$ (LAMOX) based electrolyte materials

Materials based on $La_2Mo_2O_9$ compound or LAMOX, first reported by Lacorre et al. in 2000, exhibit fast oxide ion conducting property [143-145]. The oxide ion conductivity in LAMOX was found to be ~ $6x10^{-2}$ S/cm which compares well with that of stabilized ZrO_2 at 800^{o}C. These materials undergo a phase transition from room temperature monoclinic (α-form) to cubic (β-form) at around 580^{o}C, accompanied by a sudden increase in conductivity (by 2 orders of magnitude), which is similar to that observed for Bi_2O_3 and $Ba_2In_2O_5$ oxide ion conducting oxides. Due to their susceptibility towards phase transition and the tendency of molybdenum to get reduced in fuel environment,

researchers have investigated doping at both lanthanum and molybdenum sites. The effect of substitution of lanthanum site with other elements such as Nd, Y and Gd on suppressing the cubic to monoclinic phase transition on cooling have been investigated by Georges et al. [146]. On doping with Nd, phase remains monoclinic in the entire compositional range. However, above a certain dopant level, doping with Gd and Y leads to stabilization of cubic phase at room temperature. Doping with W to form $La_2Mo_{2-x}W_xO_9$ solid solutions (with $x \leq 1.6$) were reported to exhibit ionic conductivity of ~ 0.11 S cm^{-1} (x = 0) to 0.05 S cm^{-1} (x = 1.5) at 750°C, which compares well with that of gadolinium doped ceria [147].

Both ionic and electronic conductivity of $La_2Mo_2O_9$ as a function of temperature was explored by Subasri et al. [148]. It was reported that the phase transition, although present in $La_2Mo_2O_9$, does not have any apparent effect on its conductivity. The total conductivity was observed to be ~3 orders of magnitude lower than that reported by Lacorre et al. [144]. Furthermore, at 900°C, this material exhibits an ionic conductivity of ~$8x10^{-5}$ S/cm which is significantly lower than that of YSZ at the same temperature. Also, there is an onset of high electronic conductivity even at the oxygen partial pressures of the order of 8 Pa. The reported work is in contradiction with the result reported by Lacorre et al. [144]. It was further suggested by Subasri et al. [148] that the high conductivity observed by Lacorre et al. [144] may be due to the presence of impurities in $La_2Mo_2O_9$ samples.

3.5. Apatite structure

Apatite based materials have a general formula of $A_{10}(MO_4)_6X_{2+\delta}$ (where A is a rare earth or alkaline earth cation or Pb, M is a p-block element, such as, Si, Ge, P or V and X is OH^-, O^{2-} or halides). Rare-earth apatite materials have relatively high oxide ion conductivity at moderate temperatures as well as at low oxygen partial pressures [149-151] and have been proposed as alternative solid electrolyte materials [152-154]. The most interesting aspect of the apatite conductors is that their conductivity involves interstitial oxide-ions [155-158].

Apatite-based oxide ion conductors typically consists of $Ln_{9.33+x}(Si/GeO_4)_6O_{2+3x/2}$. On examining and modeling the probable conduction mechanism in apatites silicates, the atomistic simulation results suggest that conduction in $La_{9.33}(SiO_4)_6O_2$ and $La_8Sr_2(SiO_4)_6O_2$ takes place via interstitial and vacancy mechanism, respectively [155,157]. It has been shown that $La_{9.33}(SiO_4)_6O_2$ exhibits significantly higher ionic conductivity compared to that of $La_8Sr_2(SiO_4)_6O_2$ [159]. The key difference between the two samples is the presence of lanthanum vacancies in the $La_{9.33}Si_6O_{26}$ sample, although the oxide ion content is the same and nominally stoichiometric in both samples. Using neutron diffraction investigation in both the compositions, Sansom et al. [159] have shown that channel oxide ion are ordered in $La_8Sr_2(SiO_4)_6O_2$ composition,

while a degree of disorder is present in the case of $La_{9.33}(SiO_4)_6O_2$, where a significant portion of the channel oxygen is displaced into interstitial sites.

Among several reported rare earth apatites, lanthanum silicates exhibit ionic conductivity higher than their germinate counterparts [160-165]. The conductivity obtained is purely ionic as most of the compositions exhibit ionic transference number >0.9, across a wide range of P_{O2}. Initial investigations carried out by Nakayama et al. [152, 153] on an undoped $Ln_{10}(SiO_4)_6O_3$ revealed that the high oxide ion conductivity was observed for larger rare earths cations such as La, Pr, and Nd.

Moreover, oxygen excess compositions (x > 0) were reported to exhibit higher conductivity, e.g., at 500^{o}C, $La_{9.33}(SiO_4)_6O_2$ and $La_{9.67}(SiO_4)_6O_{2.5}$ exhibit ionic conductivity of $1.1x10^{-4}$ S/cm and $1.3x10^{-3}$ S/cm, respectively [161]. The results indicate that interstitial oxide ions also significantly contribute in enhancing the oxide ion conductivity in apatite systems. A wide range of compositions have been investigated in this category; however, majority of the work is focused on the La containing system, i.e., $La_{9.33+x}(SiO_4)_6O_{2+3x/2}$ [152, 153, 160, 161, 163, 165, 166, 167]. Various types of dopant were used: for La-site: Mg, Ca, Sr, Ba, Co, Ni, Cu, Mn, Bi and for Si-site: B, Al, Ga, Zn, Mg, Ti, Ge, Fe, Co, Ni, Cu, Mn, P. In addition, there are certain dopants which can easily occupy both La- and Si-sites (for example Mg^{2+}), and are termed as 'ambi-site' dopants [166].

Compared to silicates, germanate based apatites (or $La_{9.33+x}(GeO_4)_6O_{2+3x/2}$) have shown higher activation energy and hence, lower ionic conductivity at low temperatures [150]. In addition, germanate apatite materials show instability at high temperatures as they tend to volatilize, undergo glass formation, and show poor sinterability. The sinterability is reported to be improved by doping with transition metal cations. Furthermore, these materials have a tendency to incorporate significant amount of water molecules during annealing in wet atmospheres at temperatures below 500^{o}C, which probably contribute towards protonic conduction [168]. Their high ionic conductivity at higher temperatures looks promising.

3.6. Other oxides

$LaBaGaO_4$ compounds constitute another category of oxides containing isolated GaO_4 tetrahedral units which show significantly high ionic conductivity. The undoped phase of $LaBaGaO_4$ exhibits significantly lower conductivity than the doped phases. Li et al. [169] have measured the conductivity of $La_{1-x}Ba_{1+x}GaO_{4-x/2}$ in air and in N_2 atmospheres, and observed that the conductivity in N_2 atmosphere is lower than that in air, which suggests the existence of *p*-type conductivity in these materials.

$LaSrGa_3O_7$ - based materials represent another category of oxides that can be used as electrolytes for SOFCs [170]. In this category, $LaSrGa_3O_7$ is the parent compound which exhibits poor electrical conductivity. However, with an

increase in x value in $La_{1+x}Sr_{1-x}Ga_3O_{7+x/2}$, La/Sr concentration ratio is increased, resunlting in excess oxygen incorporation into the lattice to maintain the charge balance [171, 172].

4. CATHODE

The molecular oxygen supplied on the cathode side of SOFC is adsorbed onto the surface of the porous cathode, and is further reduced to oxide ions by accepting the incoming electrons from the current collector. Depending on the nature of the cathode material, oxygen reduction reaction can occur either on the electrode/gas interface or somewhere in the vicinity of the electrode/electrolyte/gas interface. The fully or partially reduced oxide ions or atomic species are then transported through the bulk or surface pathways to the electrolyte/electrode/gas interface where the complete reduction occurs. The oxide ions are subsequently transported to anode via diffusion through dense electrolyte [8].

The main requirements for SOFC cathode are [11, 37, 85, 86]:

- high electronic conductivity;
- chemically compatible with neighboring cell component (usually the electrolyte);
- can be made thin and porous;
- stable in an oxidizing environment;
- large triple phase boundary;
- catalyze the dissociation of oxygen;
- high ionic conductivity;
- adhesion to electrolyte surface;
- thermal expansion coefficient similar to other SOFC materials;
- relatively simple fabrication;
- relatively inexpensive materials.

Several classes of materials for cathode manufacture can be distinguished.

4.1. Noble-metal-based cathodes

Noble metals have been applied as cathodes in SOFCs for long time. However, their high price and low oxygen reduction activity at reduced temperatures and easy sintering at elevated temperatures make the pure phase noble metals impractical for use as cathodes in IT-SOFCs. Instead, the most studied noble-metal-based cathodes are composites created by mixing noble metals with a second ionic conductor. The use of composite cathodes improved the catalytic activity, lowered the electrode cost, and improved the morphological stability. Among the noble metals, silver and platinum are the two most popular electronic conductors, and they also show good chemical compatibility with the selected ionic conductors. The best performance is

usually obtained when the noble-metal phase and the ionic conducting phase are properly mixed.

The Ag and $Bi_2V_{0.9}Cu_{0.1}O_{5.35}$ (BVC) mixture is a well-known composite cathode due to its high electrocatalytic activity at reduced temperature and relatively low price compared with Pt. The Ag-BVC cathode was first reported by Xia et al. [173].

Camaratta et al. systematically investigated the long-term stability of a silver–bismuth oxide composite cathode [174, 175] and found that although the initial performances of silver- and yttrium-stabilized bismuth oxide (Ag-YSB) and silver- and erbium-stabilized bismuth oxide (Ag-ESB) were quite good, their polarization resistances isothermally increased by more than 70 % for Ag-YSB and by nearly 70 % for Ag-ESB, from 0.04 to 0.07 Ω cm^2 and from 0.06 to 0.10 Ω cm^2, respectively, after operation at 650°C for 100 h. Yang et al. replaced silver with gold as the electronic conducting phase in Ag-BVC, and a core-shell-nanostructured Au-BVC cathode was developed [176] that showed activity comparable to that of the Ag-BVC electrode.

4.2. Perovskite-based cathodes

Perovskites are of particular interest for SOFC cathodes. Perovskites are oxides with general formula ABO_3 (e.g., $LaMnO_3$, $LaCoO_3$, $LaFeO_3$). The A sites are occupied by lower valence cations, mainly of rare and alkaline earth metals, e.g., La, Sr, Ca, Ba, etc. The B-sites are occupied by higher valence reducible transition metal cations, e.g., Ti, Cr, Ni, Co, Fe, etc. [177].

In 1966, $La_{1-x}Sr_xCoO_{3-\delta}$ (LSC) was the first perovskite material reported by Button and Archer to be used as cathodes for SOFCs [178, 179]. This was followed by synthesis and testing of other several perovskite materials. From 1973, La_{1-x} $Sr_xMnO_{3-\delta}$ (LSM) was exclusively used for cathode manufacture, and it has remained the most investigated cathode material for SOFC [8].

The lanthanum strontium manganite ($La_{1-x}Sr_xMnO_3$) materials are still the most popular material for cathodes in current SOFCs operating at temperatures higher than 850 °C. This popularity is due to the good performance and structural stability of $La_{1-x}Sr_xMnO_3$, as well as the good chemical compatibility with the widely used YSZ electrolyte. Mizusaki et al. found that the electronic conductivity of $La_{1-x}Sr_xMnO_3$ increased monotonically as the content of Sr increased from x = 0 to x = 0.5, and this material showed a promising electronic conductivity that exceeded 100 S cm^{-1} [21, 22].

To enhance the electrochemical performance of $La_{1-x}Sr_xMnO_3$ at intermediate temperatures, the introduction of a second ionic conducting phase into the $La_{1-x}Sr_xMnO_3$ electrode is a simple and effective strategy. The most commonly used ionic conductor is YSZ electrolyte material. Tsai et al. systematically studied the effects of cathode composition, processing, and structure on the performance of a LSM–YSZ dual-phase composite electrode. It

was found that increasing the content of YSZ in the LSM–YSZ cathodes from 0 to 60 wt% reduced the low-current area-specific resistance of the cells (in air and humidified hydrogen) from ~3.3 to 0.7 Ω cm^2 at 750 °C [180]. Murray et al. reported that at 700 °C, the polarization resistance decreased from 7.82 Ω cm 2 for a pristine LSM cathode to 0.75 Ω cm 2 for a LSM–GDC composite cathode [181].

B-site doping is also widely applied to tailor the properties of LSM, and many transition metals (Sc, Cr, Fe, Co, Ni, and Cu) have been tested as dopants. Yue et al. prepared a scandium-doped $La_{0.8}Sr_{0.2}MnO_3$ cathode ($La_{0.8}Sr_{0.2}Mn_{1-x}Sc_xO3$ (LSMS)) [182]. Sc-doped LSMS cathodes exhibited higher performance, especially at lower temperatures. By partial substitution of the Mn in LSM with cobalt, the as-obtained cobalt-based materials exhibited greatly improved electrochemical performance compared with LSM [183].

$Ln_{1-x}Sr_xCoO_3$ is another popular electrode material for IT-SOFCs due to its superior oxygen reduction activity and can be treated as a material derived from the full substitution of Mn in the $Ln_{1-x}Sr_xMnO_3$ perovskite lattice. Ishihara examined the electrochemical activity of $Sm_{0.7}M_{0.3}CoO_3$ (M = Ca, Sr, Ba), and the maximum power density was obtained from the cell with Sr-doped $SmCoO_3$ [184]. However, the high content of Co in the B site of the perovskite resulted in a somewhat unstable phase structure, a higher TEC compared with other electrolyte materials, and a serious phase interaction between the electrode and electrolyte [185, 186].

$LaNiO_3$- based perovskite oxides are another series of popular electrode materials in SOFCs [187]. The pristine $LaNiO_3$ easily decomposes at elevated temperatures to form a catalytically inert NiO phase [188]. To avoid such phase decomposition, foreign ions were tested for partial substitution of the Ni in the B site. Chiba et al. doped several elements, including Al, Cr, Mn, Fe, Co, and Ga, into $LaNiO_3$ and found that Fe was the best candidate (LNF) [189, 190]. This material exhibited a high tolerance to Cr contamination. Komatsu et al. performed three separate stability tests of single cells with LSCF, LSM, and LNF as cathodes [191]. The LNF cathode maintained a stable cathodic overvoltage for ~150 h, whereas the overvoltages of cells with LSCF and LSM cathodes in the presence of the Cr-contained alloy were steeply increased. Other researchers tested cobalt and Mo doping as a strategy for electrochemical performance improvement of the $LaNiO_3$ electrode [192-194]. In addition to B-site doping, praseodymium was demonstrated as a proper substitution element for lanthanum in perovskite oxides to improve the performance of $LaNiO_3$ as an oxygen reduction electrode [195-198]. The substitution of La by Pr in $LaNiO_3$ might help to mediate the reactivity of the electrode with the YSZ electrolyte.

4.3. Layered perovskite-based cathodes

A-site cation-ordered double perovskites

A-site cation-ordered double perovskite oxides have the general formula $AA'B_2O_5$, where A′ = Ba, A = Y or a trivalent lanthanide ion, and B is a first row transition metal ion.

Taskin et al. [199] first found that A-site ordering in $Gd_{0.5}Ba_{0.5}MnO_3$ material could greatly enhance its oxygen diffusivity. For example, an ionic conductivity of 0.01 S cm^{-1} was achieved in cation-ordered $GdBaCo_2O_5$ at ~500 °C. It was proved that the oxygen transport in double perovskite occurred in a highly anisotropic direction and only in the A–O and adjacent B–O layers [200]. Later, Kim and Zhang et al. systematically investigated the application of $LnBaCo_2O_5$ materials (Ln = La, Pr, Nd, Sm, Gd, and Y) for SOFC cathodes [201, 202]. Chen et al. systematically studied the electrode performance of $PrBaCo_2O_5$ on a SDC electrolyte. $PrBaCo_2O_5$ and SDC showed good chemical compatibility because no serious reaction occurred between these two components, even at temperatures greater than 1000°C [203]. Doping of the B site of double perovskite with transition elements other than cobalt was also attempted. Zhao et al. prepared a series of Fe-doped $PrBaCo_2O_5$ materials [204]. In the case in which the B site is fully occupied with Fe, Chen et al. found that both $LaBaFe_2O_5$ and $PrBaCo_2O_5$ showed no A-site cation ordering, whereas $LnBaFe_2O_5$ (Ln = Nd, Sm and Gd) exhibited a cation-ordered double perovskite structure. As the ionic radius of the Ln^{3+} cation decreased from La to Y, the oxygen content, the average valence state of the iron ions, and the electronic conductivity in the nominal composition of $LnBaFe_2O_5$ were also reduced. The $YBaFe_2O_5$ material had the lowest TEC value of $14.6x10^{-6}$ K^{-1}. Among these materials, the $SmBaFe_2O_5$ electrode exhibited the best electrocatalytic activity for the oxygen reduction reaction (ORR).

B-site cation-ordered double perovskites

In the $A_2B'B''O_6$-type double perovskite structure, the arrangement of the B-cation sub-lattice is controlled by the charge difference and by the size difference relative to a given A site [205].

Deng et al. [206] prepared a single-phase double perovskite $Ba_2CoMo_{0.5}Nb_{0.5}O_{6-\delta}$ (BCMN) composition with a Mo and Nb co-doping structure, which showed high structural stability because no phase decomposition was observed after 240 h of calcination at 750°C. One drawback of $Ba_2CoMo_{0.5}Nb_{0.5}O_{6-\delta}$ materials might be their relative low electrical conductivity. More recently, a novel Bi and Sc co-doped $BaCoO_3$ was reported to possess a B-site cation-ordered double perovskite structure. This $Ba_2Bi_{0.1}Sc_{0.2}Co_{1.7}O_{6-\delta}$ (BBSC) material showed good catalytic activity between 600 and 750°C related to its large oxygen vacancy diffusion coefficient and surface exchange coefficient. Moreover, despite the existence of phase decomposition, the oxygen reduction activity of BBSC was proved to be stable

under cathodic polarization treatment, which is the normal cathode operating mode in SOFCs [207].

Another popular $A_2B'B''O_6$-type double perovskite is $Sr_2Fe_{1.5}Mo_{0.5}O_{6-\delta}$ (SFM), which was first used in symmetrical SOFCs [208]. SFM showed good chemical compatibility with traditional LSGM, SDC, and $BaZr_{0.1}Ce_{0.7}Y_{0.2}O_{3-\delta}$ (BZCY) electrolyte materials. This material also showed a low TEC of $14.5x10^{-6}$ K^{-1} in a temperature range of 200-760°C [209].

5. CONCLUSIONS

Considering that the solid oxide fuel cells are devices which promise to deliver high electrical efficiency, significant environmental benefits because of their fuel flexibility and clean and efficient electric power generation, continuing efforts to discover new materials for the SOFCs components that can improve the cells performances and enable their operating temperatures are made.

Development of electrolytes with low resistance at intermediate or low temperature, i.e., increasing the ion conductivity or/and decreasing the membrane thickness, remain the mainstreams of research in the field of SOFC electrolyte. Solid electrolyte materials have to be stable over a wide range of oxygen partial pressures and temperatures. Candidate materials for medium and low temperature operation (800-500^oC) have to be examined for invariant chemical composition and crystal structure as well as for mechanical stability and electrical properties. Researches in the field have lead to new oxide materials such as: ZrO_2, CeO_2, Bi_2O_3 based oxides with the fluorite structure, $LaGaO_3$ based perovskites, $Bi_4V_2O_{11}$ and $La_2Mo_2O_9$ based derivatives, $Ba_2In_2O_5$ derived perovskite, and brownmillerite like phases and pyrochlores, which have shown promising results. Doping with multiple valent elements is considered a promising approach to enhance conductivity up to several orders of magnitude, while interfacial conduction could also exert a dramatic impact on the total conductivity.

Electrode materials have to be well adjusted to the chosen electrolyte material in terms of chemical compatibility, thermal expansion coeficient and microstructure properties.

The design of anode requires enhanced triple phase boundaries (TPB: gas, electrolyte and anode), while minimizing coking or sulfur poisoning in order to enhance the efficiency of charge transfer. This class includes metals (Ni, Cu), cermets (Ni/Cu-YSZ), perovskites, and pyrochlores. It has been observed that the finer microstructure and lower sintering temperature result in enhancing the performance of anode. The ceria impregnated Ni–YSZ appears to be one of the high performing anodes as it possesses high melting point (1453^oC), and sustain resistance to enhanced sulfur poisoning (from hydrocarbon fuels).

Cathodes require gas-diffusion type porous electrodes, and their electrochemical kinetics is governed by over potential, and other factors such as geometry of active surfaces. Popular choice among cathode materials are perovskites owing to their high *p*-type electronic conductivity and high oxide ion conductivity under oxidizing atmospheres. Furthermore, the minimal mismatch in the CTE value with electrolyte, high permeability of oxygen molecules to cathode/ electrolyte interface and ease of processing porous structure make them a perfect choice. LSCF with a thin LSM coating appears to be one of the promising cathode materials. Further, it is also observed that the cathodic polarization can lead to enhancement in the cathodic activity as well.

References

1. T.S. Lee, J.N. Chung, Y.-C. Chen, *Energy Convers Manage*, 52 (**2011**) 3214.
2. A.B. Stambouli, E. Traversa, *Renew Sustain Energy Rev*, 6 (**2002**) 433.
3. N.Q. Minh, *Solid State Ionics*, 174 (**2004**) 271.
4. O. Yamamoto, *Electrochim Acta*, 45 (**2000**) 2423.
5. B.C.H. Steele, H. Heinzel, *Nature*, 414 (**2001**) 345.
6. S. Park, J.M. Vohs, R.J. Gorte, *Nature*, 404 (**2000**) 265.
7. T. Hibino, *Electrochem Solid-State Lett*, 5 (**2002**), A242.
8. N. Mahato, A. Banerjee, A. Gupta, S. Omar, K. Balani, *Progress in Materials Science*, 72 (**2015**) 141.
9. L.-W. Tai, M.M. Nasrallah, H.U. Anderson, D.M. Sparlin, S.R. Sehlin, *Solid State Ionics*, 76 (**1995**) 259.
10. C. Ftikos, S. Carter, B.C.H. Steele, J. Europ. *Ceram. Soc.*, 12 (**1993**) 79.
11. K.C. Wincewicz, J.S. Cooper, *Journal of Power Sources*, 140 (**2005**) 280.
12. S.P.S. Badwal, K. Foger, *Mater. Forum*, 21 (**1997**) 187.
13. E. Maguire, B. Gharbage, F.M.B. Marques, J.A. Labrincha, *Solid State Ionics*, 127 (**2000**) 329.
14. S.C. Singhal, *Solid State Ionics*, 135 (**2000**) 305.
15. X. Zhang, S. Ohara, R. Maric, K. Mukai, T. Fukui, H. Yoshida, M. Nishimura, T. Inagaki, K. Miura, *J. Power Sources*, 83 (**1999**) 170.
16. J. Morse, R. Graff, P. Hayes, A. Jankowski, *Mater. Res. Soc. Symp. Proc.*, 575 (**2000**) 321.
17. R. Gorte, S. Park, J. Vohs, C. Want, *Adv. Mater.*, 12 (**2000**) 1465.
18. R.M. Ormerod, *Chem. Soc. Rev.*, 32 (**2003**) 17.
19. T. Yamamura, H. Tagawa, T. Saito, J. Mizusaki, K. Kamitani, K. Hirano, et al., 4th International symposium on solid oxide fuel cells. *The Electrochemical Society*, (**1995**) 741.
20. T. Norby, O.J. Velle, H. Leth-Olsen, R. Tunold, 3rd International symposium on solid oxide fuel cells. *The Electrochemical Society*, (**1993**) 473.

21. J. Mizusaki, H. Tagawa, T. Saito, K. Kamitani, T. Yamamura, K. Hirano, et al., *J. Electrochem. Soc.*, 414 (**1994**) 2129.
22. J. Mizusaki, H. Tagawa, T. Saito, T. Yamamura, K. Kamitani, K. Hirano, et al., *Solid State Ionics*, 70/71 (**1994**) 52.
23. J. Mizusaki, H. Tagawa, T. Saito, T. Yamamura, K. Kamitani, K. Hirano, et al., 3rd International symposium on solid oxide fuel cells. *The Electrochemical Society*, (**1993**) 533.
24. R.J. Aaberg, R. Tunold, M. Mogensen, R.W. Berg, R. Odegrd, *J. Electrochem. Soc.*, 145 (**1998**) 2244.
25. S. Pizzini, M. Bianchi, P. Colombo, S. Torchio, *J. Appl. Electrochem.*, 3 (**1973**) 153.
26. B. Boer, *Ph.D. Thesis.* Twente: University of Twente, (**1998**).
27. A. Bieberle, L.P. Meier, L.J. Gauckler, *J. Electrochem. Soc.*, 148 (**2001**) A646.
28. D. Beckel, A. Bieberle, A. Hütter, A. Harvey, A. Infortuna, U.P. Muecke, M. Prestat, et al., *J. Power Sour.*, 2007 (**2007**) 325.
29. W. Liu, M. Flytzani-Stephanopoulos, *J. Catal.*, 153 (**1995**) 304.
30. G. Pudmich, B. Boukamp, M. Gonzalez-Cuenca, W. Jungen, W. Zipprich, F. Tietz, *Solid. State. Ion.*, 135 (**2000**) 433.
31. E. Tsipis, V. Kharton, J. Frade, *J. Eur. Ceram. Soc.*, 25 (**2005**) 2623.
32. K. El Adham, A. Hammou, *Solid State Ion.*, 9 (**1983**) 905.
33. G.B. Balazs, R.S. Glass, *Solid State Ion.*, 76 (**1995**) 155.
34. Singhal S. *High-temperature solid oxide fuel cells: fundamentals, design and applications.* Elsevier, (**2003**).
35. O. Costa-Nunes, R.J. Gorte, J.M. Vohs, *J. Power Sour.*, 141 (**2005**) 241.
36. R.J. Gorte, J.M. Vohs, S. McIntosh, *Solid State Ionics*, 175 (**2004**) 1.
37. R.J. Gorte, S. Park, J.M. Vohs, Wang C., *Adv. Mater.*, 12 (**2000**) 1465.
38. H. Kim, J.M. Vohs, R.J. Gorte, *Chem. Commun.*, (**2001**) 2334.
39. C. Lu, W.L. Worrell, J.M. Vohs, R.J. Gorte, *J. Electrochem. Soc.*, 150 (**2003**) A1357.
40. H. Kim, C. Lu, W.L. Worrell, J.M. Vohs, R.J. Gorte, *J. Electrochem. Soc.*, 149 (**2002**) A247.
41. E.P. Murray, T. Tsai, S.A. Barnett, *Nature*, 400 (**1999**) 649.
42. H. Yokokawa, T. Horita, N. Sakai, K. Yamaji, M.E. Brito, Y.P. Xiong, et al., *Solid State Ionics*, 174 (**2004**) 205.
43. B.C.H. Steele, *Solid State Ionics*, 129 (**2000**) 95.
44. S. Omar, E.D. Wachsman, J.L. Jones, J.C. Nino, *J. Am. Ceram. Soc.*, 92 (**2009**) 2674.
45. S. Omar, E.D. Wachsman, J.C. Nino, *Solid State Ionics*, 177 (**2006**) 3199.
46. S. Omar, E.D. Wachsman, J.C. Nino, *Appl. Phys. Lett.*, 91 (**2007**) 1441.
47. S. McIntosh, J.M. Vohs, R.J. Gorte, *Electrochim. Acta.*, 47 (**2002**) 3815.
48. K. Sasaki, K. Susuki, A. Iyoshi, M. Uchimura, N. Imamura, H. Kusaba, et al., *J. Electrochem. Soc.*, 153 (**2006**) A2023.

49. J.P. Trembly, A.I. Marquez, T.R. Ohrn, D.J. Bayless, *J. Power. Sour.*, 158 (**2006**) 263.
50. L. Zhang, S.P. Jiang, H.Q. He, X. Chen, J. Ma, X.C. Song, *Int. J. Hydro. Energy*, 35 (**2010**) 12359.
51. P.V. Aravind, J.P. Ouweltjes, N. Woudstra, G. Rietveld, *Electrochem. Solid State Lett.*, 11 (**2008**) B24.
52. J.P. Ouweltjes, P.V. Aravind, N. Woudstra, G. Rietveld, *J. Fuel Cell Sci. Technol*., 3 (**2006**) 495.
53. G. Cai, R. Liu, C. Zhao, J. Li, S. Wang, T. Wen, *J. Solid State Electrochem*., 15 (**2011**) 147.
54. S. Song, R. Fuentes, R. Baker, *J. Mater. Chem*., 20 (**2010**) 9760.
55. K. Ahn, H. He, J. Vohs, R. Gorte, *Electrochem. Solid-State Lett.*, 8 (**2005**) A414.
56. H. Lv, D. Yang, X. Pan, J. Zheng, C. Zhang, W. Zhou, J. Ma, K. Hu, *Mater. Res. Bull*., 44 (**2009**) 1244.
57. H. Tu, H. Lv, Q. Yu, K. Hu, X. Zhu, *J. Fuel Cell. Sci. Technol*., 5 (**2008**) 031203.
58. M. Gong, X. Liu, J. Trembly, C. Johnson, *J. Power. Sour*., 168 (**2007**) 289.
59. C. Sun, U. Stimming, *J. Power. Sour*., 171 (**2007**) 247.
60. R. Mukundan, E.L. Brosha, F.H. Garzon, *Electrochem. Solid-State Lett*., 7 (**2004**) A5.
61. O.A. Marina, N.L. Canfield, J.W. Stevenson, *Solid State Ionics*, 149 (**2002**) 21.
62. H. Kurokawa, L. Yang, C.P. Jacobson, L.C.D. Jonghe, S.J. Visco, *J. Power Sour*., 164 (**2007**) 510.
63. L. Aguilar, S.W. Zha, Z. Cheng, J. Winnick, M.L. Liu, *J. Power Sour*., 135 (**2004**) 17.
64. Z. Cheng, S. Zha, L. Aguilar, D. Wang, J. Winnick, M. Liu, *Electrochem. Solid State Lett.*, 9 (**2006**) A31.
65. A. Burke, S. Li, J. Winnick, M. Liu, *J. Electrochem. Soc*., 151 (**2004**) D55.
66. L. Aguilar, S.W. Zha, S.W. Li, J. Winnick, M. Liu, *Electrochem. Solid-State Lett*., 7 (**2004**) A324.
67. Z. Cheng, S.W. Zha, L. Aguilar, M.L. Liu, *Solid State Ionics*, 176 (**2005**) 1921.
68. M. Cooper, K. Channa, R.D. Silva, D.J. Bayless, *J. Electrochem. Soc*., 157 (**2010**) B1713.
69. N. Danilovic, J.L. Luo, K.T. Chuang, A.R. Sanger, *J. Power. Sour*., 192 (**2009**) 247.
70. N. Danilovic, J.-L. Luo, K.T. Chuang, A.R. Sanger, *J. Power. Sour*., 194 (**2009**) 252.
71. S.W. Zha, P. Tsang, Z. Cheng, M.L. Liu, *J. Solid State Chem*., 178 (**2005**) 1844.
72. Y.H. Huang, R.I. Dass, Z.L. Xing, *J.B. Science*, 312 (**2006**) 254.

73. Y.H. Huang, R.I. Dass, J.C. Denyszyn, J.B. Goodenough, *J. Electrochem. Soc*., 153 (**2006**) A1266.
74. G. Xiao, Q. Liu, X. Dong, K. Huang, F. Chen, *J. Power. Sour*., 195 (**2010**) 8071.
75. S.W. Zha, Z. Cheng, M.L. Liu, *Electrochem. Solid-State Lett*., 8 (**2005**)A406.
76. S. Zha, Z. Cheng, M. Liu, *E.C.S. Trans*., 1 (**2006**) 293.
77. S. Wang, M. Liu, J. Winnick, J. *Solid State Electrochem*., 5 (**2001**) 188.
78. S. Tao, J. Irvine, *Nat. Mater*., 2 (**2003**) 320.
79. E. Lay, L. Dessemond, G. Gauthier, *J. Power Sources*, 221 (**2013**) 149.
80. E. Lay, G. Gauthier, S. Rosini, C. Savaniu, J. Irvine, *Solid State Ionics*, 179 (**2008**) 1562.
81. T. Jardiel, M.T. Caldes, F. Moser, J. Hamon, G. Gauthier, O. Joubert, *Solid State Ionics*, 181 (**2010**) 894.
82. X. Zhou, N. Yan, K. Chuang, J. Luo, *R.S.C. Adv*., 4 (**2014**) 118.
83. V.V. Kharton, F.M.B. Marques, A. Atkinson, *Solid State Ionics*, 174 (**2004**) 135.
84. S.P.S. Badwal, K. Foger, *Mater. Forum*, 21 (**1997**) 187.
85. E. Maguire, B. Gharbage, F.M.B. Marques, J.A. Labrincha, *Solid State Ionics*, 127 (**2000**) 329.
86. S.C. Singhal, *Solid State Ionics*, 135 (**2000**) 305.
87. P.K. Moon, H. Tuller, *Solid State Ionics*, 28-30 (**1988**) 470.
88. F. Abraham, J.C. Boivin, G. Mairesse, G. Nowogrocki, *Solid State Ionics*, 40-41 (**1990**) 934.
89. N.Q. Minh, *J. Am. Ceram. Soc*., 76 (**1993**) 563.
90. T.H. Etsell, S.N. Flengas, *Chem. Rev.*, 70 (**1970**) 339.
91. S.P.S. Badwal, F.T. Ciacchi, *Ionics*, 6 (**2000**) 1.
92. S. Omar, W.B. Najib, N. Bonanos, *Solid State Ionics*, 189 (**2011**) 100.
93. N. Jiang, E.D. Wachsman, *J. Am. Ceram. Soc*., 82 (**1999**) 3057.
94. H. Yahiro, K. Eguchi, H. Arai, *Solid State Ionics*, 36 (**1989**) 71.
95. H. Yahiro, Y. Eguchi, K. Eguchi, H. Arai, *J. Appl. Electochem.*, 18 (**1988**) 527.
96. K. Eguchi, T. Setoguchi, T. Inoue, H. Arai, *Solid State Ionics*, 52 (**1992**) 165.
97. Y. Arachi, H. Sakai, O. Yamamoto, Y. Takeda, N. Imanishai , *Solid State Ionics*, 12 (**1999**) 133.
98. J. Liu, B.D. Madsen, Z. Ji, S.A. Barnett, *Electrochem. Solid-State Lett*., 5–6 (**2002**) A122.
99. C. Xia, M. Liu., *J. Am. Ceram. Soc*., 84 (**2001**) 1903.
100. K. Prabhakaran, M.O. Beigh, J. Lakra, N.M. Gokhale, S.C. Sharma, *J. Mater. Process Technol*., 189 (**2007**) 178.
101. Y.Z. Jiang, J.F. Gao, M.F. Liu, Y.Y.Wang, G.Y. Meng, *Solid State Ionics*, 177 (**2007**) 3405.

102. C. Brahim, A. Ringuede, M. Cassir, M. Putkonen, L. Niinisto, *Appl. Surf. Sci*., 253 (**2007**) 3962.
103. T.S. Zhang, J. Ma, H. Cheng, S.H. Chan, *Mater. Res. Bullet*., 41 (**2006**) 563.
104. J. Van Herle, T. Horita, T. Kawada, N. Sakai, H. Yokokawa, M. Dokiya, *J. Eur. Ceram. Soc*., 16 (**1996**) 961.
105. F. Wang, S. Chen, Q. Wang, S. Yu, S. Cheng, *Catal.Today*, 97 (**2004**) 189.
106. F.Y. Wang, S.Y. Chen, S. Cheng, *Electrochem. Commun*., 6 (**2004**) 743.
107. S. Lubke, H.D. Wiemhofer, *Solid State Ionics*, 117 (**1999**) 229.
108. X.Q. Sha, Z. Lu, X.Q. Huang, J.P. Miao, L.J. Jia, *Alloys Compd*., 424 (**2006**) 315.
109. X. Guan, H. Zhou, Y. Wang, J.J. Zhang, *Alloys Compd*., 464 (**2008**) 310.
110. M. Mori, G.M. Tompsett, N.M. Sammes, E. Suda, Y. Takeda, *Solid State Ionics*, 158 (**2003**) 79.
111. V.V. Kharton, E.V. Tsipis, A.A. Yaremchenko, N.P. Vyshatko, A.L. Shaula, E.N. Naumovich, et al., *J. Solid State Electrochem*., 7 (**2003**) 468.
112. M. Pirzada, R.W. Grimes, L. Minervini, J.F. Maguire, K.E. Sickafus, *Solid State Ionics*, 140 (**2001**) 201.
113. L. Minervini, R.W. Grimes, K.E. Sickafus, *J. Am. Ceram. Soc*., 83 (**2000**) 1873.
114. B.J. Wuensch, K.W. Eberman, *J. Min. Metals Mater. Soc*., 52 (**2000**) 19.
115. S.A. Kramer, H.L. Tuller, *Solid State Ionics*, 82 (**1995**) 15.
116. B.J. Wuensch, K.W. Eberman, C. Heremans, E.M. Ku, P. Onnerud, E.M.E. Yeo, et al., *Solid State Ionics*, 129 (**2000**) 111.
117. S. Kramer, M. Spears, H.L. Tuller, *Solid State Ionics*, 72 (**1994**) 59.
118. T. Ishihara, H. Matsuda, Y. Takita, *J. Am. Chem. Soc*., 116 (**1994**) 3801.
119. M. Feng, J.B. Goodenough, *Euro. Solid State Inorg. Chem*., T31 (**1994**) 663.
120. H.U. Anderson, *Solid State Ionics*, 52 (**1992**) 33.
121. N. Yamazoe, Y. Teraoka, *Catal. Today*, 8 (**1990**) 175.
122. J.G. McCarty, H. Wise, *Catal. Today*, 8 (**1990**) 231.
123. C.B. Alcock, J.J. Carberry, R. Doshi, N. Gunasekaran, *J. Catal*., 143 (**1993**) 533.
124. P. Salomonsson, T. Griffin, B. Kasemo, *Appl. Catal. A: Gen*., 104 (**1993**) 175.
125. P.E. Marti, A. Baiker, *Catal. Lett*., 26 (**1994**) 71.
126. M. Cherry, M.S. Islam, C.R.A. Catlow, *J. Solid State Chem*., 118 (**1995**) 125.
127. H. Hayashi, H. Inaba, M. Matsuyama, N.G. Lan, M. Dokiya, H. Tagawa, *Solid State Ionics*, 122 (**1999**) 1.
128. N. Trofimenko, H. Ullmann, *Solid State Ionics*, 118 (**1999**) 215.
129. V.V. Kharton, A.P. Viskup, A.A. Yaremchenko, R.T. Baker, B. Gharbage, G.C. Mather, et al., *Solid State Ionics*, 132 (**2000**) 119.

130. T. Takahashi, H. Iwahara, *Energy Conversion*, 11 (**1971**) 105.
131. J. Mizusaki, I. Yasuda, J.-I. Shimoyama, S. Yamauchi, K. Fueki, *J. Electrochem. Soc*., 140 (**1993**) 467.
132. T. Ishihara, H. Matsuda, Y. Takita, *J. Electrochem. Soc*., 141 (**1994**) 3444.
133. D. Lybye, F.W. Poulsen, M. Mogensen, *Solid State Ionics*, 128 (**2000**) 91.
134. K. Nomura, S. Tanase, *Solid State Ionics*, 98 (**1997**) 229.
135. T.L. Nguyen, M. Dokiya, S. Wang, H. Tagawa, T. Hashimoto, *Solid State Ionics*, 130 (**2000**) 229.
136. P.S. Anderson, F.M.B. Marques, D.C. Sinclair, A.R. West, *Solid State Ionics*, 118 (**1999**) 229.
137. J.D. Ferguson, Y. Kim, L.F. Kourkoutis, A. Vodnick, A.R. Woll, D.A. Muller, et al., *Adv. Mater*., 23 (**2011**) 1226.
138. J.B. Goodenough, J.E. Ruiz-Diaz, Y.S. Zhen, *Solid State Ionics*, 44 (**1990**) 21.
139. T. Schober, J. Friedrich, *Solid State Ionics*, 369 (**1998**) 113.
140. H. Yamamura, K. Yamazaki, K. Kakinuma, K. Nomura, *Solid State Ionics*, 150 (**2002**) 255.
141. T. Yao, Y. Uchimoto, M. Kinuhata, T. Inagaki, H. Yoshida, *Solid State Ionics*, 132 (**2000**) 189.
142. C.A.J. Fisher, B. Derby, R.J. Brook, *Brit. Ceram. Proc*., 56 (**1996**) 25.
143. P. Lacorre, *Solid State Sci*., 2 (**2000**) 755.
144. P. Lacorre, F. Goutenoire, O. Bohnke, R. Retoux, Y. Laligant, *Nature*, 404 (**2000**) 856.
145. F. Goutenoire, O. Isnard, R. Retoux, P. Lacorre, *Chem. Mater*., 12 (**2000**) 2575.
146. S. Georges, F. Goutenoire, F. Altorfer, D. Sheptyakov, F. Fauth, E. Suard, et al., *Solid State Ionics*, 161 (**2003**) 231.
147. D. Marrero-López, J. Peña-Martínez, J.C. Ruiz-Morales, D. Pérez-Colla, M.C. Martín-Sedeño, P. Núñez, *Solid State Ionics*, 178 (**2007**) 1366.
148. R. Subasri, H. Nafe, F. Aldinger, *Mater. Res. Bullet*., 38 (**2003**) 1965.
149. P.R. Slater, J.E.H. Sansom, J.R. Tolchard, *Chem. Rec*., 4 (**2004**) 373.
150. E. Kendrick, M.S. Islam, P.R. Slater, *J. Mater. Chem*., 17 (**2007**) 3104.
151. T. Iwata, E. Bechade, K. Fukuda, O. Masson, I. Julien, E. Champion, P.J. Thomas, *Am. Ceram. Soc*., 91 (**2008**) 3714.
152. S. Nakayama, H. Aono, Y. Sadaokac, *Chem. Lett*., 6 (**1995**) 431.
153. S. Nakayama, T. Kageyama, H. Aono, Y. Sadaokac, *J. Mater. Chem*., 5 (**1995**) 1801.
154. S. Nakayama, M. Sakamoto, M. Higuchi, K. Kodaira, M. Sato, S. Kakita, T. Suzuki, K. Itoh, *J. Eur. Ceram. Soc*., 19 (**1999**) 507.
155. M.S. Islam, J.R. Tolchard, P.R. Slater, *Chem. Commun*., (**2003**) 1486.
156. E. Bechade, O. Masson, T. Iwata, I. Julien, K. Fukuda, P. Thomas, E. Champion, *Chem. Mater*., 21 (**2009**) 2508.
157. J.R. Tolchard, M.S. Islam, P.R. Slater, *J. Mater. Chem*., 13 (**2003**) 1956.

158. A. Jones, P.R. Slater, M.S. Islam, *Chem. Mater*., 20 (**2008**) 5055.
159. J.E.H. Sansom, D. Richings, P.R. Slater, *Solid State Ionics*, 139 (**2001**) 205.
160. H. Yoshioka, S. Tanase, *Solid State Ionics*, 176 (**2005**) 2395.
161. A. Najib, J.E.H. Sansom, J.R. Tolchard, P.R. Slater, M.S. Islam, *Dalton. Trans*., (**2004**) 3106.
162. J.E.H. Sansom, A. Najib, P.R. Slater, *Solid State Ionics*, 175 (**2004**) 353.
163. J.E.H. Sansom, P.A. Sermon, P.R. Slater, *Solid State Ionics*, 176 (**2005**) 1765.
164. J.E.H. Sansom, P.R. Slater, *Solid State Ionics*, 167 (**2004**) 23.
165. J. Sansom, E. Kendrick, J. Tolchard, M. Islam, P. Slater, *J. Solid State Electrochem*., 10 (**2006**) 562.
166. E. Kendrick, J. Kendrick, K.S. Knight, M.S. Islam, P.R. Slater, *Nat. Mater*., 6 (**2007**) 871.
167. L. León-Reina, M.C. Martín-Sedeño, E.R. Losilla, A. Cabeza, M. Martínez-Lara, S. Bruque, et al., *Chem. Mater*., 15 (**2003**) 2099.
168. L. León-Reina, J.M. Porras-Vázquez, E.R. Losilla, M.A.G. Aranda, *J. Solid State Chem*., 180 (**2007**) 1250.
169. S. Li, F. Schönberger, P. Slater, *Chem. Commun*., 21 (**2003**) 2694.
170. L. Malavasi, C.A.J. Fisher, M.S. Islam, *Chem. Soc. Rev*., 39 (**2010**) 4370.
171. C.I. Thomas, X. Kuang, Z. Deng, H. Niu, J.B. Claridge, M.J. Rosseinsky, *Chem. Mater*., 22 (**2010**) 2510.
172. X. Kuang, M.A. Green, H. Niu, P. Zajdel, C. Dickinson, J.B. Claridge, et al., *Nat. Mater*., 7 (**2008**) 498.
173. C. Xia, M. Liu, *Adv. Mater*., 14 (**2002**) 521.
174. M. Camaratta, E. Wachsman, *Solid State Ionics*, 178 (**2007**) 1242.
175. M. Camaratta, E. Wachsman, *Solid State Ionics*, 178 (**2007**) 1411.
176. T. Yang, F. Li, D. Xia, *J. Power Sources*, 195 (**2010**) 2514.
177. S.P. Jiang, *J. Mater. Sci*., 43 (**2008**) 6799.
178. D.D. Button, D. Archer, *American Ceramic Society Meeting*, Washington, (**1966**).
179. H.-H. Möbius, *J. Solid State Electrochem*., 1 (**1997**) 2.
180. T. Tsai, S.A. Barnett, *Solid State Ionics*, 93 (**1997**) 207.
181. E.P. Murray, S.A. Barnett, *Solid State Ionics*, 143 (**2001**) 265.
182. X. Yue, A. Yan, M. Zhang, L. Liu, Y. Dong, M. Cheng, *J. Power Sources*, 185 (**2008**) 691.
183. H.G. Jung, Y.K. Sun, H.Y. Jung, J.S. Park, H.R. Kim, G.H. Kim, H.W. Lee, J.H. Lee, *Solid State Ionics*, 179 (**2008**) 1535.
184. T. Ishihara, M. Honda, T. Shibayama, H. Minami, H. Nishiguchi, Y. Takita, *J. Electrochem. Soc*., 145 (**1998**) 3177.
185. A.T. Duong, D.R. Mumm, *J. Power Sources*, 241 (**2013**) 281.
186. H.Y. Tu, Y. Takeda, N. Imanishi, O. Yamamoto, *Solid State Ionics*, 117 (**1999**) 277.

187. E. Niwa, U. Chie, E. Miyashita, T. Ohzeki, T. Hashimoto, *Solid State Ionics*, 201 (**2011**) 87.
188. J. Drennan, C.P. Tavares, B.C.H. Steele, *Mater. Res. Bull*., 17 (**1982**) 621.
189. E.J. Crumlin, E. Mutoro, Z. Liu, M.E. Grass, M.D. Biegalski, Y.L. Lee, D. Morgan, H.M. Christen, H. Bluhm, Y. Shao-Horn, *Energy. Environ. Sci*., 5 (**2012**) 6081.
190. Y.M. Kim, X. Chen, S.P. Jiang, J. Bae, *Electrochem. Solid-State Lett*., 14 (**2011**) B41.
191. T. Komatsu, R. Chiba, H. Arai, S. Kazunori, *J. Power Sources*, 176 (**2008**) 132.
192. P. Hjalmarsson, M. Mogensen, *J. Power Sources*, 196 (**2011**) 7237.
193. P. Hjalmarsson, M. Sogaard, A. Hagen, M. Mogensen, *Solid State Ionics*, 179 (**2008**) 636.
194. S. Hou, J.A. Alonso, S. Rajasekhara, M.J. Martinez-Lope, M.T. Fernandez-Diaz, J.B. Goodenough, *Chem. Mater*., 22 (**2009**) 1071.
195. S. Hashimoto, K. Kammer, F.W. Poulsen, M. Mogensen, *J. Alloys. Compd*., 428 (**2007**) 256.
196. J. Rebello, V. Vashook, D. Trots, U. Guth, *J. Power Sources*, 196 (**2011**) 3705.
197. S. Huang, Q. Lu, S. Feng, G. Li, C. Wang, *J. Power Sources*, 199 (**2012**) 150.
198. R. Kumar, R.J. Choudhary, M. Ikram, D.K. Shukla, S. Mollah, P. Thakur, K.H. Chae, B. Angadi, W.K. Choi, *J. Appl. Phys*., 102 (**2007**) 073707.
199. A.A. Taskin, A.N. Lavrov, Y. Ando Y, *Appl. Phys. Lett*., 86 (**2005**) 091910.
200. D. Parfitt, A. Chroneos, A. Tarancon, J.A. Kilner, *J. Mater. Chem*., 21 (**2011**) 2183.
201. J.H. Kim, A. Manthiram, *J. Electrochem. Soc*., 155 (**2008**) B385.
202. K. Zhang, L. Ge, R. Ran, Z. Shao, S. Liu, *Acta. Mater*., 56 (**2008**) 4876.
203. D. Chen, R. Ran, K. Zhang, J. Wang, Z. Shao, *J. Power Sources,* 188 (**2009**) 96.
204. L. Zhao, J. Shen, B. He, F. Chen, C. Xia, *Int. J. Hydrogen Energy*, 36 (**2011**) 3658.
205. M.T. Anderson, K.B. Greenwood, G.A. Taylor, K.R. Poeppelmeier, *Prog. Solid State Chem*., 22 (**1993**) 197.
206. Z.Q. Deng, J.P. Smit, H.J. Niu, G. Evans, M.R. Li, Z.L. Xu, J.B. Claridge, M.J. Rosseinsky, *Chem. Mater*., 21 (**2009**) 5154.
207. W. Zhou, J. Sunarso, J. Motuzas, F. Liang, Z. Chen, L. Ge, S. Liu, A. Julbe, Z. Zhu, *Chem. Mater*., 23 (**2011**) 1618.
208. Q. Liu, X. Dong, G. Xiao, F. Zhao, F. Chen, *Adv. Mater*., 22 (**2010**) 5478.
209. G. Xiao, Q. Liu, F. Zhao, L. Zhang, C. Xia, F. Chen, *J. Electrochem. Soc*., 158 (**2011**) B455.